

# Measurement of Reduced Dipole Matrix Elements in $^{40}\text{Ca}^+$ and Construction of a Scalable Light-Ion Interface



Dissertation

zur Erlangung des Doktorgrades Dr. rer. nat.  
der Fakultät für Naturwissenschaften der Universität Ulm

vorgelegt von  
**Max Hettrich**  
aus München

**2016**

---

Amtierender Dekan: Prof. Dr. Peter Dürre

Erstgutachter: Prof. Dr. Ferdinand Schmidt-Kaler

Zweitgutachter: Prof. Dr. Johannes Hecker Denschlag

Hiermit erkläre ich, MAX HETTRICH, dass ich die vorliegende Dissertation selbstständig angefertigt und keine anderen als die angegebenen Quellen und Hilfsmittel benutzt sowie die wörtlich und inhaltlich übernommenen Stellen als solche kenntlich gemacht und die Satzung der Universität Ulm zur Sicherung guter wissenschaftlicher Praxis beachtet habe.

MAX HETTRICH  
Mainz, den 27. Mai 2016

---



# Abstract

In the first part of this thesis, a method for determining transition dipole matrix elements is introduced. It combines measuring absorptive and dispersive atom-light interactions off-resonant to the transition in question and is thus resilient against various line-broadening effects. A single  $^{40}\text{Ca}^+$  ion confined in a Paul trap is used for implementing that method. Rather than counting individual photons, the method is based on discriminating atomic states of the ion's level scheme, which circumvents many systematic error sources affecting other methods. The dipole matrix elements of the  $4^2S_{1/2} \leftrightarrow 4^2P_{1/2}$ , the  $4^2S_{1/2} \leftrightarrow 4^2P_{3/2}$  and the  $4^2P_{1/2} \leftrightarrow 3^2D_{3/2}$  transitions are determined. Moreover, the method allows also for the deduction of the radiative lifetime of the  $4^2P_{1/2}$  state which reads 6.904(26)ns. This value is in agreement with recent theoretical calculations, and resolves a long-standing discrepancy between calculated values and experimental results.

In the second part of the thesis, the design, construction, assembly and characterization of a segmented, microstructured Paul trap which can accommodate a fiber cavity for light-ion interaction is described. The trap features 31 segments, which allow for ion transport along the trap axis. Vertical interconnect accesses needed to be incorporated in the design of the conducting paths in order to electrically connect all segment electrodes to the outside. The trap is fabricated from alumina substrates and evaporatively coated with gold. To further characterize the trap, simulations of axial trap frequencies have been compared with measured values for different regions in the trap, also axial transport of single ions over a distance of  $\approx 2.5$  mm has been implemented. Coherent dynamics on the quadrupole transition of  $^{40}\text{Ca}^+$  have been used to perform sideband cooling and a single ion was cooled below the Doppler limit. The dynamics of carrier and red sideband transitions have been employed to measure the trap's heating rate, which amounts to  $\dot{n} = 16.5/\text{ms}$  at a trap frequency of  $2\pi \times 1.32$  MHz.

---

# Zusammenfassung

Im ersten Teil der vorliegenden Arbeit wird eine Methode zur Bestimmung von Übergangsdipolmatrixelementen eingeführt. Sie kombiniert die Messung von absorptiven und dispersiven Atom - Lichtwechselwirkungen, welche nichtresonant zum betrachteten Übergang sind, und damit unempfindlich gegen zahlreiche Linienverbreiterungseffekte. Ein einzelnes  $^{40}\text{Ca}^+$  Ion in einer Paulfalle wird benutzt um diese Methode zu implementieren. Anstatt einzelne Photonen zu zählen, basiert die Methode auf der Unterscheidung von atomaren Zuständen im Termschema des Ions, wodurch viele systematische Fehlerquellen umgangen werden, welche andere Methoden beeinträchtigen. Die Dipolmatrixelemente der  $4^2S_{1/2} \leftrightarrow 4^2P_{1/2}$  -,  $4^2S_{1/2} \leftrightarrow 4^2P_{3/2}$  - und  $4^2P_{1/2} \leftrightarrow 3^2D_{3/2}$  - Übergänge werden bestimmt. Darüber hinaus erlaubt die Methode die Bestimmung der Lebensdauer des  $4^2P_{1/2}$  - Zustandes, welche 6.904(26) ns beträgt. Dieser Wert stimmt mit aktuellen theoretischen Berechnungen überein, und löst eine lange bestehende Diskrepanz zwischen berechneten Werten und experimentellen Resultaten auf.

Im zweiten Teil der Arbeit wird beschrieben, wie eine segmentierte, mikrostrukturierte Paulfalle, die mit einem Faserresonator ausgestattet werden kann, entworfen, konstruiert, zusammengebaut und charakterisiert wurde. Die Falle besteht aus 31 Segmenten, was einen Ionentransport entlang der Fallenachse erlaubt. Vertikale elektrische Verbindungen waren für den Entwurf der Falle erforderlich um alle Segmentelektroden elektrisch nach außen zu kontaktieren. Die Falle wurde aus Aluminasubstraten hergestellt, welche mit Gold bedampft wurden. Um die Falle zu charakterisieren, wurden zudem Simulationen axialer Fallenfrequenzen mit gemessenen Werten in unterschiedlichen Regionen der Falle verglichen, ebenso wurde der axiale Transport einzelner Ionen über eine Distanz von  $\approx 2.5$  mm implementiert. Kohärente Dynamik auf dem Quadrupolübergang von  $^{40}\text{Ca}^+$  wurde benutzt um Seitenbandkühlen zu realisieren. Dabei wurde ein einzelnes Ion unter das Dopplerlimit gekühlt. Die Dynamik auf Träger- und Seitenbandübergängen wurde benutzt, um die Heizrate der Falle zu bestimmen, welche  $\dot{n} = 16.5/\text{ms}$  bei einer Fallenfrequenz von  $2\pi \times 1.32$  MHz beträgt.

---

# Contents

<b>1. Introduction</b>	<b>11</b>
<b>2. Theoretical Foundations</b>	<b>19</b>
2.1. Resonant Light - Ion Interaction . . . . .	19
2.2. Off-resonant Light - Ion Interactions . . . . .	21
2.2.1. Dispersive Interaction: AC-Stark Shift . . . . .	21
2.2.2. Absorptive Interaction: Off-resonant Excitation . . . . .	22
2.2.3. Ions in Paul Traps: A Two Level System in a Harmonic Potential	26
2.3. Atomic Dipole Matrix Elements & Fermi's Golden Rule . . . . .	30
2.4. Segmented Ion Trap Fundamentals . . . . .	33
<b>3. Measurement of Dipole Matrix Elements</b>	<b>37</b>
3.1. The $^{40}\text{Ca}^+$ Level Scheme . . . . .	37
3.2. Lasersystem . . . . .	38
3.2.1. Doppler Cooling, State Detection and Optical Pumping (397 nm)	39
3.2.2. Repumping and Quenching (866 nm & 854 nm) . . . . .	41
3.2.3. Electron Shelving and Optical Pumping (729 nm) . . . . .	42
3.2.4. Coherent Dynamics and Off-resonant Interactions (397 nm) . . .	42
3.2.5. Photoionization (375 nm & 423 nm) . . . . .	44
3.3. Vacuum Chamber and Imaging System . . . . .	44
3.4. Measurement Principle . . . . .	46
3.4.1. Off-resonant Excitation and the Spin-flip Rates $R_+$ and $R_-$ . . .	46
3.4.2. The AC-Stark Shift $\Delta_S$ . . . . .	50
3.4.3. Combining $R_+$ , $R_-$ and $\Delta_S$ to obtain Decay Rates and Matrix Elements . . . . .	52
3.5. Experimental Implementation . . . . .	54
3.5.1. The Measurement of $R_{\pm}$ and $\Delta_S$ . . . . .	54
3.5.2. The Measurement of the Detuning $\Delta$ . . . . .	59
3.6. Data Evaluation and Results . . . . .	59
3.6.1. Data Acquisition . . . . .	59
3.6.2. Determining the Spin-flip Rates $R_+$ and $R_-$ . . . . .	60

3.6.3. Determining the AC-Stark Shift $\Delta_S$ . . . . .	62
3.6.4. Determining the Frequencies $\nu_i$ of the Off-resonant Laser . . . . .	63
3.6.5. Results, Uncertainties and Shifts . . . . .	63
3.7. Discussion . . . . .	67
<b>4. A Segmented Ion Trap for CQED Experiments</b>	<b>69</b>
4.1. Design and Fabrication . . . . .	69
4.1.1. Conceptual Guidelines . . . . .	69
4.1.2. Trap Design . . . . .	71
4.1.3. Trap Fabrication . . . . .	74
4.1.4. Filterboard for Electrical Connections . . . . .	75
4.1.5. Fiber Cavity Assembly . . . . .	76
4.2. Characterization Measurements . . . . .	78
4.2.1. Experimental Setup . . . . .	78
4.2.2. Static and Dynamic Trap Potential Control . . . . .	79
4.2.3. Coherent Dynamics and Sideband Cooling . . . . .	84
4.3. Discussion . . . . .	88
<b>5. Conclusion and Outlook</b>	<b>91</b>
<b>A. Uncertainties of the Matrix Element Measurements</b>	<b>93</b>
A.1. Data Overview . . . . .	93
A.2. Uncertainties and Corrections of the Measured Variables . . . . .	93
A.2.1. Statistical Uncertainty of $\delta R$ and $b$ . . . . .	94
A.2.2. Detuning $\Delta$ . . . . .	94
A.2.3. Residual Near-resonant Light at 397 nm . . . . .	95
A.2.4. Residual $\pi$ -polarized Off-resonant Light . . . . .	97
A.2.5. Differential AC-Stark Shift $\Delta_S$ . . . . .	98
A.2.6. Zeeman Shift . . . . .	98
A.2.7. Influence of Micromotion . . . . .	99
A.2.8. Influence of Near-Resonance-Effects . . . . .	99
A.2.9. Finite $D_{3/2}$ -lifetime and residual 866 nm repump light . . . . .	101
A.2.10. Influence of the $P_{3/2}$ state . . . . .	102
A.2.11. Fit bias . . . . .	103
A.2.12. SPAM uncertainties . . . . .	103
A.3. Total uncertainties and corrections of $\gamma_{PS}, \gamma_{PD}$ and $\tau$ . . . . .	103
<b>B. Drawings of the Light-Ion Interface Trap</b>	<b>107</b>
<b>C. Mappings of electrical connections</b>	<b>113</b>
<b>D. List of Publications</b>	<b>115</b>

# 1. Introduction

The possibility to experiment with single or few atoms is arguably one of the greatest scientific achievements of the 20th century. Starting with the invention of the *Ionenkäfig* (ion cage) [Pau58] by W. Paul, O. Osberghaus and E. Fischer in 1958, it became possible to isolate and trap ions in a confined volume. This means, single atoms had finally entered laboratory reality after more than 2 millennia since the concept of *atomism* was formulated by Democritus in Ancient Greece. This new experimental technique was a very suitable tool to study quantum mechanics, a fundamental theory for physics at very small scales, developed by M. Planck, A. Einstein, E. Schrödinger and others at the beginning of the 20th century. The reason quantum mechanics was met in the beginning with a certain amount of disbelief was the prediction of seemingly counterintuitive phenomena, like the wave-particle dualism, or Heisenberg’s uncertainty principle. Even E. Schrödinger, one of the founders of the new theory is cited with the words:

*“We never experiment with just one electron or atom or (small) molecule. In thought experiments, we sometimes assume that we do; this invariably entails ridiculous consequences...”*

With ion traps, in conjunction with the rapid progress of laser spectroscopy since the 1970s [Hän99], these experiments started to become possible.

Since these days, ion trap physics has come a long way, and quite some “*ridiculous consequences*” of Schrödingers theory have been experimentally observed in ion trap experiments:

- **Ground State Cooling and Quantized Motional Excitation**

In the quantum mechanical regime, the kinetic energy of a particle in a trapping potential only takes on distinctive, quantized values, whereas in classical mechanics it is a continuous quantity. This has been observed e.g. in [Lei97] using a single  ${}^9\text{Be}^+$  ion. Furthermore, it is possible to remove all those excitation quanta one by one, until (almost) none is left, and the particle’s energy is reduced to the minimum value of  $\hbar\omega/2$ , the energy of ion’s motional ground state [Die89, Mon95, Roo99].

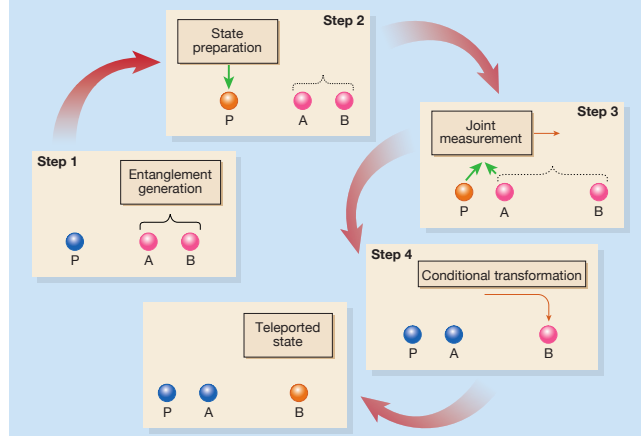


**Figure 1.1.:** Scheme for deterministic quantum teleportation, as implemented in [Rie04] and [Bar04]. The state of ion P is teleported to ion B. Image taken from [Kim04]

- **Superposition of States**

Using suitable ion-laser interactions, it is possible to create a coherent superposition of the ion's internal electronic states. As soon as the state is detected, the ion's wavefunction collapses, to either one or the other of those states.

- **Non-classical States**

When the ion is subject to state dependent optical forces, and is prepared in a superposition state, the ion's wavefunction is split up, being in two separate locations at once [Mon96, Lei03a, Pos10a]. In reference to a famous thought experiment conceived by E. Schrödinger [Sch35], such states are sometimes called *Schrödinger Cat States*.

- **Teleportation**

It is straight forward to show, that an arbitrary quantum state cannot be cloned [Woo82]. However, using the scheme of quantum teleportation, the state of one system can be imprinted on a similar one, and the state of the original system is erased. This has been implemented using ion traps [Rie04, Bar04], see Fig. 1.1, and also with ions, which are located several meters apart [Olm09].

- **Entanglement**

When two or more particles are entangled, each particle cannot be described independently anymore, without taking into account the composite state as a whole. This means, also the correlations between the the particles' states have to be taken into account. The maybe most prominent example of entangled states are



---

the Bell states [Nie00]. The measurement outcome of the state of each individual particle is totally random, but the measured states of two such entangled particles are perfectly correlated, even if both measurement events are space-like separated. Controlled entanglement of up to 14 ions has been realized in the lab [Mon11].

- **Quantum Simulation and Computation**

The numerical calculation of complex quantum mechanical problems is computationally expensive. In the 1980, R. P. Feynman had the idea to use one quantum system, which can be very well controlled experimentally to predict the behavior of another system, which does not feature the same level control, but whose description is equivalent to the first one. Following that idea, a simplified version of the Zitterbewegung has been simulated using a two ion crystal [Ger10], or a set of frustrated Ising spins [Kim10] using three ions.

The application of quantum physics with arguably the largest prospective impact on science and technology is the concept of universal quantum computing [Man80, Fey82, Deu85]. Using qubits, i.e. quantum mechanical two-level systems instead of classical bits, together with a number of requirements known as the DiVincenzo criteria [DiV96] allows for running algorithms not implementable on classical computers. Shor's factoring algorithm is the most prominent of those, as it can be used to break most of today's widely used asymmetric cryptographic algorithms, which are considered secure against attacks with classical computers. Proof of concept implementations of Shor's algorithm have been realized in ion traps [Mon16], as well as other quantum algorithms [Gul03, Bri05]. As of 2016, some major technology corporations started to direct considerable efforts towards realizing quantum computers for commercial purposes.

A remarkable feature common to all those eye-opening experiments is the *simplicity* of the physical systems, which are studied (which by no means must be misunderstood for the experiments in question being *easy* to conduct). The systems under consideration consist only of a few charged atoms in a harmonic potential, together with suitable laser fields for interaction and measurement. The underlying theoretical descriptions of how those systems behave are very clean and straight forward in the most cases.

In recent years, many efforts have been made to carefully add elements, i.e. add complexity to ion trap experiments in order to study effects and behavior of systems, which are physically more rich. One of the more obvious advancements in ion trap technology was implementing segmented electrode structures (Fig. 1.2a), which allow for dynamically shaping trapping potentials. This makes it possible to shuttle ions around during experiments [Wal12, Bow12], or to split and recombine ion crystals [Rus14]. These are

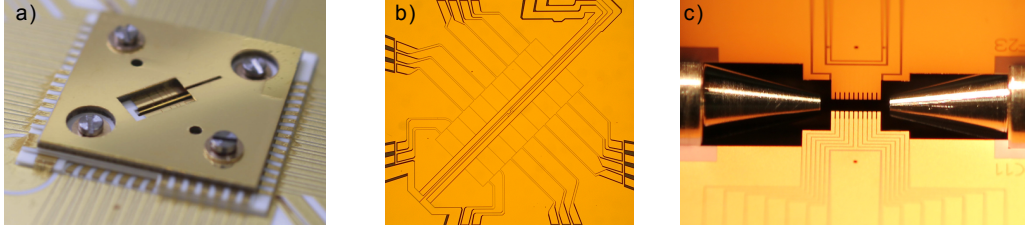


**Figure 1.2.:** a) Segmented micro trap for advanced potential shaping [Kie15]. b) Planar trap for creating large magnetic field gradients close to the ion position [Sal15]. c) Trap for ion extraction, where ions are shot through the hollow endcaps [Jac16].

important techniques for scaling up the number of qubits in quantum computing experiments [Kie02]. Easier fabrication of advanced trap structures is possible, if all electrodes are located in one plane, thus enabling the use of photolithography technology. The trap in Fig 1.2 b) features a structure which allows the creation of large magnetic field gradients at the ion position, enabling spin-spin interactions [Joh09]. Also, more exotic ideas have been realized like the trap in Fig. 1.2 c), which is used as a deterministic single ion source. Ions of different species are extracted from the trap and can be used for microscopy purposes [Jac16]. The method might be also used for implanting ions in diamond substrates with nanometer resolution. This can create color centers, which are again an candidate system for quantum computing [Jel04, Niz05, Dut07].

Another obvious extension of ion trapping experiments is the coupling to a different quantum system. Here, photons are a natural choice, as the interaction with classical optical fields is part of virtually all ion trap experiments. For neutral atom systems, groundbreaking results have been achieved in the last two decades, where single photons could be coupled to single or few atoms using optical cavities [Kim98, Kuh99]. For trapped ions, this has been always much more difficult, as low-loss, high reflective optical mirrors are typically made from dielectric materials. As those materials are subject to electrostatic charging, they will in general distort the carefully designed electric potential of the ion trap, if located in its close vicinity. To minimize that detrimental effect, mirrors for CQED experiments with ions need to be located far away from the ions' location. This in turn limits the rate, at which single photons can couple to single ions. Lots of effort have been invested in CQED experiments with ions in recent years, and many spectacular results have been reported [Gut01, Mun02, Her09, Stu12, Ste13], but the regime of strong ion-photon coupling, where the dynamics of the single photon - single ion interaction are happening on a much faster timescale than any decoherence effect, remained beyond reach.

A very promising technological progress for ion trap CQED was the development of fiber cavities in the neutral atom community [Ste06, Col07, Hun10]. Using the end facets of

---

two optical fibers as a cavity, a Bose-Einstein condensate could be strongly coupled to the cavity's field. The small geometrical dimensions of such a cavity in conjunction with the attainable high finesse opens up new possibilities of integrating such a device in the electrode structure of an ion trap. Especially miniaturized trap designs with multiple segments seem suitable for integrating fiber cavities. The trap's dimensions can be chosen to fit those of the used fibers, and the electrodes can be designed such that they largely shield the dielectric material. To realize such concepts, it is necessary again to come up with another extension of a “classical” trap design, much like those shown in Fig. 1.2, but with the additional feature to accommodate a fiber cavity. The design, implementation and characterization of such a specialized trap is discussed in the second part of this thesis.

The ion of choice for all experiments presented in the following is  $^{40}\text{Ca}^+$ . It features a comparatively simple level structure of an effective one-electron system, but has still many key features for quantum optics experiments. Moreover, the fortunate values of the transition frequencies right in or near the visible range allow for using laser systems, which are commercially available at relatively low cost together with off-the-shelf optical elements such as fibers. Those advantages are the reason why  $^{40}\text{Ca}^+$  is widely used in the ion trapping community, and many key experiments of ion trap physics have been conducted with that species. Interestingly enough, quantum optics is not the only field in physics, where that specific ion played a major role. The discovery of the interstellar medium was based on an absorption line spectroscopy measurement, where J. Hartmann observed in 1904, that the position of the Calcium K-line (which is just the  $4^2S_{1/2} - 4^2P_{3/2}$  transition in  $^{40}\text{Ca}^+$ ) did not move periodically in the spectrum of the spectroscopic binary Delta Orionis, in contrast to other lines [Har04]. He concluded, that the absorbing medium did not move together with the star, but must be located at a fixed position somewhere in the line of sight between observer and star. Also when studying emission spectra from the sun and other stars, the Calcium K-line and H-line (being the  $4^2S_{1/2} - 4^2P_{1/2}$  transition) are regularly examined [Rau06, Car12]. Consequently, as a result of the large interest in that species, the internal structure of  $^{40}\text{Ca}^+$  has been studied in detail over the years, and all spectroscopic data of the low-lying energy levels are known to a high degree of precision. Especially the transition linewidths and frequencies of the  $D$ -levels are of high relevance to quantum computing applications, and precise results have been reported fairly recently [Kre05, Chw09]. Also the branching ratio of the spontaneous decay of the  $4^2P_{1/2}$  level was measured with high accuracy [Ram13]. Theoretical calculations of the ion's internal structure are in good agreement with experimental data as well, which is expected, as this is also the case for most hydrogen-like species [Saf11]. There is one exception however: The radiative lifetime of the  $4^2P_{1/2}$  state is calculated to be 6.875(62) ns [Saf11], but the up to now

most recent measured value was 7.098(20) ns [Jin93], disagreeing with the theoretical value by more than 11 standard deviations. The investigation of that inconsistency is the starting point for the investigations presented in the first part of this thesis. But as it turns out, the described measurement method additionally reveals quite a bit more about the internal structure of  $^{40}\text{Ca}^+$  than only that lifetime. It was also possible to deduce transition dipole matrix elements, which are notoriously hard to measure by other means. Moreover, the method is applicable not only to  $^{40}\text{Ca}^+$ , but also to other atomic species, which allow for the preparation and readout of Zeeman or hyperfine sublevels.

This thesis is structured as follows: The theoretical framework for the discussed experiments is presented in chapter 2 such that the text is mostly self-contained. Fundamental light-atom interaction theory is laid out for the resonant, and the off-resonant case, where specifically dispersive and absorptive effects are discussed. Additionally, the basic working principle of a Paul trap is presented, and how it can be extended to segmented trap structures. The measurement of the  $4^2P_{1/2}$  state's lifetime and the matrix elements of  $^{40}\text{Ca}^+$  is presented in Chapter 3. At the beginning the experimental apparatus is described. The employed laser system consists mainly of diode laser, only for driving the quadrupole transition a titanium sapphire laser system is used, whose increased frequency stability over time helps to reduce systematic errors in measurement runs with durations of  $\sim 10$  h. Afterwards, a novel concept of how to measure the decay rate of the  $4^2P_{1/2} \leftrightarrow 4^2S_{1/2}$  transition is presented. It combines measuring dispersive and absorptive interactions of an off-resonant laser field. The method does not rely on counting photon numbers, only dark and bright states of one ion are distinguished, which makes the method resilient against many kinds of systematic uncertainties. Then a detailed description of the implementation of that method using the apparatus at hand is given. Data acquisition and evaluation are presented afterwards, together with the results. Special care needed to be taken to ensure that systematic effects like e.g. long-term drifts of laser-beam positions do not spoil the data. In the end, all results are summarized and compared to literature values where applicable.

In chapter 4, the new trap for ion-photon interaction is presented. In the beginning, the key concepts of the design are laid out. It is based on a segmented microtrap [Sch08] with two distinct regions. In one region, the electrode-ion distance is rather large with  $\sim 250\mu\text{m}$  for easy loading, whereas in the other region, this distance is reduced to  $\sim 125\mu\text{m}$  to allow for the integration of a fiber cavity with a small mode volume, and thereby large ion-photon coupling. The possibility of integrating a fiber cavity poses considerable constraints for connecting the trap electrodes, so special care needed to be taken. The trap is fabricated from alumina substrates, which are coated with gold by evaporation deposition. Structures in the coating and the substrate are cut using a

---

fs-laser. Furthermore, the assembly process of the trap is discussed in detail. This is followed up by a description of the vacuum vessel and the laser system for operating the trap. It consists completely of grating stabilized diode lasers, which allows for low maintenance operation compared to other, technically more complex laser systems. Once in operation, axial trap frequencies have been determined in all distinct trap regions, which are compared to simulation results using a numerical field solver [Sin10]. Finally, coherent dynamics on the quadrupole transition are studied in order to learn about the heating rate of the ion's motional state in that trap. An outlook wraps up the thesis, discussing the results, and formulating goals for the future. Appendix A gives a detailed treatise of the sources of uncertainty for the measurements in chapter 3 and their impact on the results. Detailed Drawings of the trap design discussed in chapter 4 are provided in appendix B, the mappings of the trap's connections outside the vacuum vessel are laid out in appendix C.



## 2. Theoretical Foundations

### 2.1. Resonant Light - Ion Interaction

The  $^{40}\text{Ca}^+$  ion features a multitude of energy eigenstates 18 of which are readily accessible by driving transition using laser radiation in the VIS or NIR spectrum [Roo00, Roh01]. Instead of starting with a description of the complete system, in order to gain insight to the basic principles of light-ion interaction, it is at first sufficient to only consider a subset of two of those states. Several ways of describing such a quantum mechanical two-level system can be found in a wide variety of literature. The treatment given below follows some selected texts [Bud08, Bra92, Har06, All75, Obe99] in order to provide the reader with the theoretical foundations of the work described in this thesis in a largely self-consistent way.

In the treatment below, the case where a laser field is resonant to the transition between the two states is outlined first before off-resonant interactions are described. Both cases are required for the technique to determine dipole matrix elements, which is a discussed in detail in chapter 3.

Now, we consider two energy levels of an atom, a ground state  $|g\rangle \equiv \begin{pmatrix} 1 \\ 0 \end{pmatrix}$  and an excited state  $|e\rangle \equiv \begin{pmatrix} 0 \\ 1 \end{pmatrix}$ , which form the basis of a two-dimensional Hilbert space. The Hamiltonian  $\hat{H}$  of the system reads

$$\hat{H} = \hat{H}_0 + \hat{H}_i, \quad (2.1)$$

where  $\hat{H}_0$  ist the part of the Hamiltonian describing the unperturbed system, and  $\hat{H}_i$  describes the interaction with an external field which induces a coupling of  $|g\rangle$  and  $|e\rangle$ . They read

$$\hat{H}_0 = \begin{pmatrix} 0 & 0 \\ 0 & \hbar\omega_0 \end{pmatrix} \quad \hat{H}_i = \begin{pmatrix} 0 & -\mathcal{D}E_0 \sin(\omega t) \\ -\mathcal{D}E_0 \sin(\omega t) & 0 \end{pmatrix}. \quad (2.2)$$

$\omega_0$  denotes the transition frequency between  $|g\rangle$  and  $|e\rangle$ ,  $\mathcal{D}$  is the matrix element of the transition (see chapter 2.3),  $E_0$  the amplitude and  $\omega$  the oscillation frequency of the electrical field. For now, only the resonant case is considered, i.e.  $\omega = \omega_0$ .

The dynamics of the system are described by the time-dependent Schrödinger equation,

$$i\hbar|\dot{\psi}\rangle = \hat{H}|\psi\rangle, \quad (2.3)$$

where  $|\psi\rangle$  is the time dependent state vector of the system. Analytical treatment of the equation is simplified, if it is transformed into a rotating frame, using the unitary operator

$$\hat{U} = \begin{pmatrix} 1 & 0 \\ 0 & e^{i\omega t} \end{pmatrix} \quad (2.4)$$

to obtain  $|\psi\rangle' = \hat{U}^\dagger |\psi\rangle$ , and a modified Schrödinger equation

$$i\hbar|\dot{\psi}\rangle' = \underbrace{(\hat{U}^\dagger \hat{H} \hat{U} - i\hbar \hat{U}^\dagger \dot{\hat{U}})}_{=\hat{H}'} |\psi\rangle', \quad (2.5)$$

where  $\hat{H}'$  is introduced as a new, effective Hamiltonian. Written down explicitly, one obtains

$$\hat{H}' = \begin{pmatrix} 0 & \frac{i}{2}\mathcal{D}E_0(1 - e^{-2i\omega t}) \\ -\frac{i}{2}\mathcal{D}E_0(1 - e^{2i\omega t}) & 0 \end{pmatrix}. \quad (2.6)$$

Neglecting the fast oscillating terms  $\sim 2\omega$  by means of the *rotating wave approximation* (RWA), and introducing the Rabi frequency  $\Omega_0 = \mathcal{D}E_0/\hbar$ , the Schrödinger equation reads

$$\begin{pmatrix} \dot{c}_1(t) \\ \dot{c}_1(t) \end{pmatrix} = \frac{1}{2} \begin{pmatrix} 0 & \Omega_0 \\ -\Omega_0 & 0 \end{pmatrix} \begin{pmatrix} c_1(t) \\ c_1(t) \end{pmatrix}, \quad (2.7)$$



where the  $c_i(t)$  are the components of the state vector  $\psi(t)$ . Solving this system of differential equations for the initial condition  $\begin{pmatrix} c_1(0) \\ c_2(0) \end{pmatrix} = |g\rangle = \begin{pmatrix} 1 \\ 0 \end{pmatrix}$  yields

$$\begin{aligned} c_1 &= \cos\left(\frac{\Omega_0}{2}t\right) \\ c_2 &= -\sin\left(\frac{\Omega_0}{2}t\right) \end{aligned} \quad (2.8)$$

The squared absolute values of those probability amplitudes  $|c_i|^2$  describe the probabilities  $p_i$  to find the atom in the respective state after interacting with the external field for the time  $t$ , when a projective measurement in the energy-eigenbasis is performed, i.e.

$$p_{|e\rangle} = |c_2|^2 = \sin^2\left(\frac{\Omega_0}{2}t\right) \quad (2.9)$$

Performing a series of such measurements when scanning the values for the interaction time  $t$ , one obtains the well-known *Rabi oscillations*.

## 2.2. Off-resonant Light - Ion Interactions

Starting from the basic results above for the resonant case, it is straight forward to extend those considerations to the case, where the electrical fields frequency  $\omega$  is off-resonant to the transition frequency  $\omega_0$  of the atom, i.e.  $\omega - \omega_0 = \Delta \neq 0$ . This leads to a *dispersive interaction*, where the electrical field is shifting the positions of the participating energy levels. Adding a finite spontaneous decay rate to the two level system's description allows for an incoherent *absorptive interaction*, even if the the exciting electrical field has a frequency far from resonance. For the case, when a *harmonic potential* is added to the two level system, as it is the case for a single ion in a Paul trap, an off-resonant laser field can induce a coupling between both systems.

### 2.2.1. Dispersive Interaction: AC-Stark Shift

The AC-Stark shift can be understood by redoing the evaluation from the resonant case, but keeping both quantities  $\omega$  and  $\omega_0$ , with  $\omega - \omega_0 = \Delta$ . Eqs. 2.2, 2.4, 2.5 remain unchanged, but Eq. 2.6 changes to (after performing the RWA)

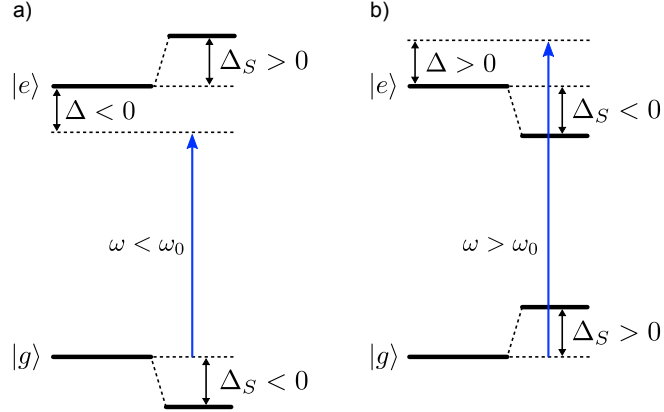


**Figure 2.1.:** Signs of AC-Stark shifts  $\Delta_S$  of ground state  $|g\rangle$  and excited state  $|e\rangle$  depending on the detuning  $\Delta$ .  $\Delta < 0$  (a) increases (decreases) the energy of  $|e\rangle$  ( $|g\rangle$ ) and vice versa for  $\Delta > 0$  (b). In both cases all levels are always pushed further away from resonance.

$$\hat{H}'_{off} = \begin{pmatrix} 0 & \frac{i}{2}\mathcal{D}E_0 \\ -\frac{i}{2}\mathcal{D}E_0 & \hbar(\omega_0 - \omega) \end{pmatrix} = \hbar \begin{pmatrix} 0 & \frac{i}{2}\Omega_0 \\ -\frac{i}{2}\Omega_0 & -\Delta \end{pmatrix} \quad (2.10)$$

In the rotating frame, Eq. 2.10 has the form of a Hamiltonian describing a *DC-Stark shift* induced by the electrical field  $E_0/2$ . It shifts two states with the energy difference  $\hbar\omega_0$  by

$$\Delta_S = \pm \frac{\Omega_0^2}{4\Delta}, \quad (2.11)$$

as follows from the use of second order perturbation theory [Bra92]. The positive sign refers to the lower, the negative one to the upper level. The process is depicted in Fig. 2.1.

### 2.2.2. Absorptive Interaction: Off-resonant Excitation

The formalism so far only incorporates *coherent* dynamics of the two level system. This means, an arbitrary state  $|\psi\rangle$  can be transferred to a different arbitrary state  $|\psi'\rangle$  in the same Hilbert space by means of *unitary* operations,  $|\psi'\rangle = U|\psi\rangle$ . If the Hamiltonians  $\hat{H}(t_i)$  for different times  $t_i$  commute, the evolution through time of an arbitrary state reads

$$|\psi(t_1)\rangle = \hat{U}(t_0, t_1) |\psi(t_0)\rangle = e^{i/\hbar \int_{t_0}^{t_1} \hat{H}(\tau) d\tau} |\psi(t_0)\rangle. \quad (2.12)$$

The probably most simple example, where the evolution of a two level system cannot be described anymore with a unitary operator is, when the excited state experiences *spontaneous decay*. On a fundamental level, this can be described by a quantum field theory, where the two level system is interacting with a multitude of vacuum modes of the electromagnetic field [CT04], but in many circumstances, this is not a feasible approach. The alternative is to extend the Schrödinger theory with a mechanism for state transitions caused by external effects, whose detailed physical description is not feasible or not possible at all. In this case, the quantum system cannot solely be described anymore by a *pure* quantum state  $|\psi\rangle$ , but a more general *density matrix*  $\hat{\rho}$  needs to be used. Apart from pure quantum states, a density matrix can also describe *statistical mixtures*, which are comprised of partly or completely collapsed quantum states. The dynamics of density matrices is described by the *Kossakowski-Lindblad equation* [Kos72, Lin76, Har06]

$$\dot{\hat{\rho}} = -\frac{i}{\hbar}[\hat{H}, \hat{\rho}] + \mathcal{L}(\hat{\rho}). \quad (2.13)$$

It resembles the Schrödinger equation in many ways, but additionally it features the *Lindblad Superoperator*  $\mathcal{L}(\hat{\rho})$  which describes non-unitary dynamics, e.g spontaneous decay. It reads

$$\mathcal{L}(\hat{\rho}) = \frac{1}{2} \sum_m \left[ 2\hat{C}_m \hat{\rho} \hat{C}_m^\dagger - \hat{C}_m^\dagger \hat{C}_m \hat{\rho} - \hat{\rho} \hat{C}_m^\dagger \hat{C}_m \right], \quad (2.14)$$

where the  $\hat{C}_m$  are called *collapse operators*

If this framework is used to describe spontaneous emission in a two level system, only one collapse operator  $\hat{C}$  is used, which reads

$$\hat{C} = \sqrt{\gamma} |g\rangle \langle e|, \quad (2.15)$$

for a decay rate  $\gamma$ . The explicit form of Eq. 2.13 for the two-level system then reads

$$\begin{aligned} \dot{\rho}_{11} &= \frac{\Omega_0}{2}(\rho_{12} + \rho_{21}) + \gamma\rho_{22} \\ \dot{\rho}_{12} &= -i\Delta\rho_{12} + \frac{\Omega_0}{2}(\rho_{22} - \rho_{11}) - \frac{\gamma}{2}\rho_{12} \\ \dot{\rho}_{21} &= i\Delta\rho_{21} + \frac{\Omega_0}{2}(\rho_{22} - \rho_{11}) - \frac{\gamma}{2}\rho_{21} \\ \dot{\rho}_{22} &= -\frac{\Omega_0}{2}(\rho_{12} + \rho_{21}) - \gamma\rho_{22}. \end{aligned} \quad (2.16)$$

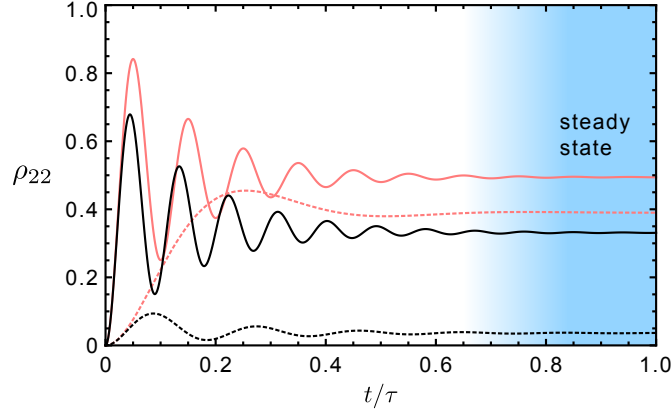


**Figure 2.2.:** Numerical simulation of the dynamics of  $\rho_{22}$ , see Eq. 2.16. For short times, the system undergoes Rabi oscillations, which die down after some time, and a steady state, which does not change anymore in time, is reached. For the shown diagrams, the Rabi frequencies read  $\Omega_0 = 2\pi \times 10/\tau$  ( $\Omega_0 = 2\pi \times 2/\tau$ ) for the solid (dashed) curves, the detuning  $\Delta = 0$  ( $2\pi \times 5/\tau$ ) for the red (black) curves. The decay rate  $\gamma = 2\pi \times 1.5/\tau$ .

The components of the density matrix  $\hat{\rho}$  are not independent. As  $\hat{\rho}$  is always hermitian, the relation

$$\rho_{12} = \rho_{21}^* \quad (2.17)$$

always holds. Also, because the system's population is normalized, the condition

$$\rho_{11} + \rho_{22} = 1 \Rightarrow \dot{\rho}_{11} = -\dot{\rho}_{22} \quad (2.18)$$

holds for all times. This reduces the equation system 2.16 to

$$\begin{aligned} \dot{\rho}_{12} &= \left(i\Delta + \frac{\gamma}{2}\right) \rho_{12} + \frac{\Omega_0}{2} w \\ \dot{w} &= -\Omega_0(\rho_{12} + \rho_{21}) - \gamma(w + 1), \end{aligned} \quad (2.19)$$

where the *inversion*  $w = \rho_{22} - \rho_{11}$  is introduced. Of further interest now is the *steady state solution*, i.e. the solution of that system after a long time, when the system is stable and does not experience any further change, see Fig. 2.2. This can be expressed by the additional requirements

$$\begin{aligned} \dot{w} &= 0 \\ \dot{\rho}_{12} &= 0. \end{aligned} \quad (2.20)$$

Eqs. 2.19 can now be solved for  $w$ , and one obtains

$$w = -\frac{1}{1 + \frac{\Omega_0^2/2}{\Delta^2 + \gamma^2/4}} = -\frac{1}{1 + S} \quad (2.21)$$

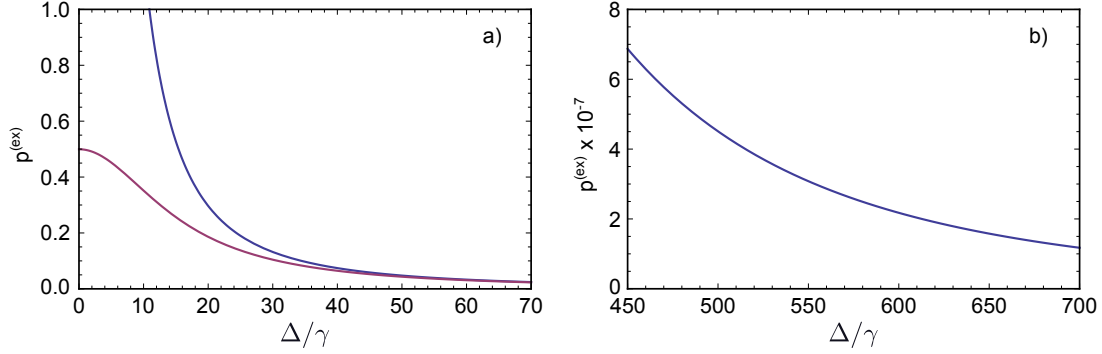


**Figure 2.3.:** Evaluation of approximation Eq. 2.23 in the relevant parameter regime. a) Plots of  $p^{(ex)}$  over detuning  $\Delta$  for the exact case (Eq. 2.22, red) and the approximation (Eq. 2.23, blue). It is clear, how the hyperbola-shaped approximation deviates from the saturation broadened Lorentzian curve of the exact solution close to resonance. If however the detuning  $\Delta$  becomes larger than  $50 \gamma$ , the approximation starts to coincide with the exact calculation pretty well. b) Plot of the difference of Eq. 2.22 and Eq. 2.23 in the far-detuned region studied in this thesis ( $\Delta = 2\pi \times 10 \dots 15 \text{ GHz} = 450 \dots 700 \gamma$ ). The deviation is at a level of better than  $10^{-6}$ . For both plots, also Rabi frequency  $\Omega_0$  and decay rate  $\gamma$  are set close to values observed in the experiment, being  $\Omega_0 = 2\pi \times 470 \text{ MHz}$  and  $\gamma = 2\pi \times 21 \text{ MHz}$ .

with the *saturation parameter*  $S = \frac{\Omega_0^2/2}{\Delta^2 + \gamma^2/4}$ . It is now straight forward to obtain  $\rho_{22}$ , the fraction of the population, which can be found in the excited state, as  $\rho_{22} = \frac{(w+1)}{2} = \frac{S}{2(1+S)}$ , and explicitly

$$\rho_{22} = \frac{\Omega_0^2}{4\Delta^2 + \gamma^2 + 2\Omega_0^2}. \quad (2.22)$$

All cases considered in this thesis are far detuned, i.e.  $\Delta^2 \gg \Omega_0^2$ , and  $\Delta^2 \gg \gamma^2$ . This allows for the further simplification of Eq. 2.22,

$$\rho_{22} \approx \frac{\Omega_0^2}{4\Delta^2} = p^{(ex)}. \quad (2.23)$$

Here, the symbol  $p^{(ex)}$  is introduced, as Eq. 2.23 describes the probability that the two-level system is in the excited state after off-resonant interaction. It is remarkable, that in the regime considered here  $p^{(ex)}$  is completely independent of the transition's natural linewidth  $\gamma$ , and is only described by the squared ratio of the Rabi frequency  $\Omega_0$  and the detuning  $\Delta$ . Eq. 2.23 is the key relation to evaluate the absorptive light - ion interaction in chapter 3. To validate the applicability of the approximate solution, plots of Eqs. 2.22 and 2.23 are compared in Fig. 2.3.

### 2.2.3. Ions in Paul Traps: A Two Level System in a Harmonic Potential

When describing experiments with ions in Paul traps, it is not sufficient to only consider their internal states. The trapping potential gives rise to another, external degree of freedom, which needs to be taken into account as well. The emerging possibility of interacting with both the internal electronic state and the external motional state of the ion is the core of many spectacular theoretical and experimental results in quantum optics from the last two decades [SK03, Rie04, Lei05, Häf08].

A system of one ion with two internal states in a one-dimensional harmonic potential, interacting with a single mode, running-wave laser field is described by the Hamiltonian [Roo00, Lei03a]

$$\begin{aligned}\hat{H} &= \hat{H}_0 + \hat{H}_i \\ \hat{H}_0 &= \hbar\omega_0\hat{\sigma}_z + \hbar\omega_{ho}\left(\hat{a}^\dagger\hat{a} + \frac{1}{2}\right) \\ \hat{H}_i &= \frac{1}{2}\hbar\Omega_0(\hat{\sigma}^+ + \hat{\sigma}^-)\left(e^{i(k\hat{x}-\omega t)} + e^{-i(k\hat{x}-\omega t)}\right),\end{aligned}\tag{2.24}$$

where  $\hat{\sigma}_z$  is the respective Pauli matrix,  $\hat{\sigma}^+$  and  $\hat{\sigma}^-$  are the atomic raising and lowering operators, and  $\hat{a}^\dagger$  and  $\hat{a}$  are the creation and the annihilation operator of the harmonic oscillator [Har06].  $\omega_{ho}$  denotes the frequency of the harmonic oscillator,  $k$  is the laser field's wavenumber and  $\hat{x}$  is the position operator,

$$\hat{x} = \sqrt{\frac{\hbar}{2m\omega_{ho}}}(\hat{a}^\dagger + \hat{a}),\tag{2.25}$$

with  $m$  being the ion's mass.

Similarly to chap. 2.1, a transformation to the interaction picture of  $\hat{H}$  with respect to  $\hat{H}_0$ , and a RWA can be performed, which yields [Roo00]

$$\hat{H}_I = \frac{1}{2}\hbar\Omega_0\left(e^{i\eta(\hat{a}'^\dagger + \hat{a}')} \hat{\sigma}^+ e^{-i\Delta t} + e^{-i\eta(\hat{a}'^\dagger + \hat{a}')} \hat{\sigma}^- e^{i\Delta t}\right).\tag{2.26}$$

Here,  $\hat{a}' = \hat{a}e^{i\omega_{ho}t}$  has been introduced, together with the *Lamb-Dicke parameter*,

$$\eta = k\sqrt{\hbar/2m\omega_{ho}}.\tag{2.27}$$

In the Lamb-Dicke regime, defined by  $\eta\sqrt{\langle(\hat{a}^\dagger + \hat{a})^2\rangle} \ll 1$  [Lei03a], the wave packet size is much smaller than the wavelength of the driving laser. In this case, the exponential in Eq. 2.26 can be considerably simplified using a Taylor expansion,

$$\hat{H}_I \approx \frac{1}{2}\hbar\Omega_0\hat{\sigma}^+e^{-i\Delta t}\left(1 + \eta\hat{a}e^{i\omega_{ho}t} + \eta\hat{a}^\dagger e^{-i\omega_{ho}t}\right) + h.c. \quad (2.28)$$

Eq. 2.28 provides a very insightful interpretation of the dynamics in that kind of system. Depending on the detuning  $\Delta$ , there are three specific cases:

- $\Delta = 0$

In the resonant case, the terms which couple the internal state to the motional mode are heavily suppressed, and effectively only the Hamiltonian of the bare two-level system remains:

$$\hat{H}_I^{car} \approx \frac{1}{2}\hbar\Omega_{car}(\hat{\sigma}^+ + \hat{\sigma}^-) \quad (2.29)$$

This *carrier transition* couples the states  $|g, n\rangle$  and  $|e, n\rangle$ .

- $\Delta = +\omega_{ho}$

When the laser fields frequency is detuned to the red side by just the frequency of the harmonic oscillator, the part which was dominant in the resonant case cancels out, and the Hamiltonian effectively reads:

$$\hat{H}_I^{rsb} \approx \frac{1}{2}\hbar\Omega_{rsb}(\hat{\sigma}^+\hat{a} + \hat{\sigma}^-\hat{a}^\dagger) \quad (2.30)$$

This *red sideband transition* coherently couples the state  $|g, n\rangle$  to the state  $|e, n-1\rangle$ , i.e. exciting the internal state also always subtracts one excitation quantum to the external motional state. This mechanism is the basis for all sideband cooling techniques [Die89, Roo99, Rei13]. Eq. 2.30 is equivalent to the *Jaynes-Cummings Hamiltonian* known from cavity quantum electrodynamics [Jay63, Har06]

- $\Delta = -\omega_{ho}$

Analogously, the Hamiltonian of the *blue sideband transition* reads:

$$\hat{H}_I^{bsb} \approx \frac{1}{2}\hbar\Omega_{bsb}(\hat{\sigma}^+\hat{a}^\dagger + \hat{\sigma}^-\hat{a}) \quad (2.31)$$

The Hamiltonian from Eq. 2.31 of *anti-Jaynes-Cummings* type [Lei03a] couples  $|g, n\rangle$  to  $|e, n+1\rangle$ , i.e. one additional motional quantum is created upon excitation of the internal state.

All three transitions have their own distinctive effective Rabi frequency,

$$\begin{aligned}\Omega_{car} &\approx \Omega_0(1 - \eta^2 n) \\ \Omega_{rsb} &\approx \eta\sqrt{n}\Omega_0 \\ \Omega_{bsb} &\approx \eta\sqrt{n+1}\Omega_0.\end{aligned}\tag{2.32}$$

However, when the condition for the Lamb-Dicke regime is not fulfilled, the simplification from Eq. 2.28 does not hold, and also higher-order sidebands can be driven [Alo16], i.e. generally the states  $|g, n\rangle$  and  $|e, n \pm m\rangle$  are coupled, with  $m$  being the order of the driven sideband. The respective transition matrix elements  $M_{n+m,n}$  are given by [Win79]

$$M_{n+m,n} = \langle n+m | e^{i\eta(\hat{a}'^\dagger + \hat{a}')} | n \rangle = e^{-\eta^2/2} \eta^{|m|} \mathcal{L}_q^{|m|}(\eta^2) \left( \frac{q!}{(q+m)!} \right)^{1/2} \tag{2.33}$$

$q$  denotes the lesser of  $n$  and  $n+m$  and  $\mathcal{L}_q^m(x)$  are the associated Laguerre polynomials,

$$\mathcal{L}_q^m(x) = \sum_{k=0}^q (-1)^k \frac{(q+m)!}{(q-k)!(m+k)!k!} x^k \tag{2.34}$$

This yields individual Rabi frequencies for each transition,

$$\Omega_{n+m,n} = M_{n+m,n} \Omega_0. \tag{2.35}$$

After trapping and Doppler cooling [Hän75, Win75], the motional state of an ion in a harmonic potential however is not a pure Fock state  $|n\rangle$ , but a *thermal state*. As the three motional degrees of freedom are uncoupled, they can be treated independently, and the ion's occupation of a motional excitation  $n$  follows a one-dimensional thermal distribution  $p_n$  for each degree of freedom. It reads [Lou97]

$$p_n^{(\bar{n})} = \frac{\bar{n}^n}{(\bar{n}+1)^{n+1}}, \tag{2.36}$$

Fig. 2.4 depicts some examples of Eq. 2.36 for different mean excitation numbers  $\bar{n}$ .

The mean excitation number  $\bar{n}$  can be connected to a generalized temperature  $T$  by the following relation,

$$\bar{n} = \frac{k_B T}{\hbar \omega_{ho}}, \tag{2.37}$$

where  $k_B$  denotes the Boltzmann constant. It has to be noted, that the such defined generalized temperature is not equivalent with the temperature defined in standard



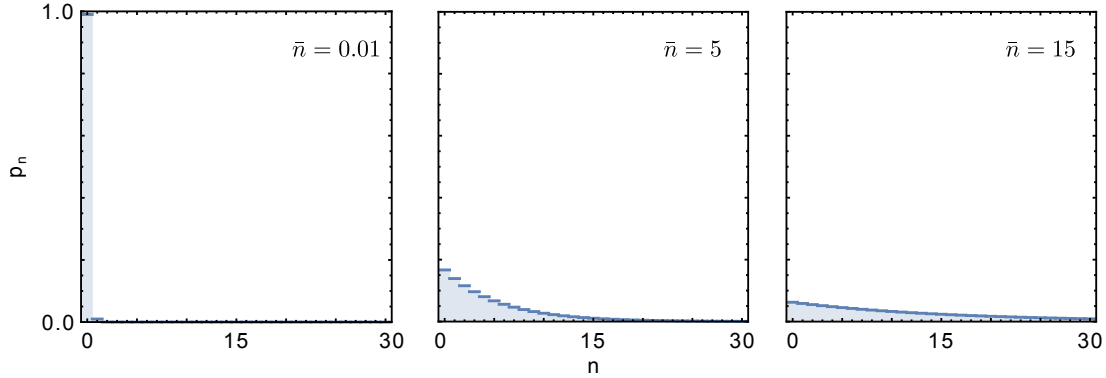


**Figure 2.4.:** Probability distribution of thermal states with mean excitation numbers  $\bar{n}$  of 0.01, 5 and 15. Note, how the the occupation probability of  $n = 0$  is always highest.

thermodynamics, as the mean in Eq. 2.37 is a *temporal* mean, taken over many consecutive, identical realizations of the system, which might only consist of a single particle, whereas standard temperature is defined using the mean of the undirected kinetic energy of a particle *ensemble*. In the remainder of this thesis, whenever the notion of temperature or the attributes cold or hot are used in the context of motional states of single ions or ion crystals, the generalized temperature from Eq. 2.37 is meant.

When describing the dynamics of a thermal state, all different Rabi frequencies from Eq. 2.35 have to be taken into account. To this end, Eq. 2.9 is invoked for all individual Rabi frequencies  $\Omega_{n+m,n}$  and weighted with the respective fraction of the thermal population. This leads to the expression

$$p_{|e\rangle}^{(\bar{n})} = \sum_n p_n^{(\bar{n})} \sin^2 \left( \frac{1}{2} \Omega_{n+m,n} t \right). \quad (2.38)$$

Eq. 2.38 describes coherent dynamics of an ion in a thermal motional state with a mean excitation number  $\bar{n}$  for the cases  $m = 0$  (carrier transitions),  $m = +1$  (first blue sideband transitions) and  $m = -1$  (red sideband transitions). Depictions of those dynamics are shown in Fig. 2.5. It is worth noting, that the oscillation damping observed for higher excitations is not due to incoherent *processes* - at no point in this description any sort of dissipative channel has been considered - but due to an incoherent initial *state*, i.e. the thermal state. This means, to maximize the attainable coherence for a given interaction time, it is desirable to reduce the incoherence of the initial state as far as possible by lowering the amount of motional excitation quanta in the system, and keeping it low during all operations.

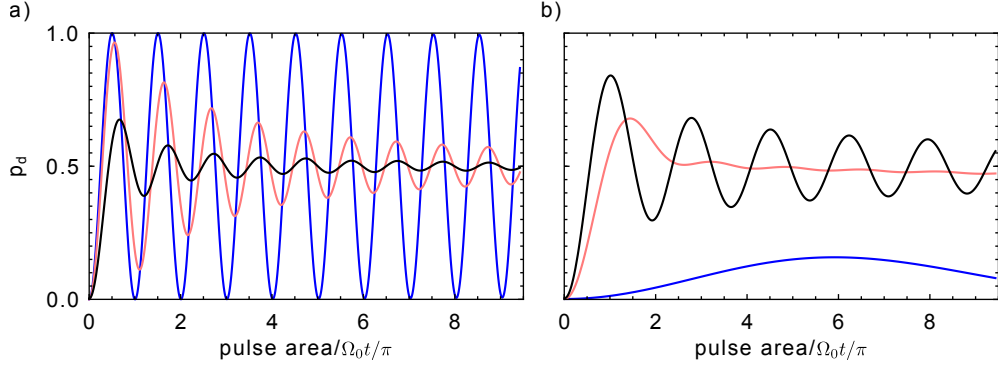


**Figure 2.5.:** Coherent dynamics of a single ion in a thermal motional state for a) carrier transitions and b) red sideband transitions. The mean phonon numbers  $\bar{n}$  are 0.2 (blue curves), 10 (red curves) and 100 (black curves). A higher excited motional state leads to a more pronounced contrast loss of carrier oscillations. A low motional excitation heavily suppresses the dynamics on the red sideband.

### 2.3. Atomic Dipole Matrix Elements & Fermi’s Golden Rule

While the former two sections deal with the interaction of a given two-level system with a light field, two inherent properties of that system itself have not been discussed so far. Those properties are the *reduced dipole matrix element*  $\mathcal{D}$ , which governs how much the two levels of the system in question are coupled, and the already mentioned spontaneous decay rate  $\gamma$ . In this section, it is shown that those two quantities are inherently connected, and can be understood just as two different descriptions of the same physical feature. The underlying mechanism is widely known as “Fermi’s Golden Rule” in the literature. It has first been stated by Dirac [Dir27, Vis09], descriptions using a more modern nomenclature can be found in various quantum mechanics textbooks [Bud08, Bra92, MK13]. The treatment given here starts in general fashion, and later the specifics for the  $4^2P_{1/2}$  level in  $^{40}\text{Ca}^+$  are included.

The starting point for understanding that mechanism is a Hamiltonian consisting of two parts:

$$\hat{H} = \hat{H}_0 + \hat{V} \quad (2.39)$$

As in Eq. 2.1, the first part  $\hat{H}_0$  describes the unperturbed system, which features the energy eigenstates  $|\psi_n\rangle$ ,

$$\hat{H}_0 |\psi_n\rangle = \hbar\omega_n |\psi_n\rangle. \quad (2.40)$$

The second part  $\hat{V}$  is a small perturbation in the sense of perturbation theory [Bra92], which couples the energy eigenstates, i.e. enables transitions between them.

An arbitrary state  $|\psi\rangle$  can now be expressed in the basis of the energy eigenstates  $|\psi_n\rangle$ ,

$$|\psi\rangle = \sum_n c_n |\psi_n\rangle e^{-i\omega_n t}, \quad (2.41)$$

where  $c_n$  are the coefficients of  $|\psi\rangle$  in that basis. The Schrödinger equation 2.3 now reads

$$i\hbar \sum_n [\dot{c}_n |\psi_n\rangle e^{-i\omega_n t} - i\omega_n c_n |\psi_n\rangle e^{-i\omega_n t}] = \quad (2.42)$$

$$\sum_n [c_n \hbar \omega_n |\psi_n\rangle - \hat{V} |\psi_n\rangle c_n e^{-i\omega_n t}]. \quad (2.43)$$

Multiplying from the left side with  $\langle\psi_m| e^{i\omega_m t}$  and comparing coefficients yields

$$\dot{c}_m = -\frac{i}{\hbar} \sum_n \langle\psi_m| \hat{V} |\psi_n\rangle e^{i\omega_{mn} t} c_n, \quad (2.44)$$

where  $\omega_{mn} = \omega_m - \omega_n$  is a short notation for the transition frequency between the eigenstates  $m$  and  $n$ .

The differential equation 2.44 describes how one specific energy eigenstate  $|\psi_m\rangle$  changes, when it is coupled to all other energy eigenstates  $|\psi_n\rangle$  by  $\hat{V}$ , the perturbative part of the Hamiltonian  $\hat{H}$ . The generality of Eq. 2.44 makes it hard to make concrete predictions, so it makes sense at this point to focus on our specific problem of interest. Instead of taking into account the influence of *all* energy eigenstates  $|\psi_n\rangle$ , only *one* initial energy eigenstate  $|i\rangle$  of those is considered from now on. This means  $c_n(t=0) = 1$ . Furthermore,  $c_n$  is considered only slowly changing with time, thus  $c_n(t) \approx 1$ . With the final state  $|\psi_m\rangle$  now denoted by  $|f\rangle$ , Eq. 2.44 simplifies to

$$\dot{c}_f = -\frac{i}{\hbar} \langle f | \hat{V} | i \rangle e^{i\omega_{fi} t}. \quad (2.45)$$

If  $\hat{V}$  is taken to be time dependent in the sense, that it is “switched on” at time  $t' = 0$  and “switched off” again at  $t' = t$ , Eq. 2.45 can be readily integrated,

$$c_f = -\frac{i}{\hbar} \frac{\sin(\omega_{fi} t/2)}{\omega_{fi}} 2V_{fi} e^{i\omega_{fi} t/2}. \quad (2.46)$$

Here  $V_{fi} = \langle f | \hat{V} | i \rangle$  is the *transition matrix element* of the perturbative part of the Hamiltonian, which couples the states  $|f\rangle$  and  $|i\rangle$ .  $|c_f|^2$  yields the population probability  $p_f$  of the final state,

$$p_f = |c_f|^2 = \frac{4}{\hbar^2} V_{fi}^2 \frac{\sin^2(\omega_{fi} t/2)}{\omega_{fi}^2}. \quad (2.47)$$

## 2. Theoretical Foundations

---

In the end, the quantity of interest is not population probability  $p_f$ , but the transition rate  $W_{fi} = \dot{p}_f$ ,

$$W_{fi} = \dot{p}_f = \frac{2}{\hbar^2} V_{fi}^2 \frac{\sin(\omega_{fi}t)}{\omega_{fi}} \quad (2.48)$$

Now, not only a singular final state  $|f\rangle$ , but a multitude of possible final states is considered. The density of those final states is  $\rho(E) = dn/dE$ , where  $dn$  is the number of those states in the energy interval  $dE = \hbar d\omega$ . The cardinal sine shape of Eq. 2.48 makes sure, that only transitions with frequencies in the vicinity of  $\omega_{fi}$  play a role. The expression for the transition rate then becomes

$$W_{fi} = \frac{2}{\hbar} V_{fi}^2 \int_{-\infty}^{\infty} \rho(E) \frac{\sin(\omega_{fi}t)}{\omega_{fi}} d\omega. \quad (2.49)$$

Finally, the assumption is made, that the change of  $\rho(E)$  with respect to  $\omega_{fi}$  is much slower than the cardinal sine under the integral, and therefore can be treated as constant. Integration leads to the expression, which is known as *Fermi's Golden Rule*,

$$W_{fi} = \frac{2\pi}{\hbar} V_{fi}^2 \rho(E). \quad (2.50)$$

It directly connects the transition rate  $W_{fi}$  with the matrix element of that transition  $V_{fi}$ , the probably most remarkable feature being its time-independence.

As the form of Eq. 2.50 is very general, it will be explained in the following, how it can be applied to determining the connection between the decay rate  $\gamma_{PS}$ , i.e. the natural linewidth of a short lived excited atomic state (here, the  $4^2P_{1/2}$  level of  $^{40}\text{Ca}^+$ ) and the reduced dipole matrix element  $\mathcal{D}$  of the respective transition. In that specific case, the initial state  $|i\rangle$  of the system translates to the ion being in the excited  $4^2P_{1/2}$  - state, with no photon being yet emitted in any mode  $\mathbf{k}$  of free space, i.e.  $|i\rangle = |e, 0_{\mathbf{k}}\rangle$ . The final state  $|f\rangle$  the system decays into is the ion being in its ground state, the  $4^2S_{1/2}$  - state, with one photon emitted in the mode  $\mathbf{k}$ , i.e.  $|f\rangle = |g, 1_{\mathbf{k}}\rangle$ . As the ion is considered to be in vacuum, not interacting with any additional external electrical field, the only perturbing field existent is the vacuum field  $\mathcal{E}_{vac}$ . Its quantity in a mode volume  $\mathcal{V}$  follows from normalization arguments [Har06, Fox06] to be

$$\mathcal{E}_{vac} = \sqrt{\frac{\hbar\omega}{2\epsilon_0\mathcal{V}}}. \quad (2.51)$$

This field interacts with the reduced dipole matrix element  $\mathcal{D}$  of the respective transition. The transition matrix element  $V_{fi}$  of the resulting electric dipole interaction reads

$$V_{fi} = \langle \mathcal{D} \mathcal{E}_{vac} \rangle. \quad (2.52)$$

Written more explicitly, one arrives at

$$V_{fi}^2 = \frac{1}{3} \mathcal{D}^2 \mathcal{E}_{vac}^2 = \frac{\mathcal{D}^2 \hbar \omega}{6 \epsilon_0 \mathcal{V}}, \quad (2.53)$$

with the factor  $1/3$  appearing due to averaging over all possible field directions.

The density of states  $\rho(E) = dn/dE$ <sup>1</sup> for the considered process consists of the density of photon states  $\rho_p(\omega)$  in three dimensions [Fox06], and the multiplicity  $2S + 1 = 2$  of the ion's  $4^2S_{1/2}$  ground state:

$$\rho(E) = \rho_p(\omega)(2S + 1) = 2 \frac{\omega^2 \mathcal{V}}{\pi^2 c^3} \quad (2.54)$$

Now, Eq. 2.50 can be used to obtain the following expression for connecting the transition dipole moment  $\mathcal{D}$  and the decay rate of the excited state  $\gamma_{PS}$ ,

$$\mathcal{D}^2 = 2\gamma_{PS} \frac{3\epsilon_0 \hbar}{8\pi^2} \lambda^3, \quad (2.55)$$

where the right hand side only consists of physical constants together with the experimentally accessible quantities  $\gamma_{PS}$  and  $\lambda$ . Note, that  $\mathcal{D}$  from Eq. 2.55 is independent from angular momentum considerations, i.e.  $\mathcal{D}$  is the *reduced* dipole matrix element of that transition. For the treatment of transitions between different Zeeman sublevels, the corresponding Clebsch-Gordan coefficients need to be taken into account as given by the Wigner-Eckart-Theorem [Sak13].

## 2.4. Segmented Ion Trap Fundamentals

The electrical charge of an ion provides an obvious handle for its spacial confinement by means of electrical fields. However, from Maxwell's equations follows the Laplace condition for the electrostatic potential,

$$\Delta \Phi = 0, \quad (2.56)$$

which means, no confining electrostatic potential is possible in all three dimensions at the same time. If a potential is confining in two dimensions, Eq. 2.56 dictates, that it will be anti-confining in the third. There exist two possibilities to circumvent that limitation. First, an additional magnetic field can be applied. Devices which operate in that way to trap ions are known as *Penning traps* [Bro86]. Second, a non-static

<sup>1</sup>Note, that there exist also deviating definitions for the density of states, e.g.  $\tilde{\rho}(E) = \frac{1}{V} \frac{dn}{dE}$

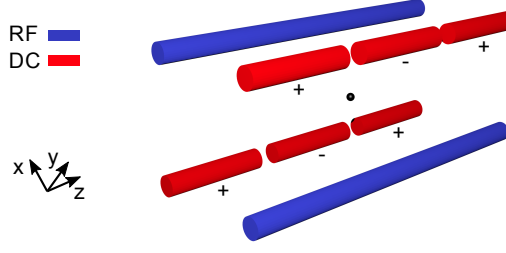


**Figure 2.6.:** Linear Paul trap; Radial confinement is provided by the RF field, axial confinement by suitable voltages in the DC electrodes.

electrical field is used to create average effective confining potential. Those devices are known as *Paul traps* [Pau90]. As these are used throughout this thesis, their operational principles will be outlined in the following.

An electrode structure, like the one shown in Fig. 2.6, to which the DC voltage  $U_{dc}$  and the sinusoidal AC voltage  $U_{rf} \cos(\omega_{rf}t)$  are applied, creates an electric potential  $\Phi(\mathbf{r}, t)$  at position  $\mathbf{r}$  at time  $t$ , which reads

$$\Phi(\mathbf{r}, t) = \frac{U_{dc}}{2} \sum_i \alpha_{dc,i} r_i^2 + \frac{U_{rf}}{2} \cos(\omega_{rf}t) \sum_i \alpha_{rf,i} r_i^2 \quad i = x, y, z. \quad (2.57)$$

In the case of ion traps,  $\omega_{rf}$  is typically in the radio frequency (RF) range between 10 MHz and 100 MHz. The potential curvatures  $\alpha_{dc,i}$  and  $\alpha_{rf,i}$  depend on the geometry and the spacial position of the electrode structure. Obeying Eq. 2.56, there exist several sets of those factors describing electrode structures which can be used as an ion trap. The traps used for the experiments described in this thesis are variants of *linear Paul traps* [Lei03a], which feature the geometry factors  $\alpha_{dc,x} + \alpha_{dc,y} = -\alpha_{dc,z}$ ,  $\alpha_{rf,x} = -\alpha_{rf,y}$  and  $\alpha_{rf,z} = 0$ . This trap is a modification of a quadrupole mass filter, as there is a confining radio frequency potential along the x- and the y direction, but not in the z direction. The confinement in that last direction is provided by DC voltages on dedicated DC electrodes. A simplified structure of a linear Paul trap is shown in Fig. 2.6.

The necessary condition for an electrode structure to work as a Paul trap is the existence of a stable solution for the equations of motion,  $m\ddot{\mathbf{r}} = -e\nabla\Phi$  [Pau90]. For the linear electrode structure, their uncoupled form can be written as

$$\frac{d^2\tilde{r}}{d\xi^2} + [a_{\tilde{r}} - 2q_{\tilde{r}} \cos(2\xi)] \tilde{r}(\xi) = 0, \quad (2.58)$$

with  $\tilde{r} = x, y$  and  $\xi = \omega_{rf}t/2$ . Eq. 2.58 have the form of Mathieu differential equations. For readability, the parameters  $a_{\tilde{r}}$  and  $q_{\tilde{r}}$  are introduced. They read

$$\begin{aligned} a_x &= \frac{4|q|U_{dc}\alpha_{dc,x}}{m\omega_{rf}^2} & a_y &= -\frac{4|q|U_{dc}\alpha_{dc,y}}{m\omega_{rf}^2} \\ q_x &= -\frac{2|q|U_{rf}\alpha_{rf,x}}{m\omega_{rf}^2} & q_y &= \frac{2|q|U_{rf}\alpha_{rf,y}}{m\omega_{rf}^2}. \end{aligned} \quad (2.59)$$

The solution

$$\tilde{r}(t) = \tilde{r}_0 \cos\left(\frac{\beta_{\tilde{r}}}{2}\omega_{rf}t\right) \left(1 + \frac{q_{\tilde{r}}}{2} \cos(\omega_{rf}t)\right) \quad (2.60)$$

is stable, i.e. the ion's trajectory is confined to a finite volume for all times, if  $0 \leq \beta_{\tilde{r}} \leq 1$ . There is no closed form available for  $\beta_{\tilde{r}}$ , but in the lowest order approximation [Roo00], it reads  $\beta_{\tilde{r}} \approx \sqrt{a_{\tilde{r}} + q_{\tilde{r}}^2/2}$ . Eq. 2.60 consists of two superimposed oscillations, the *secular motion* at frequency  $\omega_{rf}\beta_{\tilde{r}}/2$  and the *micromotion* at frequency  $\omega_{rf}$ .

In many cases the explicit trajectory of the ion is not of further interest and approximations treating the trapping potential as an effective harmonic *pseudopotential*. For the radial directions this can be achieved by using the concept of a *ponderomotive force*. One can then define the pseudopotential  $\Phi_{eff}$ , which reads

$$\Phi_{eff} = \frac{|e||\nabla\Phi|^2}{4m\omega_{rf}^2}. \quad (2.61)$$

The confinement in the axial direction is provided by the the static voltages on the DC electrodes. From Eq. 2.57 one obtains a harmonic potential in z direction with frequency  $\omega_z$ , which reads

$$\omega_z = \sqrt{\frac{|q|U_{dc,z}}{m}} \quad (2.62)$$

The linear Paul trap described so far is typically used for trapping single ions or ion chains, the possibilities of moving ions in theses devices is limited. To that end, the concept has been extended, and *segmented* linear Paul traps have been developed [Kie02, Ami10]. These devices do not feature only one pair of DC electrodes to obtain an axial trapping potential, but a larger number of those, each possibly being set to a different DC voltage. Each electrode gives then rise to one distinctive potential along the trap axis, which in the end add up to one resulting axial potential. Control over the different DC voltages thus allows for tailoring the resulting potential in time, e.g. for trapping ions at different axial trap locations or for transporting or splitting ion crystals [Wal12, Bow12, Rus14]. These techniques have found wide use,

most prominently in the ongoing pursuit to further scale up ion trapping technology for quantum information processing purposes, but also for other applications, which require advanced control of the trap's potential landscape [Jac16, Har11].

To calculate the resulting potential  $\Phi(x_i)$  at the positions  $x_i$ , which is generated by  $N$  electrodes, the matrix  $A_{x_i,j}$  is defined. It describes the electric potential of electrode  $j$ , at the position  $x_i$ , if a DC voltage of 1V is applied. Upon applying the voltages  $U_j$  to the respective electrodes, the resulting potential reads

$$\Phi(x_i) = \sum_j^N A_{x_i,j} U_j. \quad (2.63)$$

Eq. 2.63 shows, that the ability to relate  $\Phi(x_i)$  and  $U_j$  depends on the knowledge of the matrix  $A(x_i, j)$  (or its inverse, respectively). This can be achieved by using appropriate simulation software packages, like the one from [Sin10], where the boundary element method [Poz02] in conjunction with the fast multipole method [Gre97] is used to calculate  $A(x_i, j)$  for a given electrode structure.



## 3. Measurement of Dipole Matrix Elements

### 3.1. The $^{40}\text{Ca}^+$ Level Scheme

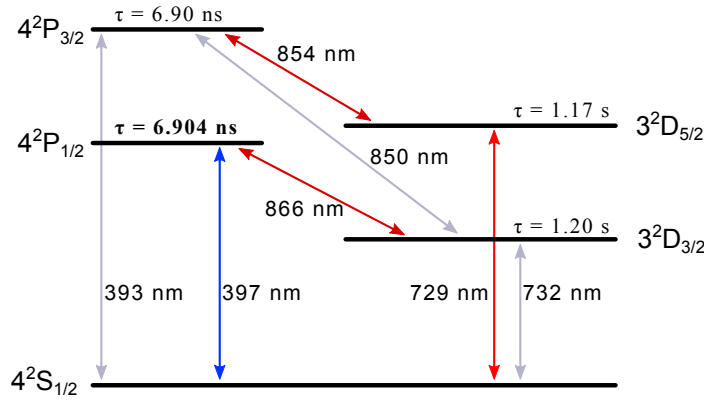


**Figure 3.1.:** Simplified level scheme of  $^{40}\text{Ca}^+$ , together with the wavelengths of the respective transitions and the radiative lifetimes of the excited states. Zeeman splittings are not shown, transitions, which are not driven by laser fields in the context of this thesis are depicted in grey. The lifetime of the  $4^2P_{1/2}$ -level is a result from this work, values for the other lifetimes have been taken from [Kre05, Jin93].

All experiments described in this thesis use singly positively ionized Calcium-40 ( $^{40}\text{Ca}^+$ ) as an atomic species. It is produced by isotope-selective photoionization of neutral Calcium, where one laser close to 423 nm resonantly excites the atom from its  $4s^1S_0$  ground state to the  $4p^1P_1$  excited state, and in a second step from there to the continuum using a laser field near 375 nm, see [Gul01] for details.

Ionized earth-alkaline species are very similar in their atomic structure to neutral alkaline species. They feature a hydrogen-like level scheme due to their single valence electron. The imperfect shielding of the core charges by the inner electrons in  $^{40}\text{Ca}^+$  however leads to a notable feature not found in Hydrogen, namely the existence of metastable states. Those states have a very long lifetime, and consequentially the respective transitions have a very small linewidth. These two features are key for not

only various applications in quantum information processing, but also for performing the precision measurements discussed in this thesis. Fig. 3.1 shows a simplified level scheme of  $^{40}\text{Ca}^+$ . This isotope has zero nuclear spin and therefore no hyperfine splitting is present in its level scheme.

The  $4^2S_{1/2}$  level can be coupled to the two excited levels  $4^2P_{1/2}$  and  $4^2P_{3/2}$  with radiation close to 397 nm and 393 nm respectively. Both states are short lived, and the  $4^2P_{1/2}$  is used for Doppler cooling. Both excited states have additional decay channels to the  $3^2D_{3/2}$  and the  $3^2D_{5/2}$  levels. The transitions from the  $4^2S_{1/2}$  to the metastable levels  $3^2D_{3/2}$  and  $3^2D_{5/2}$  are dipole-forbidden, but quadrupole transitions are possible using laser fields with sufficiently narrow linewidths and high enough power.

As the only decay channels of the two D-states are quadrupole transition, the radiative lifetimes of  $\sim 1$  s for both D-levels are rather long compared to those of the P-levels, which are short-lived. An updated value for the radiative lifetime of the  $4^2P_{1/2}$  level with a value of 6.904(26) ns is one result of the measurements discussed in this thesis.

The transition wavelengths of all transitions are accessible by commercially available grating-stabilized narrow-linewidth external cavity diode lasers (ECDLs). However, the increased demands concerning the optical power, linewidth and the frequency stability of the laser used for the quadrupole transition close to 729 nm make the use of a titanium sapphire (Ti:Sa) laser system beneficial. In the remainder of this thesis, both systems have been used. A Ti:Sa system for the measurement of the transition matrix elements, and a diode-based system for the trap characterization experiment.

## 3.2. Lasersystem

To control the internal state of the ion, laser sources with the following wavelengths are used: A source near 397 nm is driving the  $S_{1/2} \leftrightarrow P_{1/2}$ , and is used for Doppler cooling, state detection and optical pumping. The repumper close to 866 nm keeps population out of the  $D_{3/2}$  state during Doppler cooling and detection. In the context of the matrix element measurement, the laser driving the  $S_{1/2} \leftrightarrow D_{5/2}$  quadrupole transition at about 729 nm is used for optical pumping and electron shelving. The quenching of the  $D_{5/2}$  is done by means of a source near 854 nm. A Raman transition between the two ground states is driven using another source close to 397 nm, but detuned by  $\sim 10$  GHz from resonance. The same source is used for inducing the off-resonant dispersive and absorptive interactions, which form the basis for the determination of the transition's reduced matrix element.

All laser sources are commercially available ECDLs, except for the source at 375 nm, which is a not grating stabilized diode, and the source of the 729 nm light, which is a Ti:Sa laser system<sup>1</sup>. The source close to 397 nm used for Doppler cooling, detection and optical pumping as well as the source close to 866 nm for repumping are frequency locked to reference cavities to prevent long-term drifting using the Pound-Drever-Hall (PDH) technique [Dre83, Bla01, Tha99]. The Ti:Sa source providing the light close to 729 nm is locked to a high-Finesse cavity for drift prevention and linewidth reduction [Mac12]. The sources running close to 423 nm, 854nm and the second, off-resonant source running close to 397 nm are free running, their wavelengths are monitored on a commercial wavemeter<sup>2</sup> and adjusted automatically or manually if necessary. For mode cleaning and transportation of the laser fields, commercial polarization maintaining optical fibers (PMFs) or single mode fibers (SMFs)<sup>3</sup> are used. As all the diode lasers are provide enough power, those are shared with a second, independent trapping setup, the Ti:Sa source is even shared with a third experiment. The second off-resonant source close to 397 nm is an exception, as all available power is needed for the experiments here. The whole laser setup is designed such that the maximum available power of each beam is much higher than the power, which is actually needed for operation, so that the setup can be operated even under suboptimal conditions. All reported powers are always typical values achievable in prolonged operation, never absolute maximum values.

### 3.2.1. Doppler Cooling, State Detection and Optical Pumping (397 nm)

Up to 20 mW of laser light with a wavelength close to 397 nm for driving the  $S_{1/2} \leftrightarrow P_{1/2}$  dipole transition close to resonance are provided by an ECDL<sup>4</sup>. This light is used for Doppler cooling of the ion, state detection by fluorescence and optical pumping. The optical setup is depicted in Fig. 3.2. Directly after the light leaves the ECDL, two small fractions of the output light are extracted from the main beam, one is coupled into a reference cavity for creating a PDH error signal, the other is fed to the wavemeter for monitoring the wavelength. Then, the main beam is divided in two parts, where one part is diverted to another independent setup. The remaining part is split between two branches, one being used for Doppler cooling and fluorescence detection, and one for optical pumping. Both branches consist of a double pass configuration, which allows not only for fast switching, but also for independent frequency tuning of the branches.

---

<sup>1</sup>Matisse TX, Sirah Lasertechnik GmbH, Heinrich-Hertz Straße 11, 41516 Grevenbroich, Germany

<sup>2</sup>WSU-267, HighFinesse GmbH, Auf der Morgenstelle 14d, 72076 Tübingen, Germany

<sup>3</sup>Schäfter + Kirchhoff GmbH, Kieler Straße 212, 22525 Hamburg, Germany

<sup>4</sup>DL pro design, Toptica Photonics AG, Lochhamer Schlag 19, 82166 Gräfelfing, Germany

### 3. Measurement of Dipole Matrix Elements

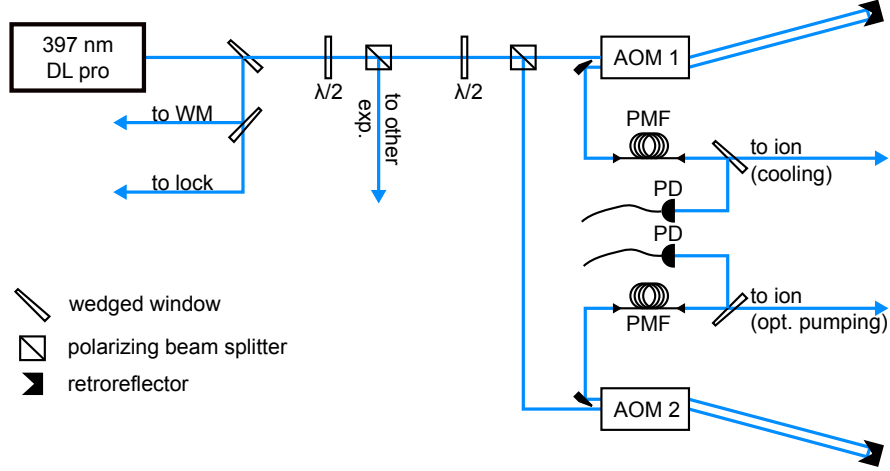


**Figure 3.2.:** Scheme of optical setup providing laser light near 397 nm for Doppler cooling and optical pumping.

The incoming and the outgoing beam of the double passes are separated not by polarization, but geometrically by using D-shaped pickoff mirrors. This allows for keeping the polarization of incoming and outgoing beam constant at that angle, which yields the highest transmission through the acousto-optical modulator (AOM) crystal. For both branches, the outgoing beams are coupled to polarization maintaining fibers (PMF) and are transferred to the respective viewports of the vacuum chamber. There, a small part of each beam is diverted to a photodetector (PD) for monitoring the intensity directly in front of the vacuum window. The beam used for optical pumping is now circularly polarized by means of a  $\lambda/4$  plate. At last, both beams are focused at the position of the ion. The beam waists are on the order of  $200 \mu\text{m}$ . For trap operation, typical powers as measured in front of the vacuum windows are adjusted to be  $150 \mu\text{W}$  for the Doppler beam and  $30 \mu\text{W}$  of optical pumping light.

The frequency of the laser is locked to a reference cavity to prevent slow drifting. This is accomplished by modulating the current driving the laser diode, which creates sidebands in the laser's frequency spectrum. A photodetector measured the light reflected from the reference cavity, and its signal is mixed with the local oscillator in order to produce a Pound-Drever-Hall error signal. A PID regulator uses this error signal as an input, and operates on the laser diode's current as well as on the piezo crystal controlling the angle of the laser's stabilization grating. The radio frequency signal driving the AOMs<sup>5</sup> is derived from two voltage controlled oscillators (VCOs). Their amplitudes are adjusted via voltage variable attenuators (VVAs) and amplified before fed to the AOM assemblies. Using the VCOs and the VVAs, frequency and amplitude of those

<sup>5</sup>I-M110-3C10BB-GH27, Gooch & Housego PLC, Dowlish Ford, Ilminster TA19 0PF, United Kingdom

RF signals can be adjusted by means of external DC voltages. Those are generated by USB-interfaced ADC/DAC devices, connected to the main experimental control PC. The same ADC/DAC devices read the output signals of the intensity monitoring photodetectors, and make them available on the experimental control PC. This system allows for independent adjustment of power and frequency of both the Doppler cooling beam and the beam used for optical pumping, without the need to change the operation parameters of the laser or the locking system.

### 3.2.2. Repumping and Quenching (866 nm & 854 nm)

Two similar ECDL laser systems<sup>6</sup> are used for the generation of the repumping light close to 866 nm and the quenching light close to 854 nm. Both systems deliver about 15 mW each, the optical setup is depicted in Fig. 3.3

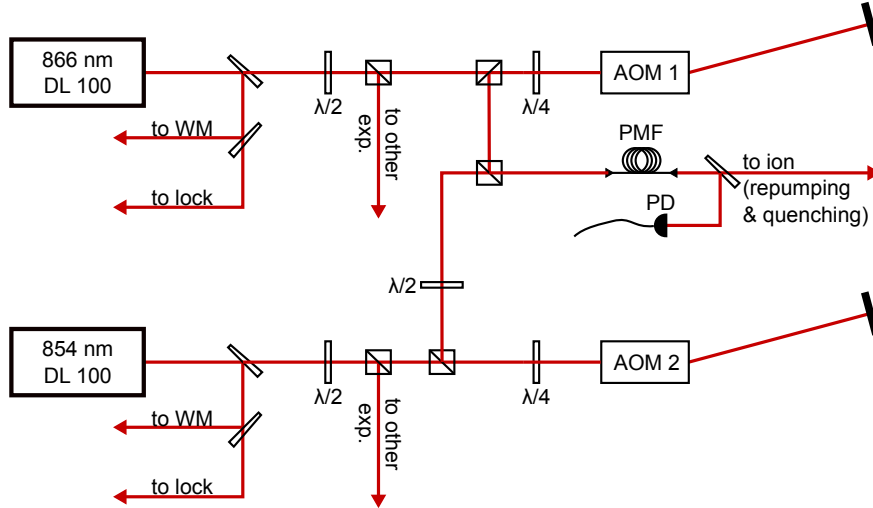


**Figure 3.3.:** Scheme of optical setup providing laser light for repumping near 866 nm and for repumping and quenching near 854 nm.

Like with the 397 nm laser system, a wedged window in each beam is used to couple a small fraction of the light to a wavemeter for wavelength monitoring. Only the repumper laser is locked to an external reference cavity, the quenching laser is left free running. Then both beams are divided, where half of each beam is used for another independent setup. After going through AOMs<sup>7</sup> in double pass configuration, both beams are superimposed, and coupled jointly to a single mode fiber, which delivers the

<sup>6</sup>DL 100, Toptica Photonics AG, Lochhamer Schlag 19, 82166 Gräfelfing, Germany

<sup>7</sup>TEF 80-20 and QZF 80-20, Brimrose Corporation of America, 19 Loveton Circle, Hunt Valley Loveton Center, Sparks, MD. 21152, USA

light to the viewport of the vacuum chamber. For intensity monitoring, a small fraction of the superimposed beams is diverted to a photodetector, before the light is focused to the ion. The power of each beam is adjusted to values between 30 and 200  $\mu\text{W}$ .

Like for the 397 nm setup, the RF signal for driving the in the repumper beam is produced by a VCO, passed through a VVA for amplitude adjustment before amplification. The DC voltages for VCO and VVA are set by the experimental control PC via another ADC/DAC module, allowing for the same frequency and intensity control of the repumper light as for both beams at 397 nm. The AOM in the quenching laser beam path is directly driven by an amplified VCO at fixed Voltage, as no further controls are needed in this case.

#### 3.2.3. Electron Shelving and Optical Pumping (729 nm)

As light close to 729 nm is driving a quadrupole transition, stricter demands concerning the lasers linewidth and frequency drift have to be met. The laser field is produced by a Ti:Sa laser source, which is stabilized to a high-finesse cavity. Details for the setup of that source can be found in [Mac12]. Light from the Ti:Sa setup is coupled to a polarization maintaining fiber, and passes afterwards through an AOM<sup>8</sup> in double pass configuration. The exiting light is delivered to the chamber viewport again by a PMF, where its polarization is adjusted by a  $\lambda/2$  plate and finally focused down to the ion's position. In order to achieve reasonably fast Rabi frequencies on the quadrupole transition, the power of that beam is chosen to be much higher compared to the other laser fields, ranging between 30 and 50 mW.

The AOM is driven by a DDS based RF synthesizer<sup>9</sup>, which is controlled via an USB connection by the experimental control PC.

#### 3.2.4. Coherent Dynamics and Off-resonant Interactions (397 nm)

The intensity requirements for driving off resonant interactions on the  $S_{1/2} \leftrightarrow P_{1/2}$  transition are higher than for those close to resonance. To provide light with a wavelength close to 397 nm with a power on the order of 80 mW, the system depicted in Fig. 3.4 is used. Light from a 793 nm laser diode is going through a tapered amplifier, which results in a total laser power of  $\sim 500$  mW. This light is now frequency doubled by a non-linear crystal in a bow tie cavity, which produces  $\sim 80$  mW of light at the

---

<sup>8</sup>TEM-85-10, Brimrose Corporation of America, 19 Loveton Circle, Hunt Valley Loveton Center, Sparks, MD. 21152, USA

<sup>9</sup>VFG 150, Toptica Photonics AG, Lochhamer Schlag 19, 82166 Gräfelfing, Germany

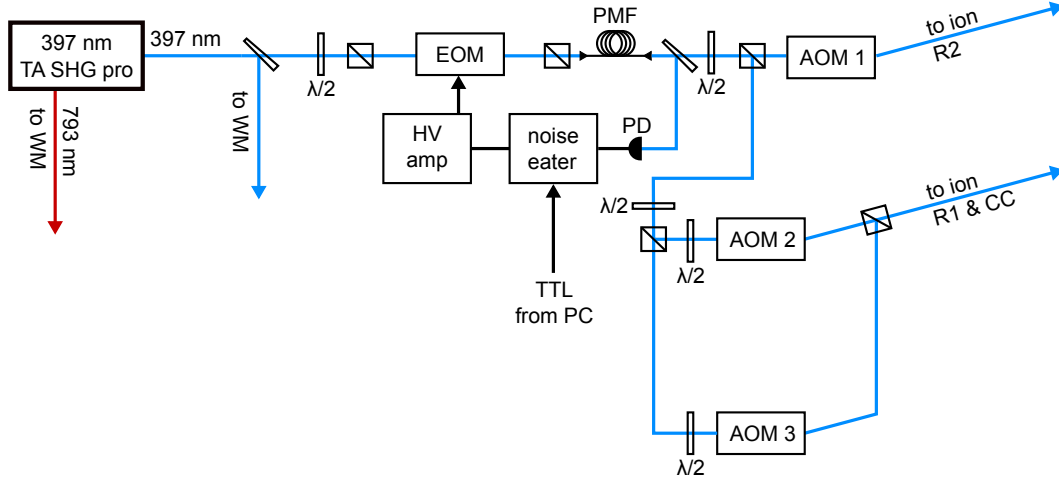


**Figure 3.4.:** Scheme of optical setup providing laser light for the Raman transition between the ground states

target wavelength close to 397 nm. The wavelengths of both the fundamental and the frequency doubled laser field are monitored on the wavemeter. After a  $\lambda/2$  plate for polarization adjustment, the beam passes an electro-optical modulator (EOM)<sup>10</sup>, which is used for intensity stabilization. Now, the beam is coupled to a PMF for mode-cleaning purposes. After the fiber small fraction of the output is sent to PD, whose signal is used for intensity stabilization. Using  $\lambda/2$  plates and PBS, the beam is now divided into three parts, two collinear beams (R1 and CC) for driving coherent dynamics between the two ground states with a Raman scheme, and one beam (R2) is used for inducing the off-resonant absorptive and dispersive interactions. All three beams are sent through AOMs<sup>11</sup> in single pass configuration before being focused on the ion. R1 and CC are superimposed before that to achieve a collinear beam configuration. Around 1 mW of optical power each are used for the R1 and the CC beams, 5 to 10 mW are used in the R2 beam. Those values are intentionally reduced compared to the attainable maxima to give the intensity stabilization plenty of regulation headroom.

The frequency of the laser is not stabilized by means of a reference cavity, as a simple drift correction using the wavemeter has proven to be sufficient. The wavelength of the fundamental beam is constantly read from the wavemeter by a PC. If the wavelength changes more than  $\pm 20$  fm, the PC acts via a DAC on the voltage of the laser grating's adjustment piezo to correct the wavelength to the desired value. The attainable frequency standard error is on the order of 20 MHz (see appendix A for details). The

<sup>10</sup>LM0202, Qioptiq GmbH & Co. KG, Königsallee 23, 37081 Göttingen, Germany

<sup>11</sup>2 x I-M95-3C10BB-GH27 and I-M110-3C10BB-GH27, Gooch & Housego PLC, Dowlish Ford, Ilminster TA19 0PF, United Kingdom

bow tie cavity for frequency doubling is in turn PDH-locked to the frequency of the fundamental mode (for details, see the manual). The intensity stabilization takes the setup's PD signal as an input, and acts on the EOM as the controlling element. The output of a PID controller<sup>12</sup> is amplified<sup>13</sup> to the high voltage necessary to drive the EOM. The setpoint DC voltage is provided by a DAC connected to the experimental control PC. Additionally, a TTL trigger input can switch the PID controlling on and off, which is used in experimental sequences to increase the total light attenuation as compared to AOM-only switching. DDS-based frequency synthesizers provide the RF for driving the AOMs of the R1<sup>14</sup>, CC<sup>14</sup> and R2<sup>15</sup> beams.

#### 3.2.5. Photoionization (375 nm & 423 nm)

An oven assembly in the vacuum provides a continuous beam of neutral Ca, which is isotope-selectively ionized by a two step photoionization scheme. The first excitation from the  $S_0$  to the  $S_1$  state in neutral Ca is driven by a diode laser<sup>16</sup> at a wavelength close to 423 nm, and the second excitation to the continuum is provided by a free running Laser diode<sup>17</sup> at a wavelength of  $\sim 375$  nm. No further means of frequency stabilization are necessary for those two lasers. Both beams are superimposed, and coupled into a common single mode fiber, which delivers 0.5 to 1 mW of each laser at the viewport, where it is focused on the ion. Mechanical shutters are used [Sin02] for switching both laser fields. Two independent independent shutters at the beginning of the beam paths of both lasers are used to prevent bleaching of optical elements due to excessive exposure to UV light. Using that setup typical loading times for single ions are in the order of seconds.

### 3.3. Vacuum Chamber and Imaging System

The vacuum chamber contains calcium ovens [Rot03], the ion trap together with electrical low-pass filters on its DC electrodes, an ion getter pump and a Titanium sublimation pump needed to keep the pressure at ultrahigh vacuum level, as well as a Bayard-Alpert gauge for pressure measurement. Further details concerning vacuum system and trap can be found in [Sch08].

---

<sup>12</sup>Noise Eater, TEM-Messtechnik GmbH, Großer Hillen 38, 30559 Hannover, Germany

<sup>13</sup>HV AMP, TEM-Messtechnik GmbH, Großer Hillen 38, 30559 Hannover, Germany

<sup>14</sup>VFG 150, Toptica Photonics AG, Lochhamer Schlag 19, 82166 Gräfelfing, Germany

<sup>15</sup>SMC100A, Rohde & Schwarz GmbH & Co. KG, Mühldorfstraße 15, 81671 München, Germany

<sup>16</sup>DL pro, Toptica Photonics AG, Lochhamer Schlag 19, 82166 Gräfelfing, Germany

<sup>17</sup>iBeam smart, Toptica Photonics AG, Lochhamer Schlag 19, 82166 Gräfelfing, Germany



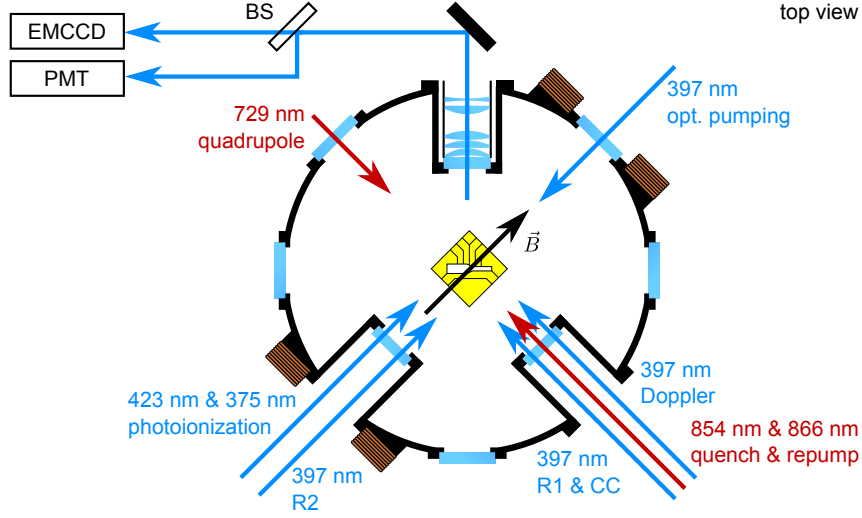


**Figure 3.5.:** Scheme of optical setup providing laser light for the Raman transition between the ground states

The fluorescence of the ion is collected with a high NA objective lens and detected with both a photomultiplier tube<sup>18</sup> and an EMCCD camera<sup>19</sup>. An additional lens in the beampath is used to create an intermediate image, which is used to suppress out-of-focus stray light. The fluorescence light is divided at a beamsplitter,  $\sim 70\%$  are used for PMT detection and  $\sim 30\%$  for camera imaging.

<sup>18</sup>ET P25PC, Electron Tubes Limited, Bury Street, Ruislip, Middlesex HA4 7TA, United Kingdom

<sup>19</sup>Ixon DV860DCS-BV, Andor Technology Ltd., 7 Millennium Way, Springvale Business Park, Belfast BT12 7AL, United Kingdom

### 3.4. Measurement Principle

The method described in this chapter for measuring the dipole matrix element of the  $4^2S_{1/2} \leftrightarrow 4^2P_{1/2}$  transition in  $^{40}\text{Ca}^+$  follows the scheme proposed in [Pos10b]. It relies on the comparison between absorptive and dispersive interactions when subjecting the ion to a laser field off-resonant to that transition.

The *absorptive interaction* of that laser field with the ion manifests itself through an off-resonant excitation, as described in more detail in 2.2.2.

The *dispersive interaction* of the same laser field with the ion manifests itself through an AC-Stark shift, as described in more detail in 2.2.1.

#### 3.4.1. Off-resonant Excitation and the Spin-flip Rates $R_+$ and $R_-$

For describing off-resonant excitation and the resulting inelastic Raman scattering, a good starting point is a view on the probabilities of spontaneous emission events.

The spontaneous emission rate  $R_{SE}$  of a manifold of  $i$  excited atomic states reads [Win03]

$$R_{SE} = \sum_i \gamma_i P_i, \quad (3.1)$$

where the  $\gamma_i$  are the decay rates of the respective states, and  $P_i$  are the occupation probabilities of those states.

Considering now the transitions in  $^{40}\text{Ca}^+$ , the excited state manifold consists of the  $|4^2P_{1/2}, m_s = \pm 1/2\rangle$  states, the decay rate of both being  $\gamma_{PS}$  and the ground state manifold consists of the  $|4^2S_{1/2}, m_s = \pm 1/2\rangle$  states. The ion is initialized in the ground state manifold and subject to off-resonant laser radiation. This means, the occupation probabilities  $P_i$  are the sum of all possible excitation probabilities  $p_i^{(ex)}$  induced by that laser field, as introduced in Eq. 2.23. Thus, Eq. 3.1 becomes

$$R_{SE} = \gamma_{PS} \sum_{i=1}^4 p_i^{(ex)}, \quad (3.2)$$

where the  $p_i^{(ex)}$  are the probabilities of exciting either of the two excited states either via  $\sigma^\pm$ - ( $\Delta m = \pm 1$ ) or  $\pi$ -transitions ( $\Delta m = 0$ ) (see Fig 3.6).

For the described measurement principle, only those scattering events, which change the polarization of the ground state are relevant, i.e. events, where an excitation

via a  $\sigma^\pm$  - transition is followed by a decay via a  $\pi$ -transition and vice versa. Those conditional spin-flip rates read

$$R_+ = \gamma_{PS} \left( p_{\sigma+}^{(ex)} p_{\pi}^{(dec)} + p_{\pi}^{(ex)} p_{\sigma-}^{(dec)} \right) \quad (3.3)$$

$$R_- = \gamma_{PS} \left( p_{\sigma-}^{(ex)} p_{\pi}^{(dec)} + p_{\pi}^{(ex)} p_{\sigma+}^{(dec)} \right), \quad (3.4)$$

where the  $p_{\sigma^\pm}^{(dec)}$  ( $p_{\pi}^{(dec)}$ ) is the probability that a  $\sigma^\pm$ - ( $\pi$ -) transition occurs when the excited state decays.

Making use of expression 2.23, the excitation probabilities  $p_{\sigma^\pm}^{(ex)}$  and  $p_{\pi}^{(ex)}$  are given by

$$p_{\sigma^\pm}^{(ex)} = \frac{\Omega^2}{4\Delta^2} c_{\sigma}^2 \epsilon_{\pm}^2 \quad (3.5)$$

$$p_{\pi}^{(ex)} = \frac{\Omega^2}{4\Delta^2} c_{\pi}^2 \epsilon_0^2. \quad (3.6)$$

The transition's Rabi frequency is denoted by  $\Omega$ , the laser field's detuning from resonance is  $\Delta$ , the polarization components of that laser field are denoted  $\epsilon_{\pm}$ ,  $\epsilon_0$  and  $c_{\sigma}$ ,  $c_{\pi}$  are the Wigner 3-j Symbols of that transition. They are defined as [Bud08]

$$c_{m_S, m_P} = \begin{pmatrix} J_S & 1 & J_P \\ m_s & q & -m_P \end{pmatrix}. \quad (3.7)$$

For the four possible transitions these symbols have the following numerical values.

$$c_{-1/2, 1/2}^2 = c_{1/2, -1/2}^2 = c_{\sigma}^2 = 1/3 \quad (3.8)$$

$$c_{-1/2, -1/2}^2 = c_{1/2, 1/2}^2 = c_{\pi}^2 = 1/6 \quad (3.9)$$

The numerical values for the probabilities, that one of the excited states undergoes a decay via a  $\sigma^\pm$ - or a  $\pi$ -transition,  $p_{\sigma^\pm}^{(dec)}$  and  $p_{\pi}^{(dec)}$  can be obtained as follows:

$$p_{\sigma^\pm}^{(dec)} = \frac{c_{\sigma}^2}{c_{\sigma}^2 + c_{\pi}^2} = 2/3 \quad (3.10)$$

$$p_{\pi}^{(dec)} = \frac{c_{\pi}^2}{c_{\sigma}^2 + c_{\pi}^2} = 1/3 \quad (3.11)$$

### 3. Measurement of Dipole Matrix Elements

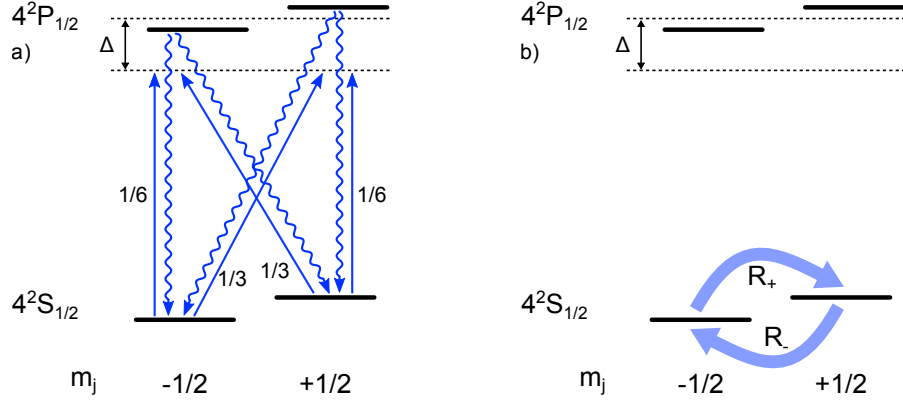


**Figure 3.6.:** Relevant levels and transitions with their respective squared Clebsch-Gordan coefficients (a), which give rise to the conditional spin-flip rates  $R_+$  and  $R_-$  (b).

Using those definitions, the expressions for  $R_{\pm}$  read

$$R_{\pm} = \gamma_{PS} \frac{\Omega^2}{4\Delta^2} \frac{\epsilon_{\pm}^2 + \epsilon_0^2}{9}. \quad (3.12)$$

They describe the rate of change of the ground state polarization when the ion is subject to the off-resonant laser field (see Fig. 3.6). The quantity  $\gamma_{PS}$  is contained in those expressions.

Apart from the decay from the  $P_{1/2}$  manifold to the  $S_{1/2}$  ground states, a second decay channel is present in  $^{40}\text{Ca}^+$ , namely from the  $P_{1/2}$  manifold to the metastable  $D_{3/2}$  manifold. The description of that process is analogous to the decay to the  $S_{1/2}$  ground state.  $R_{+D}$  ( $R_{-D}$ ) is the rate, at which population from the  $|4^2S_{1/2}, m_s = -1/2\rangle$  ( $|4^2S_{1/2}, m_s = +1/2\rangle$ ) state is transferred to the metastable  $D_{3/2}$  manifold:

$$R_{+D} = \gamma_{PD} \frac{\Omega^2}{4\Delta^2} \left( \frac{1}{3}\epsilon_+^2 + \frac{1}{6}\epsilon_0^2 \right) \quad (3.13)$$

$$R_{-D} = \gamma_{PD} \frac{\Omega^2}{4\Delta^2} \left( \frac{1}{3}\epsilon_-^2 + \frac{1}{6}\epsilon_0^2 \right). \quad (3.14)$$

Note, that for  $R_{+D}$  and  $R_{-D}$  it is not relevant, in which exact substate of the  $D_{3/2}$  manifold the excited states decay to. The process is depicted in Fig. 3.7

Both decay channels have to be taken into account, when describing the total population dynamics of the system. In order to simplify the treatment from hereon, an additional condition is imposed on the off-resonant laser field by assuming, that the light is only  $\sigma^{\pm}$ - polarized, i.e.  $\epsilon_0 = 0$ .

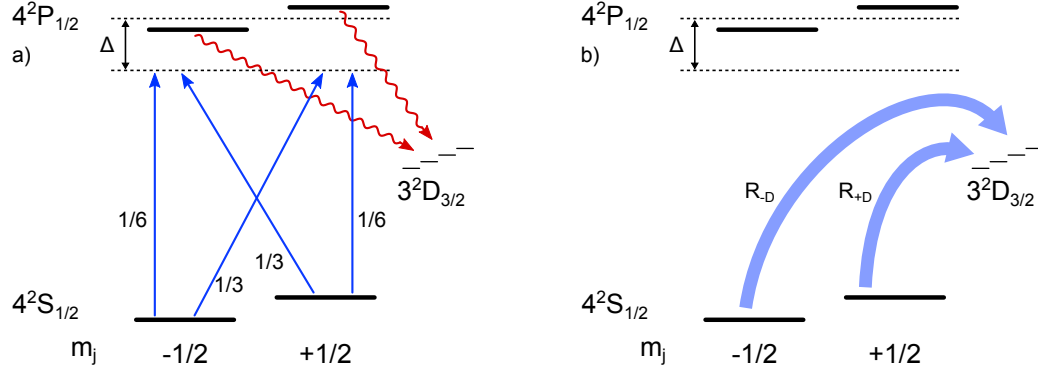


**Figure 3.7.:** Relevant transitions which take part in the decay process to the  $D_{3/2}$  - state (a). This mechanism effectively reduces the total population in the  $S_{1/2}$  - manifold by transferring it to the  $D_{3/2}$  manifold with the rates  $R_{+D}$  and  $R_{-D}$ , where it is lost for further interaction with the off-resonant laser field (b).

In that case, the rates for both decay channels can be connected by

$$R_{\pm} + R_{\pm,D} = R_{\pm}(1 + b) \quad (3.15)$$

where the leak factor  $b = 3\gamma_{PD}/\gamma_{PS}$  is introduced. Instead of fully taking into account the effects of both decay channels separately, this simplification allows for just describing the dynamics of the ground state- and the excited state manifolds with the addition of a constant population leak rate.

The quantities, which are experimentally accessible are the populations  $p_{\uparrow}(t)$  and  $p_{\downarrow}(t)$  of the states  $|\uparrow\rangle$  and the  $|\downarrow\rangle$  as a function of the duration  $t$  the ion is subjected to the off-resonant laser field. The quantities  $R_+$ ,  $R_-$  and  $b$  can now be used to set up rate equations for those state populations:

$$\dot{p}_{\uparrow}(t) = -R_-(1 + b)p_{\uparrow}(t) + R_+p_{\downarrow}(t) \quad (3.16)$$

$$\dot{p}_{\downarrow}(t) = -R_+(1 + b)p_{\downarrow}(t) + R_-p_{\uparrow}(t) \quad (3.17)$$

The solution of Eqs. 3.17 reads

$$\begin{aligned} p_{\uparrow}^{(\uparrow)}(t) &= \frac{1}{\tilde{R}} e^{-\frac{1}{2}\tilde{R}t} \left( \tilde{R} \cosh\left(\frac{\tilde{R}t}{2}\right) - (1 + b)\delta R \sinh\left(\frac{\tilde{R}t}{2}\right) \right) \\ p_{\uparrow}^{(\downarrow)}(t) &= \frac{2}{\tilde{R}} e^{-\frac{1}{2}\tilde{R}t} R_+ \sinh(\tilde{R}t/2), \end{aligned} \quad (3.18)$$

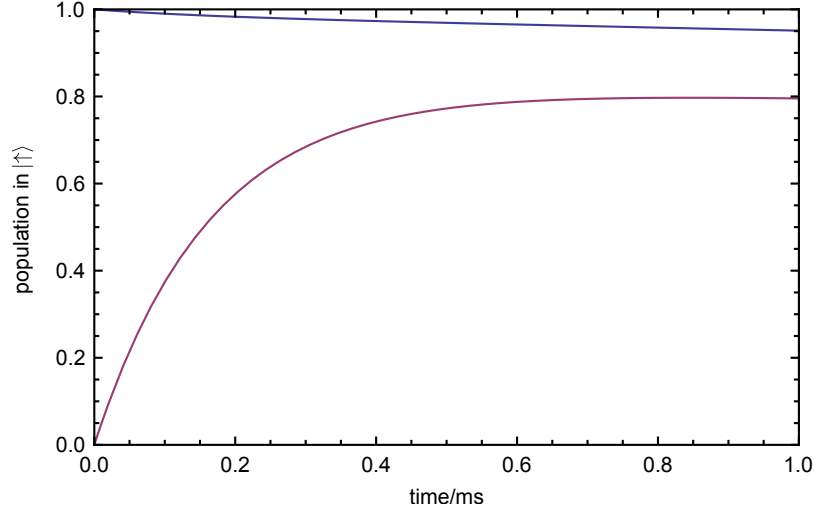


**Figure 3.8.:** Plots of Eqs. 3.18,  $p_{\uparrow}^{(\uparrow)}(t)$  (blue) and  $p_{\uparrow}^{(\downarrow)}(t)$  (red). Parameters are set to values similar to those determined experimentally, being  $R_+ = 2\pi \times 795$  Hz,  $R_- = 2\pi \times 16$  Hz,  $b=0.2$ .

where  $p_{\uparrow}^{(\uparrow)}(t)$  refers to the population in  $|\uparrow\rangle$ , when the ion is initialized in  $|\uparrow\rangle$ , i.e.  $p_{\uparrow}^{(\uparrow)}(t=0) = 1$ , and  $p_{\uparrow}^{(\downarrow)}(t)$  is the population fraction in  $|\uparrow\rangle$  when the ion is initialized in  $|\downarrow\rangle$ , i.e.  $p_{\uparrow}^{(\downarrow)}(t=0) = 0$ . The symbols  $\bar{R} = (1+b)(R_+ + R_-)$  and  $\tilde{R}^2 = \bar{R}^2 - 4b(2+b)R_+R_-$  are used to shorten the notation. Plots of Eqs. 3.18 are shown in Fig. 3.8.

### 3.4.2. The AC-Stark Shift $\Delta_S$

The dispersive interaction of the ion with the laser field manifests itself through an AC-Stark shift, which is derived in Eq. 2.11. Both ground states  $|\uparrow\rangle$  and  $|\downarrow\rangle$  experience different Stark shift, depending on the polarization of the laser field. Scaled with the appropriate Wigner 3-j Symbols from Eq. 3.9 for the different laser polarizations, they read

$$\Delta_S^{\uparrow} = \frac{\Omega^2}{4\Delta} \left( \frac{1}{3}\epsilon_- + \frac{1}{6}\epsilon_0 \right) \quad (3.19)$$

$$\Delta_S^{\downarrow} = \frac{\Omega^2}{4\Delta} \left( \frac{1}{3}\epsilon_+ + \frac{1}{6}\epsilon_0 \right) \quad (3.20)$$

Experimentally, the differential AC-Stark shift  $\Delta_S = \Delta_S^{\downarrow} - \Delta_S^{\uparrow}$  is determined by a spin-echo measurement [Häf03]. The coherent dynamics between the two ground states necessary for that measurement scheme are driven by a two-photon Raman transition [Pos10b, Mon95], realized by two laser fields near 397 nm, off-resonant to the  $S_{1/2} - P_{1/2}$

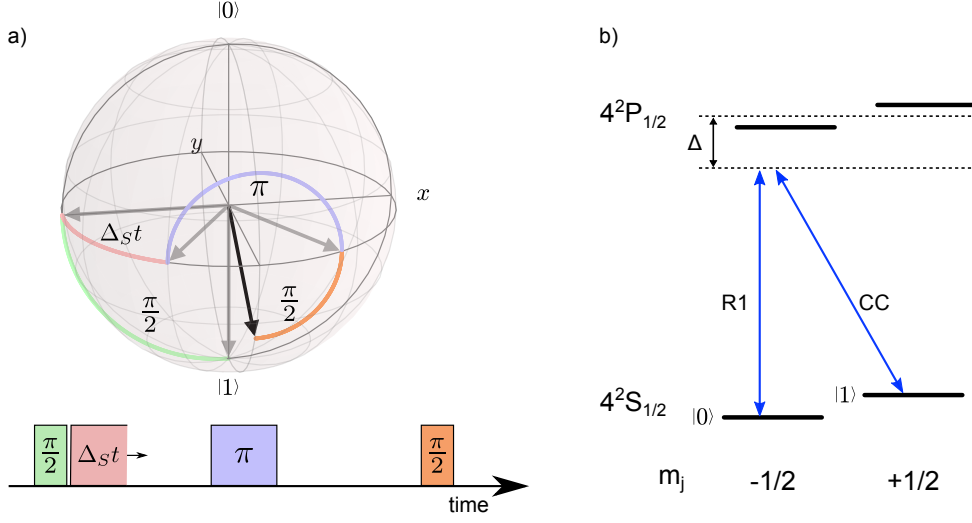


**Figure 3.9.:** a) Pulse sequence of a spin-echo measurement for determining the AC-Stark shift  $\Delta_S$ . The effects of the pulses on the state are depicted on the Bloch sphere. The duration of the AC-Stark shift pulse between the first  $\pi/2$  - pulse and the  $\pi$  pulse is scanned. b) Coherent dynamics between  $|0\rangle$  and  $|1\rangle$  are driven by two off-resonant laser fields, detuned with respect to each other by the total ground state splitting.

transition, see Fig. 3.9 b). After state initialization of the ion to  $|1\rangle$ , the pulse sequence for a spin-echo measurement involves two,  $\pi/2$  - pulses, with one  $\pi$  pulse in the middle. Between the pulses, a constant waiting time  $\tau$  is inserted. The effect of such a pulse on the state is described by the rotation operator  $R_i(\theta)$ , where  $\theta$  is the rotation angle, and  $i$  is the rotation axis on the Bloch sphere [Nie00, Rie05]. During the first waiting time  $\tau$ , the off-resonant laser radiation is switched on for the variable time  $t$ , which gives rise to the AC-Stark shift  $\Delta_S$  during  $t$ . In the total effect of all pulses in the sequence on  $|1\rangle$  reads:

$$R_y(\pi/2)R_y(\pi)R_z(\Delta_S t)R_y(\pi/2)|1\rangle \rightarrow \frac{1}{2} [(1 - e^{i\Delta_S t})|0\rangle - (1 + e^{i\Delta_S t})|1\rangle] \quad (3.21)$$

This sequence of pulses is also depicted in 3.9 a).

Afterwards, a measurement in the  $z$  - basis is performed. The squared probability amplitudes yield the following probability for the ion being projected into the state  $|1\rangle$ ,  $P_{|1\rangle}$ :

$$P_{|1\rangle} = \frac{1}{2} [1 + \cos(\Delta_S t)] \quad (3.22)$$

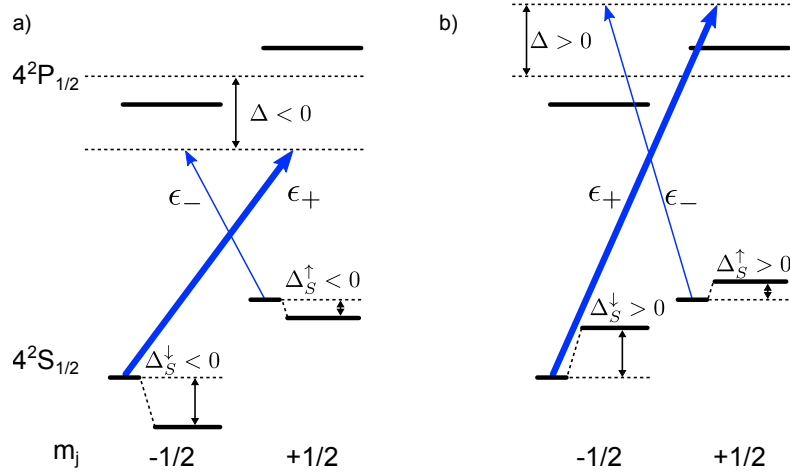


**Figure 3.10.:** Dependence of the the sign of  $\Delta_S = \Delta_S^\downarrow - \Delta_S^\uparrow$  and the sign of the detuning  $\Delta$  for the case  $\epsilon_+ > \epsilon_-$ . In the red-detuned ( $\Delta < 0$ ) case a), the differential AC-Stark shift is negative ( $\Delta_S < 0$ ), whereas in the blue detuned ( $\Delta > 0$ ) case b), this shift is positive ( $\Delta_S > 0$ ). See also Fig. 2.1 in chapter 2.2.1. The AC-Stark shifts of the levels in the  $4^2P_{1/2}$  manifold are not shown, as they are of no further relevance in the following. Note also, that regardless of the AC-Stark shifts the Zeeman sublevels are not degenerate, but split due to a non-zero magnetic field.

Eq. 3.22 is the experimentally accessible function. Fitting that expression to the measured data yields  $\Delta_S$  as a fit parameter.

At this point, it has to be noted, that due to the symmetry of the cosine function, it is not possible to infer the sign of  $\Delta_S$  from fitting Eq. 3.22. However, as can be seen from Fig. 3.10, this information can be deduced from the sign of the detuning  $\Delta$ .

### 3.4.3. Combining $R_+$ , $R_-$ and $\Delta_S$ to obtain Decay Rates and Matrix Elements

Combining now Eq. 3.12 and Eq. 3.20 results in a neat and simple expression for the decay rate  $\gamma_{PS}$ ,

$$\gamma_{PS} = 3\Delta \frac{R_+ - R_-}{\Delta_S^\downarrow - \Delta_S^\uparrow} = 3\Delta \frac{\delta R}{\Delta_S} \quad (3.23)$$

Note, that the Rabi frequency  $\Omega$ , which is notoriously hard to determine experimentally, does not appear in Eq. 3.23. However, the detuning  $\Delta$  does, and still needs to be determined. On first sight, that might seem trivial, using the wavelength meter from chapter 3.2 for measuring the absolute wavelength of the off-resonant laser  $\nu_i$  for each detuning  $i$ . To measure the resonance frequency  $\nu_{ref}$  in the same fashion however can be more problematic, as there is a multitude of effects, which deteriorate the accuracy



of that measurement, and are hard to quantify, e.g. saturation broadening of the line [Bra92], non-Lorentzian shape of the line due to excess micromotion of the ion [Pru14] or effects due to the Zeeman splitting.

In order to circumvent those difficulties to find  $\nu_{res}$ , one can make use of the fact, that the ratio of  $\Delta_S$  and  $\delta R$  is proportional to the detuning, which directly follows from Eq. 3.23:

$$\Delta \propto \frac{\Delta_S}{\delta R} \quad (3.24)$$

Plotting  $\Delta_S/\delta R$  over their different, well known absolute frequencies allows for fitting a linear function to that data. The zero-crossing of that linear function now yields the resonance frequency. This means,  $\Delta_S$  and  $\delta R$ , together with their absolute frequencies  $\nu_i$  suffice to determine the detunings  $\Delta$ , and no additional measurement are needed. The requirement that the data for different detunings  $\Delta$ , evaluated as in Eq. 3.24 needs to fit to a linear function also constitutes an additional countercheck of the data's validity.

Together with the leak factor  $b = 3\gamma_{PD}/\gamma_{PS}$  from Eq. 3.15, Eq. 3.23 also yields the decay rate of the metastable state  $\gamma_{PD}$ . The lifetime of the excited state  $\tau$  can now be deduced via  $\tau = 1/(\gamma_{PS} + \gamma_{PD})$ . Together with the resonance wavelength of the  $S_{1/2} \leftrightarrow P_{1/2}$  and the  $P_{1/2} \leftrightarrow D_{1/2}$  transitions, and using Eq. 2.55 the reduced matrix elements  $\mathcal{D}_i$ ,  $i = \{PS, PD\}$  can be determined as well:

$$\mathcal{D}_i^2 = 2\gamma_i \frac{3\epsilon_0\hbar}{8\pi^2} \lambda_i^3 \quad (3.25)$$

Additionally, it is possible to extract [Saf11]

$$\tilde{\mathcal{D}}_{PS} = \sqrt{2}\mathcal{D}_{PS}, \quad (3.26)$$

where  $\tilde{\mathcal{D}}_{PS}$  pertains to the reduced matrix element of the  $4^2P_{3/2} \leftrightarrow 4^2S_{1/2}$  transition.

All these quantities can be determined, by measuring the differential spin-flip rate  $\delta R$  together with the leak factor  $b$ , the differential AC-Stark shift  $\Delta_S$ , the detuning  $\Delta$  of the off-resonant laser field, as well as the resonance wavelengths of the transitions in question,  $\lambda_{PS}$  and  $\lambda_{PD}$ . The implementation of those measurements will be discussed in detail in the next chapter.

### 3.5. Experimental Implementation

Two similar experimental sequences are performed to determine first the spin-flip rates  $R_{\pm}$  and second the AC-Stark shift  $\Delta_S$  using the setup described in the chapters 3.2 and 3.3. Both those effects are mediated by the same laser field labelled R2. The main focus has been put on keeping the parameters of that laser field constant during many identical iterations of both those experiments. The laser's detuning  $\Delta$  does not need to be measured separately, but can be inferred by evaluating the data taken for  $R_{\pm}$  and  $\Delta_S$  together with the wavelength of the R2 beam, which is constantly logged.

For all measurements described here, a single ion is trapped at a fixed position at segment 5 in the trap [Sch08]. The trapping frequencies are  $\sim 1.4$  MHz in the trap's axial direction, and  $\sim 2.5$  MHz in radial direction. For those values, the DC voltages at trapping segment 5 are  $\sim -7$  V and the RF drive frequency is 35.225 MHz. Micromotion compensation happens by applying  $\sim \pm 100$  mV on the DC electrodes of the trap.

These specifics of trap operation play only a minor role, and are somewhat arbitrary. Most importantly, the configuration needs to be sufficiently stable over time to ensure a prolonged operation without excessive readjustment of control parameters. Also, effects of the somewhat large micromotion of the trap geometry need to be taken into account in the uncertainty evaluation, although their relative contribution is considerably small, as discussed in detail in appendix A.

#### 3.5.1. The Measurement of $R_{\pm}$ and $\Delta_S$

In summary, the experimental sequence for each of both measurements starts with **Doppler cooling** the ion, then a **state initialization** is performed. As the ion is now in a well-defined state, the **interaction with the off-resonant laser field** takes place. At the end, **fluorescence detection** is performed, projecting the ion in either a bright or a dark state. The sequences used to implement these measurements are depicted in 3.11.

#### Doppler Cooling

On the beginning of the sequence, standard Doppler cooling [Hän75, Win78, Ste86, Roo00] on  $S_{1/2} \leftrightarrow P_{1/2}$  transition of the ion is performed. It is driven with  $\approx 50 \mu\text{W}$  of laser light which is  $\approx 50$  MHz red detuned from the resonance. The repumping light close to 866 nm is blue detuned from resonance in order to avoid the occurrence of

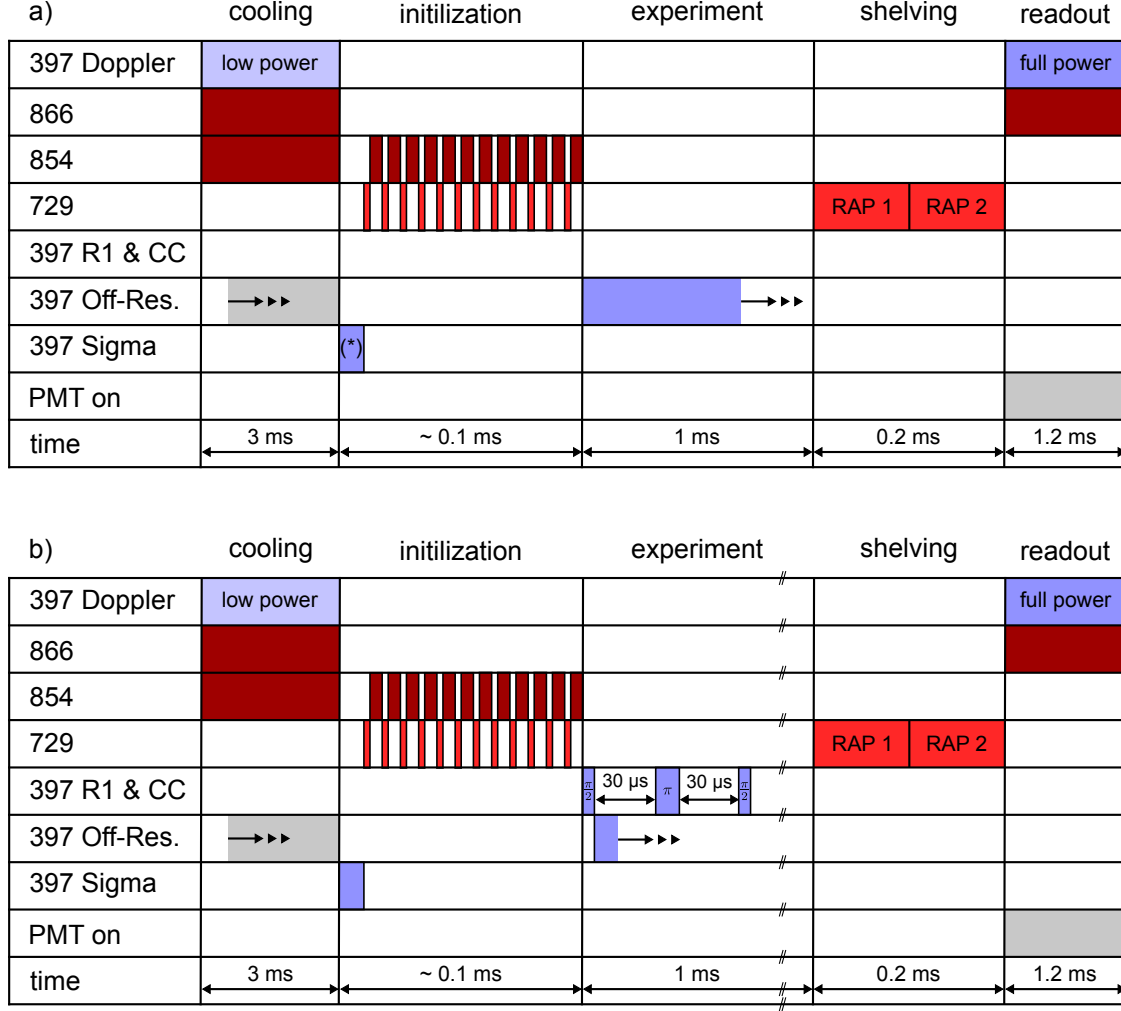


**Figure 3.11.:** Sequences of a) the scattering experiment for the measurement of the spin-flip rates  $R_+$  and  $R_-$  and b) the spin-echo experiment for measuring the AC-Stark Shift  $\Delta_S$ . Note the non-linear time axis. The sequences' total duration is identical and always constant. The scanned parameter in both cases is the pulse length of the off-resonant laser during the actual experiments. During Doppler cooling, the off-resonant laser's AOM is switched on to warm up the device before the experiment, thus minimizing possible temperature-induced beam pointing issues. The EOM (see Fig. 3.4) switches the laser off during that warm-up pulse, and the ion is not illuminated. As the experimental pulse's duration increases, the warm-up pulse's duration decreases such, that the total duration during which the AOM is switched on is kept constant at 3 ms for each count cycle. The pulse for  $\sigma$ -pumping is only used, when initializing the ion to  $|\uparrow\rangle$  (see (\*)). It is left out of the sequence otherwise.

dark resonances [Scu01] in the fluorescence spectrum. It is indeed possible to make use of those dark resonances for cooling purposes [Har12], but their much steeper slope compared to the standard line makes this kind of cooling much more sensitive to minor frequency fluctuations of the lasers involved. The quench laser near 854 nm is also turned on during cooling, as the ASE-background from the diode near 397 nm can spuriously drive off-resonant transitions to the  $P_{3/2}$ -state, and in return population might be trapped in the  $D_{5/2}$ -state otherwise. Although durations in the order of  $\sim 500 \mu\text{s}$  are enough to reliably cool the ion, all lasers are switched on for 3 ms. This time is used for warming up the AOM of the off-resonant laser (see below). All experiments described here can be performed on Doppler cooled ions, no further cooling, e.g. resolved sideband cooling [Win75, Mon95, Esc03] is necessary.

#### Optical Pumping and State Initialization

In order to precisely determine  $R_+$  and  $R_-$ , it is necessary to initialize the ion deterministically in one of the two  $S_{1/2}$  Zeeman levels. After doppler cooling however, both those sublevels are populated. A frequency-resolving optical pumping scheme [Roo06] is used transport all the population in one of those two ground states. Using a  $\pi$ -pulse on the narrow quadrupole transition, population from one of the two  $S_{1/2}$  substates is selectively transferred to the  $D_{5/2}$ -state, which is afterwards quenched with the laser close to 854 nm, and the population decays back to the  $S_{1/2}$  manifold. The specific transitions are selected in such a way, that most of the population ends up the target Zeeman sublevel, see Fig. 3.12. To account for that fraction of the population, which ends up again in the non-target sublevel and for resiliency against process imperfections (e.g. imperfect  $\pi$  pulses on the quadrupole transition), this scheme is repeated twelve times, which routinely transfers a fraction of more than 0.99 to the target sublevel<sup>20</sup>.

#### Off-resonant Interaction: Spin Flip Rates

The next part of the experimental sequence consists of a time window of 1 ms duration, in which the ion is subjected to the off-resonant light. If the spin-flip rate  $R_+$  or  $R_-$  induced by that light is to be measured, the off-resonant light is switched on for a duration  $\tau_R$  in that time window, which causes the initial state to depolarize, as described in Eqs. 3.18. Repeating that experiment for different values  $\tau$  allows for fitting Eqs. 3.18 to the data, and therefore extracting the parameters  $R_+$  and  $R_-$ . The choice of the values  $\tau_R$  is nonlinear with time, as most of the interesting dynamics are

---

<sup>20</sup>This number is the combined success rate for both the initialization and the readout process, as they cannot be straightforwardly separated.

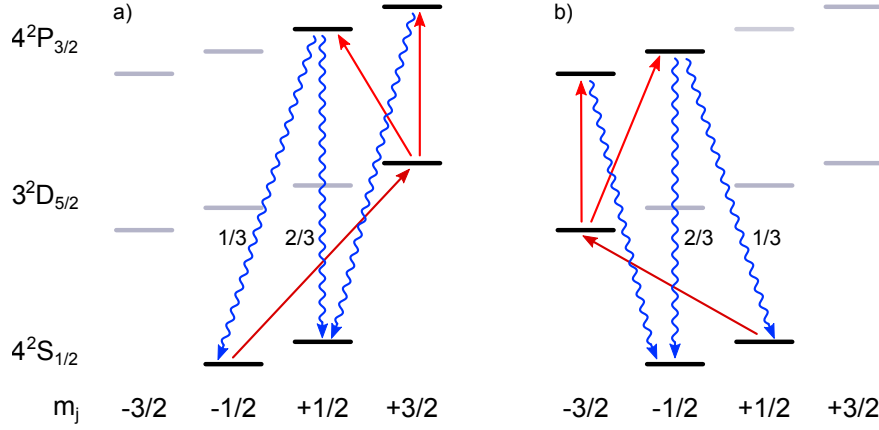


**Figure 3.12.:** Level scheme and transitions participating in the pumping process using the quadrupole transition near 729 nm. Pumping to the  $|S_{1/2}, m_S = +1/2\rangle$  ( $|S_{1/2}, m_S = -1/2\rangle$ ) is shown in a) (b). The process is not working perfectly even in the ideal case, where one pulse fails to pump the population to the target state with a probability of  $\approx 1/6$ . The numbers shown next to the  $P_{3/2} \leftrightarrow S_{1/2}$  - transitions are relative transition probabilities, i.e. normalized squared Clebsch-Gordan coefficients. The pumping process is repeated several times until the population fraction in the target state is above the required threshold.

happening for small  $\tau_R$ , which makes a high sampling rate preferable there. For large  $\tau_R$  however, a lower sampling rate is sufficient, as the dynamics of 3.18 almost die down there, as depicted in Fig 3.8.

### Off-resonant Interaction: AC-Stark Shift

If instead of the spin-flip rates  $R_+$  and  $R_-$  the AC-Stark shift  $\Delta_S$  is to be determined, a spin-echo measurement [Hah50, Car54] is performed in the 1 ms window. To that end, coherent dynamics are driven between the two Zeeman levels of the  $|S_{1/2}\rangle$  ground state,  $|\uparrow\rangle$  and  $|\downarrow\rangle$ , using a two-photon Raman transition. A spin-echo measurement according to the description in chapter 3.4.2 is implemented as follows: One  $\pi/2$  pulse, which produces the superposition state  $|\uparrow\rangle + |\downarrow\rangle$  from the initial state. This state is now freely evolving during the time  $\tau_{e1} = 30 \mu\text{s}$ . After that, a  $\pi$  pulse inverts the state's phase, and the state is again allowed to freely evolve for another time  $\tau_{e2} = \tau_{e1}$ . A final  $\pi/2$  pulse concludes the measurement. During  $\tau_{e1}$ , the off-resonant light is switched on for a variable time  $\tau_S$ , which induces an AC-Stark shift on the respective level during  $\tau_S$ , as shown in Eq. 3.20. This is effectively imposing a variable phase shift onto the state  $|\uparrow\rangle + |\downarrow\rangle$ , which manifests itself through an oscillatory signal, see Eq. 3.22.

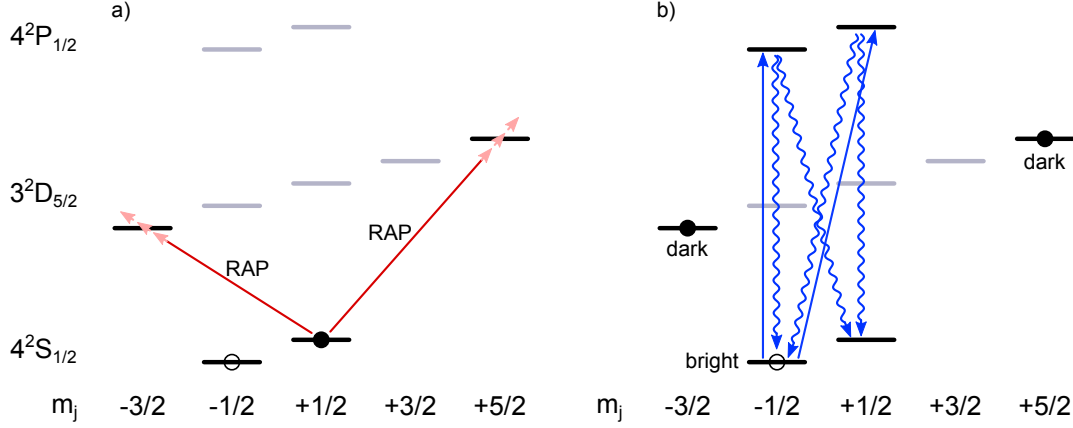


**Figure 3.13.:** a) Electron shelving performed by two RAPs, first on the  $|S_{1/2}, m_j = +1/2\rangle - |D_{5/2}, m_j = -3/2\rangle$  transition and second on the  $|S_{1/2}, m_j = +1/2\rangle - |D_{5/2}, m_j = +5/2\rangle$  transition. After this process, the  $|S_{1/2}, m_j = +1/2\rangle$  is depopulated to a high degree. b) Now, standard fluorescence detection takes place. Population in the  $|S_{1/2}, m_j = -1/2\rangle$  makes the ion fluoresce upon radiation with a resonant laser field (repumping processes not shown), while population in the  $|D_{5/2}\rangle$  manifold does not.

### Electron Shelving and State Detection

At the end of the sequence the ion's electronic state needs to be projected to measurement eigenbasis and detected. The first step here is to perform *electron shelving* [Nag86], by which the population of the  $|\uparrow\rangle$  - state is transferred ("shelved") to the  $|D_{5/2}\rangle$  state. Two independent transitions are driven by the quadrupole laser near 729 nm in order to deplete the state as well as possible, as shown in Fig. 3.13. To increase the resiliency of those processes, the the transitions in question are not driven by simple  $\pi$  - pulses, but by rapid adiabatic passages (RAPs) [Vit01], where a light field is smoothly turned on and off again, while its frequency is chirped over the transition's resonance frequency. Care has to be taken when adjusting the power of the RAP pulses, as more power will always improve the transfer probability of the  $|\uparrow\rangle$  - state to the  $D_{5/2}$  - state, but it will also at some point drive also an unwanted  $|\downarrow\rangle \leftrightarrow |D_{5/2}\rangle$  transition due to power broadening effects. This means the total power needs to be low enough, before this *cross talk shelving* becomes relevant.

As now the population in  $|\uparrow\rangle$  has been mapped to the  $D_{5/2}$  - state, standard fluorescence detection [SK03] can be performed, where a bright event corresponds to the ion being in  $|\downarrow\rangle$ , whereas a dark ion maps to  $|\uparrow\rangle$ . The fluorescence detection in the experimental sequence is performed using a PMT. A triggered counter module counts the PMT's detection events during a time window of 1.2 ms.

### 3.5.2. The Measurement of the Detuning $\Delta$

As shown in chapter 3.4.3, no distinct measurement is necessary for determining the detuning  $\Delta$ , only the absolute frequencies of the scattering light need to be determined. This is achieved by constantly logging that frequencies with the wavelength meter during all measurements. To monitor the drifts of the meter itself, the frequency of the quadrupole laser close to 729 nm is also logged. As this laser is actively stabilized to a high finesse cavity, its linewidth and long-term frequency drifts are orders of magnitude smaller than what the wavemeter is able to resolve. It thus can serve as a frequency reference.

## 3.6. Data Evaluation and Results

In this section it is discussed, how the measurement data has been acquired and processed further. The fitting of the data to the model described in chapter 3.4 is explained, and the results are extracted

### 3.6.1. Data Acquisition

The measurement sequence of the spin flip rates is described in chapter 3.5.1. In the following, the layout of the data acquisition is described, and some nomenclature for use throughout the remainder of this thesis is defined.

- Executing the the sequence depicted in Fig 3.11 once performs on single spin-flip rate experiment. At the end of the sequence, during detection, the ion is projected either to  $|\uparrow\rangle$  or  $|\downarrow\rangle$ . Such a single instance of an experiment will be called a **count cycle**.
- After one specific experiment is executed, before the detection, the state of the ion reads  $|\psi\rangle = \alpha |\uparrow\rangle + \beta |\downarrow\rangle$ . To accumulate information about  $\alpha^2$  und  $\beta^2$  to reduce their uncertainty, many identical count cycles are executed. This set of count cycles, will be called a **data point**. For the spin-flip rate experiments, one data point consists of 25 count cycles, for the AC-Stark shift measurements, it consists of 50 count cycles.
- To be able to fit a suitable model to the data, multiple data points are recorded, with a chosen parameter being scanned. The scanned parameter in the case of both the spin-flip rate measurements and the AC-Stark shift measurements is the

duration the ion is exposed to the off-resonant light. The scanned parameter is quantized in suitable steps to sample the features of the model adequately. A set of data points, where each sample step of the scanned parameter is populated by one data point will be termed **iteration**. One iteration of spin-flip measurements contains 30 data points, one iteration of AC-Stark shift measurements consist of 250 data points.

- To increase the statistical significance of the acquired data, several iterations of a measurement are performed. One set of iterations will be called a **data set**. One spin-flip measurement data set usually consists of 100 iterations<sup>21</sup>, one AC-Stark shift data set of 3 iterations. Those data sets are now used to fit model functions to.

Another parameter, which was changed after several data sets of spin-flip and AC-Stark measurements is the detuning  $\Delta$ , which has been set to four different values during the measurement. For the spin-flip measurements also the spin initialization was changed after each count cycle, which effectively means, that always a pair of spin-flip measurement data sets has been recorded in an interleaved fashion. In total, 65 pairs of data sets of spin-flip measurements and 75 data sets of AC-Stark shift measurements have been acquired.

#### 3.6.2. Determining the Spin-flip Rates $R_+$ and $R_-$

The data sets acquired in the spin-flip rates measurements are used for fitting a model function, and thereby extracting the the spin-flip rates  $R_+$  and  $R_-$  and the leak factor  $b$  from the data. The idealized model functions 3.18 however are not sufficient for that purpose for two reasons:

- The **initialization** of the ionic state is always non-perfect. This means each data set needs to be fitted to a model function taking into account the intended initial ionic ground state polarization as well as a small fraction of the unintended polarization. This means, the data for both initial polarizations need to be fitted to not only one part of Eq. 3.18, but to both. Two free parameters are added to the model,  $a_\uparrow$  and  $a_\downarrow$ , which act as weights for the two parts of Eq. 3.18. In the case of perfect initialization, the ideal values of those two parameters would read  $a_\uparrow = a_\downarrow = 1$ .

---

<sup>21</sup>Some data sets consist of less iterations, because the operation of the experimental setup was interrupted, e.g. due to a laser falling out of lock.



- The **readout** of the ionic state is always non-perfect as well. This translates in a dark ion being wrongly detected as being bright, and vice versa. As this effect is also not contained in the model from Eq. 3.18, another set of two parameters is introduced to account for this error.  $\bar{r}_\downarrow$  is the probability of the ion's initial state being  $|\downarrow\rangle$ , but *wrongly* being detected as  $|\uparrow\rangle$ , i.e. the ion *wrongly* being detected as being dark.  $r_\uparrow$  at is the probability of the ion's initial state being  $|\uparrow\rangle$ , and being *correctly* detected as being as  $|\uparrow\rangle$ , i.e. the ion *correctly* being detected as being dark. In the case of perfect readout, the ideal values of those two parameters would read  $\bar{r}_\downarrow = 0$  and  $r_\uparrow = 1$ .

The refined model functions  $f_\uparrow(t)$ ,  $f_\downarrow(t)$ , taking the errors in initialization and readout into account read now

$$\begin{aligned} f_\uparrow(t) &= \bar{r}_\downarrow + (r_\uparrow - \bar{r}_\downarrow) \left[ a_\uparrow p_\uparrow^{(\uparrow)}(t) + (1 - a_\uparrow) p_\uparrow^{(\downarrow)}(t) \right] \\ f_\downarrow(t) &= \bar{r}_\downarrow + (r_\uparrow - \bar{r}_\downarrow) \left[ a_\downarrow p_\uparrow^{(\downarrow)}(t) + (1 - a_\downarrow) p_\uparrow^{(\uparrow)}(t) \right]. \end{aligned} \quad (3.27)$$

These functions are used fitting the spin-flip data sets,  $p_\uparrow^{(\uparrow)}(t)$  and  $p_\uparrow^{(\downarrow)}(t)$  are the model functions from Eq. 3.18, see Fig. 3.14. Both those functions are jointly fitted to one pair of spin-flip data sets to obtain one set of fitting parameters ( $R_+$ ,  $R_-$ ,  $b$ ,  $a_\uparrow$ ,  $a_\downarrow$ ,  $r_\uparrow$ ,  $\bar{r}_\downarrow$ ).

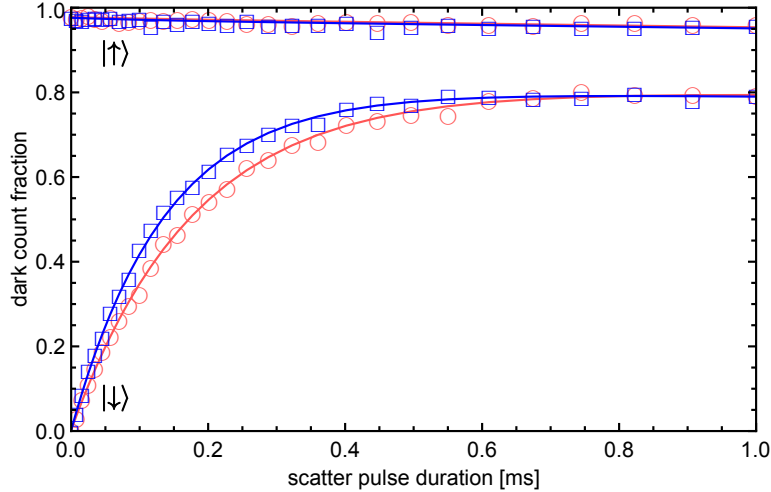


**Figure 3.14.:** Two pairs of spin-flip rate data sets (red and blue). Dark event fraction are plotted versus time of exposure to the off-resonant laser pulse for initializations in  $|\uparrow\rangle$  and  $|\downarrow\rangle$ . Data points indicated by blue squares (red circles) are measured with the laser detuned by -12.03 GHz (-13.94 GHz) from resonance. Solid lines show the fits to the model from Eq. 3.27. Figure taken from [Het15].

Note that the described way of dealing with initialization and readout errors is merely a phenomenological description which yields no detailed insight of the physical processes behind those errors. A more detailed approach can be found in [Pos10b], where e.g. the errors occurring in the photon detection process are separated from those occurring during electron shelving. Such a more elaborate model has not been used in this treatment however, as it would merely lead to more free fitting parameters, which have no further use.

#### 3.6.3. Determining the AC-Stark Shift $\Delta_S$

The model function for fitting the data sets acquired in the AC-Stark shift measurements needs some refinement as well in order to perform proper fitting to the data.

- **Decoherence** effects, like fluctuating magnetic fields, slowly reduce the contrast of a spin-echo measurement's signal. To account for those effects, an exponential decay with the decay time  $\tau$  is incorporated in the refined model.
- Like in the refined model for the spin-flip dynamics, **readout** errors are taken into account by adding the parameters  $\bar{r}_\downarrow$  and  $r_\uparrow$  to the model.

This changes Eq. 3.20 to the refined model function

$$f_S = \frac{1}{2} [r_\uparrow + \bar{r}_\downarrow + (r_\uparrow - \bar{r}_\downarrow) \exp(-t/\tau) \cos(\Delta_S t)]. \quad (3.28)$$

It is used to fit each AC-Stark shift data set, see Fig. 3.15 and yields the parameters  $(\Delta_S, r_\uparrow, \bar{r}_\downarrow, \tau)$ .

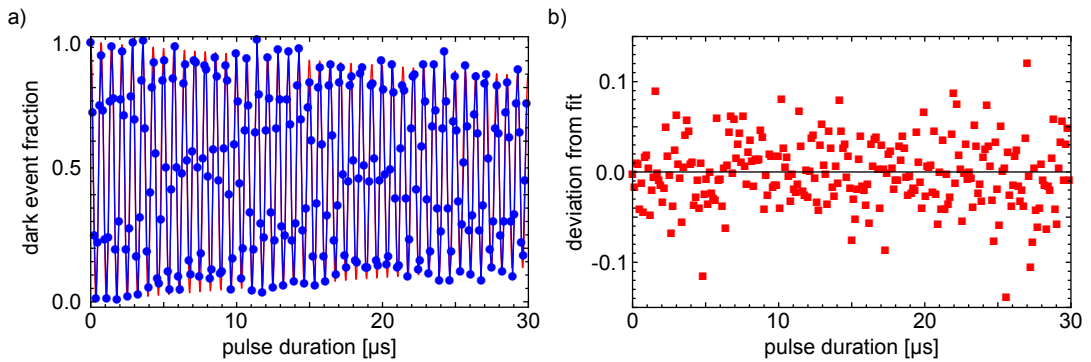


**Figure 3.15.:** a) Dark event fraction versus pulse duration for a spin-echo experiment. The blue line connects the data points, the red line is the resulting fit to the model from Eq. 3.28. The oscillation frequency directly corresponds to the differential AC-Stark shift  $\Delta_S$ . b) Deviation of data shown in a) from the model. Figure taken from [Het15].

### 3.6.4. Determining the Frequencies $\nu_i$ of the Off-resonant Laser

The four different detunings  $\Delta$  used for the measurements have been chosen by adjusting the absolute frequency of the off-resonant laser to four different absolute frequencies respectively. Their values were determined by constantly logging the laser's frequency  $\nu$ , and afterwards taking the mean. The resonance frequency  $\nu_{res}$ , and therefore the detunings  $\Delta$  have been determined by plotting  $\Delta_S/\delta R$  over  $\nu$ , performing a linear fit, and determining its zero-crossing, see Fig. 3.16.

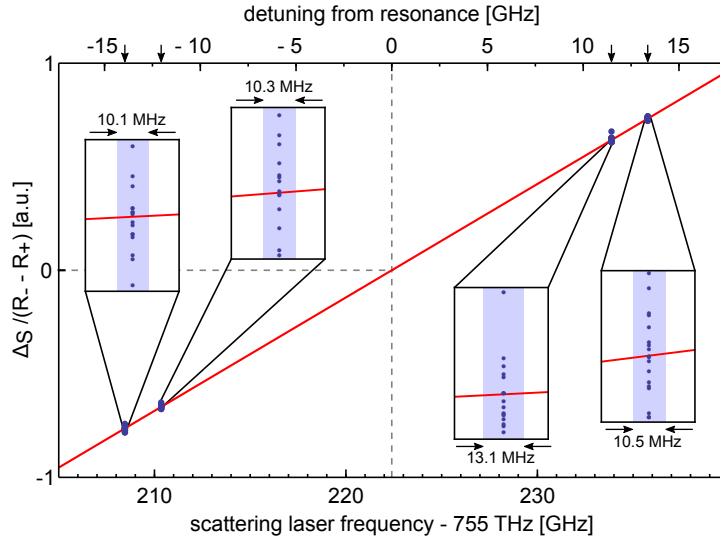


**Figure 3.16.:** Determination of the four detunings chosen for the measurements. For each of the 65 acquired spin-flip data set pairs, we plot the quantity  $\Delta_S/\delta R \propto \Delta$  versus the optical frequency as measured by a wavelength meter. The zero crossing of a linear fit, depicted by the solid red line, reveals the resonance frequency. The insets show details of the spin-flip data sets measured at the different detunings with the abscissa magnified 166 times. The shaded backgrounds indicate their uncertainties along the frequency axis. The arrows on the top frequency scale indicate the values of the four different detunings at -13.94, -12.03, 11.52, and 13.42 GHz. Figure taken from [Het15].

### 3.6.5. Results, Uncertainties and Shifts

$N=65$  pairs of spin-flip rate data sets have been taken, distributed over the four different detunings, yielding 65 values of  $\delta R = R_+ - R_-$  and  $b$  from fitting. Before and after each spin-flip rate data set, one AC-Stark Shift data set has been recorded, yielding a values for  $\Delta_S$  each. The mean of those two values is taken to be the AC-Stark shift belonging to the respective value of  $\delta R$ . This allows now for calculating 65 values for  $\gamma_{PS}$  according to Eq. 3.23. Their mean reads

### 3. Measurement of Dipole Matrix Elements

---

$$\gamma'_{PS} = \frac{1}{N} \sum_{i=1}^N \Delta_i \frac{\delta R_i}{\Delta_{S,i}} = 2\pi \times 21.48 \text{ MHz}. \quad (3.29)$$

As this is an experimentally determined value, it is subject to uncertainties as well as systematic shifts. Those are summarized in Table 3.1 and their underlying calculations can be found in appendix A.

Looking at the numbers, it is remarkable, that the largest contributions to both the uncertainty and the shift of  $\gamma_{PS}$  come from *residual  $\epsilon_0$  polarized light* in the off-resonant laser. In order for Eq. 3.15 to hold, it is necessary to assume that the  $\epsilon_0$  component of that light is zero. Imperfect alignment of the beam with respect to the magnetic field and limitations concerning the control of the beam's polarization at the position of the ion, e.g. by strain-induced birefringence in the window of the vacuum vessel give rise to this unwanted polarization component. The next contributors are the *uncertainty of the resonance frequency* and the *statistical uncertainty of  $\delta R$* , arising from the uncertainties of fitting the respective models to the data. *Residual near-resonant light* weakly driving the  $S_{1/2}$  -  $P_{1/2}$  transition, mostly from the imperfectly switched off Doppler laser contributes as well, as does the limited *wavemeter precision*, which is determined by constantly logging all wavelengths and taking the stable, narrow-linewidth laser source close to 729 nm as a reference.  *$D_{3/2}$  depletion* is caused by two processes, first the finite lifetime of the  $D_{5/2}$  state, and second residual repumper light close to 866 nm. The *uncertainty of  $\Delta_S$*  due to drifts during the measurements plays only a minor role, as does the *influence of micromotion*. The *influence of the  $P_{3/2}$  state* and *residual line broadening effects* give both rise to a certain shift, but their contribution to the total uncertainty is close to being negligible.

Taking all those shifts and uncertainties into account, the corrected decay rate reads

$$\gamma_{PS} = 2\pi \times 21.57(8) \text{ MHz}. \quad (3.30)$$

In the following, additional quantities are derived using  $\gamma_{PS}$ . The 65 obtained values for  $b$  allow for the calculation of the decay rate of the  $4^2P_{1/2} \leftrightarrow 3^2D_{3/2}$  transition,

$$\gamma_{PD} = \gamma_{PS} \frac{b}{3} = \gamma_{PS} \frac{1}{3N} \sum_{i=1}^N b_i = 2\pi \times 1.482(8) \text{ MHz}, \quad (3.31)$$

Effect	Shift $\times 10^{-3}$	Uncertainty $\times 10^{-3}$
Residual $\epsilon_0$ polarized light	3.3	2.9
Uncertainty of resonance frequency	-	1.6
Statistical uncertainty of $\delta R$	-	1.5
Residual near-resonant light	-0.4	0.5
Wavemeter precision	-	0.4
$D_{3/2}$ depletion	0.3	0.2
Uncertainty of $\Delta_S$	-	0.2
Influence of micro motion	-	0.1
Influence of $P_{3/2}$ state	0.3	$< 0.1$
Residual line-broadening effects	0.1	$< 0.1$
Total	+3.6	3.7

**Table 3.1.:** List of relative corrections and measurement uncertainties for  $\gamma_{PS}$ . The specified values result from averaging over the 65 sets of measurement data. They are added in quadrature to obtain the resulting final uncertainty.

and the radiative lifetime of the  $4^2P_{1/2}$  state

$$\tau = \frac{1}{\gamma_{PS}[1 + b/3]} = 6.904(26) \text{ ns.} \quad (3.32)$$

The branching fraction  $\mathcal{B}$  of the  $4^2P_{1/2} \leftrightarrow 4^2S_{1/2}$  transition and the  $4^2P_{1/2} \leftrightarrow 3^2D_{3/2}$  transition reads then

$$\mathcal{B} = \frac{\gamma_{PS}}{\gamma_{PS} + \gamma_{PD}} = \frac{1}{1 + b/3} = 0.93572(25) \quad (3.33)$$

The reduced dipole matrix element of the  $4^2P_{1/2} \leftrightarrow 4^2S_{1/2}$  transition,  $\mathcal{D}_{PS}$  can be calculated using Eq. 3.25, where the necessary transition wavelength  $\lambda_{PS}$  is used as determined by the method explained by Fig. 3.16. In atomic units [Bra92], it reads

$$\mathcal{D}_{PS} = 2.8928(43) \text{ } ea_0. \quad (3.34)$$

The reduced dipole matrix element of the  $4^2P_{1/2} \leftrightarrow 3^2D_{3/2}$  transition  $\mathcal{D}_{PD}$  can be determined likewise. The transition's resonance wavelength has been directly measured by the wavemeter in this case. The value reads

$$\mathcal{D}_{PD} = 2.445(5) \text{ } ea_0. \quad (3.35)$$

### 3. Measurement of Dipole Matrix Elements

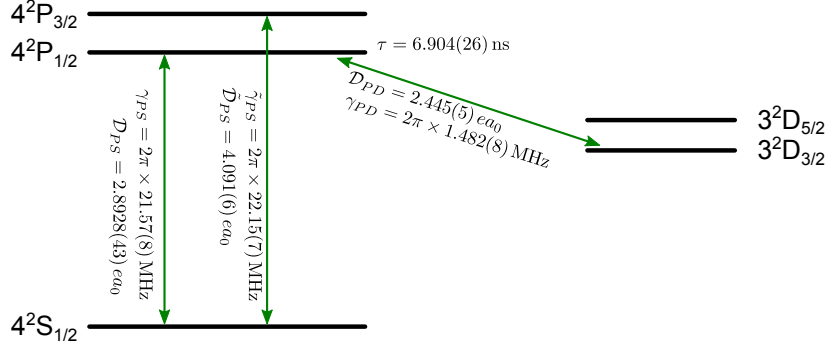


**Figure 3.17.:** Overview of the results of this work. The values of reduced dipole matrix elements and decay rates are drawn next to their transitions, the lifetime of the  $4^2P_{1/2}$  state is indicated as well.

Furthermore, it is possible to calculate the reduced dipole matrix element of the  $4^2P_{3/2} \leftrightarrow 4^2S_{1/2}$  transition  $\sqrt{2}\mathcal{D}_{PS} = \tilde{\mathcal{D}}_{PS}$  [Saf11] together with the respective decay rate  $\tilde{\gamma}_{PS}$ . The transition frequency however needed to be taken from the literature in this case [Bas78], as it was not measured in the experiments described in this thesis.  $\tilde{\mathcal{D}}_{PS}$  and  $\tilde{\gamma}_{PS}$  read

$$\tilde{\mathcal{D}}_{PS} = 4.091(6) ea_0 \quad \tilde{\gamma}_{PS} = 2\pi \times 22.15(7) \text{ MHz.} \quad (3.36)$$

An overview of those results is given in Fig. 3.17, a comparison with literature values can be found in Table 3.2.

Quantity	this work [Het15]	other exp.	theory [Saf11]
$\tau/\text{ns}$	6.904(26)	7.098(20) [Jin93]	6.875(62)
$\gamma_{PS}/\text{MHz}$	$2\pi \times 21.57(8)$	-	$2\pi \times 21.64(19)$
$\gamma_{PD}/\text{MHz}$	$2\pi \times 1.482(8)$	-	$2\pi \times 1.504(16)$
$\tilde{\gamma}_{PS}/\text{MHz}$	$2\pi \times 22.15(7)$	-	$2\pi \times 22.23(20)$
$\mathcal{B}$	0.93572(25)	0.93565(7) [Ram13]	0.93500(90)
$\mathcal{D}_{PS}/ea_0$	2.8928(43)	-	2.898(13)
$\mathcal{D}_{PD}/ea_0$	2.445(5)	-	2.464(13)
$\tilde{\mathcal{D}}_{PS}/ea_0$	4.091(6)	-	4.099(18)

**Table 3.2.:** Comparison of the values determined in this work with theoretical predictions and other experimental results (where applicable). The value for  $\tau$  given in this work starkly deviates from the one given in [Jin93]. All other values are within the uncertainties of the theoretical predictions, except for  $\gamma_{PD}$  and  $\mathcal{D}_{PD}$ , which are more than one, but less than two standard deviations smaller the calculated ones.

### 3.7. Discussion

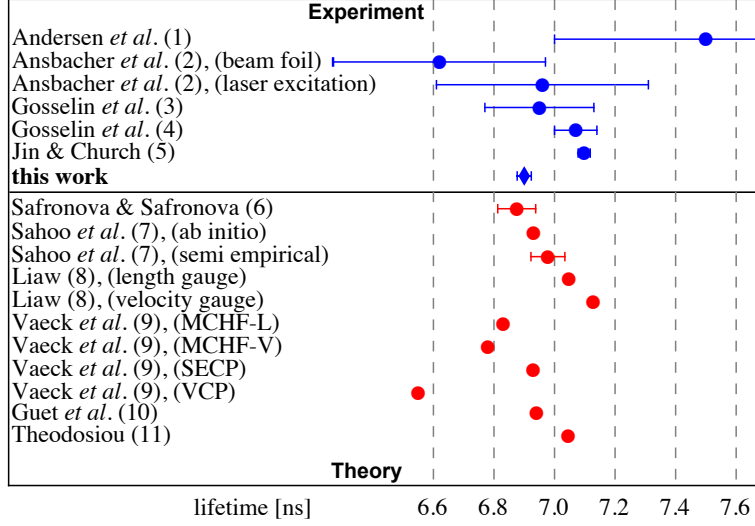


**Figure 3.18.:** Comparison of theoretical calculations and experimental results of the  $4^2P_{1/2}$  state's lifetime  $\tau$ . Note the the result from this work is compatible to the most recent theoretical prediction, whereas it considerably deviates from the experimental result by (5): [Jin93]. (Other references: (1): [And70]; (2): [Ans85]; (3): [Gos88b]; (4): [Gos88a]; (6): [Saf11]; (7): [Sah09]; (8): [Lia95]; (9): [Vae92]; (10): [Gue91]; (11): [The89];) Figure taken from [Het15].

When comparing this work's value for  $\tau$  with those from the literature (see Fig. 3.18), most prominently it shows a strong contradiction to the up to now most recent experimental value from [Jin93]. It deviates from this work's value by more than 11 standard deviations. On the other hand, the most recent theoretical prediction from [Saf11] is in agreement with the value reported in this work. The experimental uncertainty, which might be even further reduced by the measures described above, starts to challenge the uncertainties given by the current methods for atomic physics calculations.

The branching ratio  $\gamma_{PS}/(\gamma_{PS} + \gamma_{PD})$  has been measured with another method [Ram13] to be 0.93565(7), which is in agreement with the value from this work. The theoretical prediction from [Saf11] of 0.9350(9) is also compatible with this work's value.

To the author's knowledge, no prior experimental values for the decay rates  $\gamma_{PS}$ ,  $\gamma_{PD}$  and  $\tilde{\gamma}_{PS}$  or the reduced dipole matrix elements  $\mathcal{D}_{PS}$ ,  $\mathcal{D}_{PD}$  and  $\tilde{\mathcal{D}}_{PS}$  exist, which is why they can be only compared to theoretical predictions. Those values, which can be found in [Saf11], are compatible with this work's result as well.

### 3. *Measurement of Dipole Matrix Elements*

---



## 4. A Segmented Ion Trap for CQED Experiments

### 4.1. Design and Fabrication

The design requirements for an ion trapping device with the main purpose of performing cavity QED experiments in the strong coupling regime are quite specific, and deviate considerably from those for traditional designs intended for other experiments. However, such a system opens up promising possibilities also for applications, like the implementation of a quantum repeater. Strategies how such a device can be implemented using trapped ions and protocols for entanglement distribution are discussed in [Pfi16]. In the following, a detailed discussion of the design and implementation of an ion trap suitable for that purpose is given, from fundamental concepts to fabrication and manufacturing considerations.

#### 4.1.1. Conceptual Guidelines

The necessity of incorporating a high finesse cavity into a ion trap setup intended for CQED experiments without sacrificing the core features of a segmented design poses the most important challenge when designing an experimental setup for that purpose. Strong light-ion coupling should be realized in such a setup, while keeping the possibilities of transporting and splitting ion crystals and of implementing deterministic high-fidelity single- and two-qubit gates.

Mirrors with high reflectivity and low losses in the optical regime always consist of dielectric material, which can be subject to electrostatic charging for various reasons. If in the close vicinity of the ion, the charges on those dielectric mirrors act on the trapping potential in a widely uncontrollable manner. One strategy to alleviate that problem is a placement of those mirrors far away from the ion, as in the experiments described e.g. in [Gut01,Mun02,Her09,Stu12]. For reaching the strong coupling regime, it is however desirable to decrease the cavity's mode volume as far as possible, which directly contradicts a mirror placement far away from the ion.

Recent work established a novel approach for realizing optical cavities of high finesse, where the end facets of two optical fibers are used as cavity mirrors [Ste06, Col07, Hun10]. Compared to cavities made from standard mirror substrates, the physical dimensions of such a fiber cavity are much smaller. Also, activities for development of miniaturized ion trap structures have been constantly increasing for quite some time now. The purposes of those newly developed traps are various, but two major motivations are the ability to obtain higher trap frequencies using lower electrode voltages and the ability to construct segmented ion traps, allowing for controlled transport of ions, as well as separating and merging of ion crystals.

As the physical dimensions of fibercavities and segmented microtraps are on the same scale, this opens the possibility for integrating those two technologies.

The design from [Sch09], see Fig.4.1 a) serves as starting point for the new trap. It features 31 individually addressable trap segments, which allow for transporting ions along the trap's axis. The whole segmented structure consists of two distinct trap regions, a large region with a vertical electrode distance of  $500\text{ }\mu\text{m}$ , and a segment width of  $250\text{ }\mu\text{m}$ , and a small region where the vertical electrode distance is only  $250\text{ }\mu\text{m}$ , and the segment width amounts to  $100\text{ }\mu\text{m}$ . Both are connected with a tapered transitional region. This electrode structure is theoretically understood very well and trap designs featuring that structure have been studied experimentally by many groups [Sch08, Har12, Kau12].

This electrode structure is very well suited for incorporating a fibercavity for various reasons:

- The radial electrode-electrode distance in the small region ( $250\mu\text{m}$ ) roughly matches the mirror distance of typical fiber cavities. This allows a design, where the dielectric fibers of the cavity can be at least partly shielded by the electrodes of the trap structure, if aligned in the trap's radial direction, see Fig. 4.1 b).
- On the other hand, the radial electrode-electrode distance in the large region ( $500\text{ }\mu\text{m}$ ) allows for easy ion loading and imaging, both of which take more effort to realize in the small region.
- The possible distance between the ion loading position and the fibercavity's location amounts to several millimeters. Together with the possibility for fast and cold transport [Wal12, Bow12] of ions between those locations, this allows for a local separation of different operations on the ion: Trapping, cooling and detection, which in the case of  $^{40}\text{Ca}^+$  incorporate the use of laser radiation in the blue and the UV spectrum, can be performed in the trap's large region, and only the interaction with the cavity field takes place at the remote cavity location. The crucial

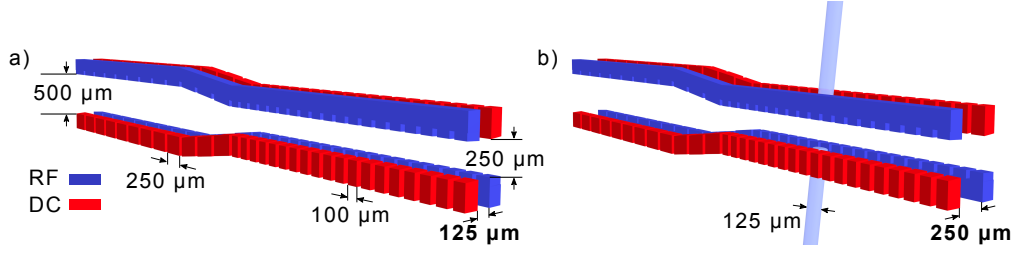


**Figure 4.1.:** a): Electrode structure of the trap from [Sch09]. The linear, segmented microtrap features two distinct regions, and a total of 31 segments. The vertical electrode distance is  $500\ \mu\text{m}$  in the large region, and  $250\ \mu\text{m}$  in the small region. Both are connected with a transitional taper b): Extension of the trap structure a) with an accommodated fiber cavity. The distance between toplayer and bottomlayer has been increased from  $125\ \mu\text{m}$  to  $250\ \mu\text{m}$  in order to provide space for the two fibers. Their distance is  $300\ \mu\text{m}$ , effectively shielding them behind the trap electrodes.

advantage of that experimental strategy is that it largely avoids the exposure of the dielectric fibers to unnecessary direct or scattered laser radiation. This kind of radiation exposure, especially for light in the UV or blue visible spectrum has been shown to be a major source of electrostatic charging of dielectric materials in ion trapping experiments [Har10].

One major design challenge however needs to be solved, when designing a trap assembly with the electrode structure from [Sch09], which can accommodate a fiber cavity. The connections of all electrodes in this design are directly routed outwards to all borders of the trap substrate, where they form larger pads used for wirebonding. Those wirebond connections make the insertion of a fiber cavity structure into the trap assembly as outlined in Fig. 4.1 impossible. The routing of the electrode connections to the outside needs to be altered in such a way, that one part of the outside border of the trap assembly is not blocked by wirebonds, but left free for the fiber cavity to be inserted. For optimal mechanical stability, the mounting point of the fibers needs to be as close to the trap axis as possible, and the amount of trap substrate material around the electrodes of the fiber cavity position in the trap needs to be minimized.

#### 4.1.2. Trap Design

Following the general guidelines described in the previous section a new segmented Paul trap for accommodating a fiber cavity has been constructed. The design is depicted in Fig. 4.2. It consists of three distinct layers, two of which are used to realize the electrodes, and a middle one which only acts as a spacer. The bond pads are located such that the insertion of a fiber cavity is possible.

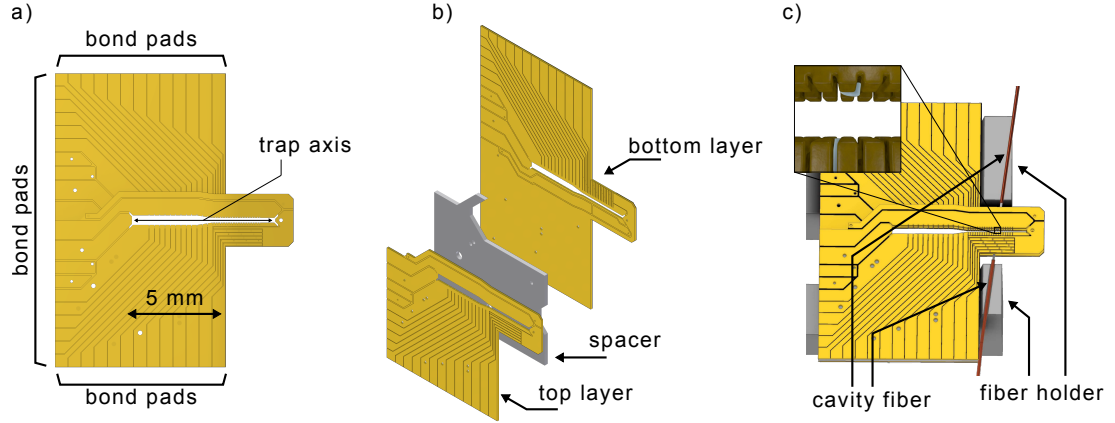


**Figure 4.2.:** a): Front view, on the top, the bottom and the left border are the pads used for wirebond connections, the right side of the trap is unobstructed for insertion of the fiber cavity. b): Exploded view of the trap assembly: Top layer, spacer, and bottom layer are shown separately. Note the absence of spacer material, at the position where the fiber cavity will be situated. c) Trap together with fiber cavity assembly, which is constructed independently from the the trap, and can be inserted and removed in a reversible manner.

### Bond Pads and Conducting Paths

All bond pads have a minimum width of  $660 \mu\text{m}$ , the reason for this being the pitch capacitance arrays the bonds are connected to, see chapter 4.1.4. With one bond connection needing about  $100 \mu\text{m}$  in width, this provides plenty of space for several bonds. Starting from the bond pads, conducting paths run to the segments to be connected. Their width is never smaller than  $100 \mu\text{m}$  to keep the resistance of the connections low. The minimum distance of two conducting paths amounts to  $30 \mu\text{m}$ , for all connections, which carry DC voltage up to  $\pm 10 \text{ V}$ , and  $80 \mu\text{m}$  for connections, which carry higher voltages to prevent arcing.

### Vertical Interconnect Accesses and Coupled Electrodes

The connection of the trap electrodes in the small region, where the fiber cavity will be located is depicted in Fig. 4.3. As shown, an individual direct routing of each DC electrode connection to the trap assembly border is not feasible, so those electrodes are organized in four sets of five electrodes each, which are electrically interconnected. This is realized by a matrix of vertical access interconnects (VIAs), and it allows the addressing of all 40 electrodes of the 20 DC segments, by only using 10 conducting paths to the outside.

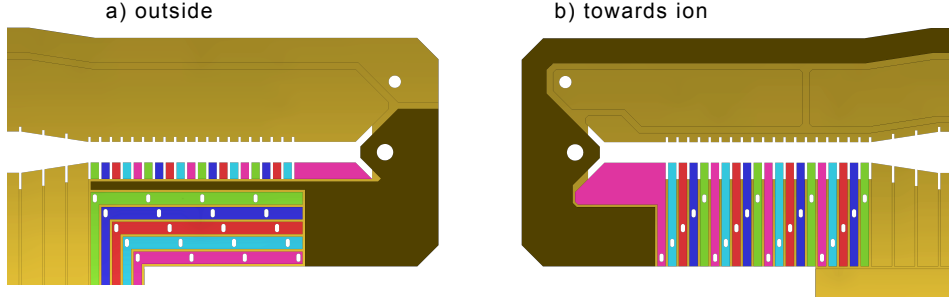


**Figure 4.3.:** a) frontside and b) backside of the small region of the trap assembly's top layer, where the backside faces the trap axis. The layout of the bottom layer is designed analogously. Areas of the same color are on the same electric potential, all holes in the substrate shown in this figure form VIAs. Each colored horizontal conducting path depicted in a) connects four electrodes through VIAs and the vertical conducting paths shown in b). Effectively, five conducting paths to the outside connect a total of 20 electrodes. The shaded area is constantly on ground potential, its long horizontal protrusion shown in a) minimizes the electrical field originating from the voltage-carrying horizontal conducting paths on the trap axis.

### RF- and RF Compensation Electrodes

The ion's position along the trap axis can be thoroughly controlled by applying appropriate Voltages to the DC segments in the ion's vicinity. To place the ion in the center of the fiber cavity's mode, which has a typical diameter of  $\approx 5\mu\text{m}$ , it is also necessary to control the position of the trap's RF minimum. The fibertrap features two independently contacted RF electrodes, which makes a precise positioning of the RF minimum possible by applying two different RF voltage levels [Her09]. In order to be able to compensate the the ion's micromotion in both radial directions, two additional electrodes are located next to each RF electrode, so compensation along two radial directions is possible with this design, independently for the region, where the fiber cavity is located, and the remainder of the trap, see Fig. 4.4.

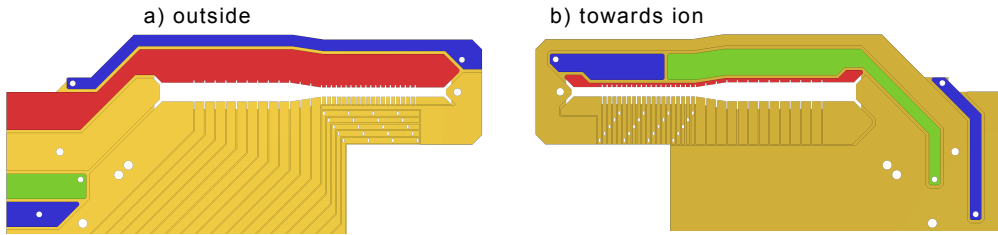


**Figure 4.4.:** RF electrode and compensation electrodes and corresponding conducting paths of the trap assembly's top layer. The layout of the bottom layer is designed analogously. a) Outward facing side with bond pads. b) Side facing the trap axis. Areas of the same color are on the same electrical potential, and connected by VIAs, where applicable.

### 4.1.3. Trap Fabrication

Alumina ( $\text{Al}_2\text{O}_3$ ) is used as substrate material for all three layers of the trap assembly. For the top layer and the bottom layer, commercially available substrates<sup>1</sup> with a thickness of 125  $\mu\text{m}$  are used, the thickness of the material used for the spacer is 250  $\mu\text{m}$ . This allows for the insertion of a fibercavity made from standard fibers with 125  $\mu\text{m}$  diameter between the top layer and the bottom layer, without physical contact. Also, fibers with a diameter of 200  $\mu\text{m}$  might be used in the future. The first processing step is the cutting of the trap structure, i.e. the holes used as VIAs and the trap slit by femtosecond laser cutting<sup>2</sup>. Afterwards, the cut substrate is evaporatively coated first with a 50 nm Titanium adhesion layer, and then with 500 nm of Gold. In a third step, the conducting paths are separated again by femtosecond laser cutting, where this time the laser only cuts through the metal coating, and not through the substrate itself. Finally, holes used for glueing and alignment are cut, and the trap chips are diced from the surrounding substrate material. For the spacer, the production steps associated with the metal coating do not apply, only the substrate cutting is performed. The whole process is the same as in [Sch09], where it is described in more detail.

The three layers which constitute on trap assembly are fixed by UV-hardened glue<sup>3</sup>, which is applied through holes in the chips designated for that purpose. The relative alignment of the chips is done manually, using a microscope. To that end, the chips are put on a platform, stacked, and carefully moved with respect to each other using a pair of tweezers. It became apparent, that the small VIAs used for the coupled DC electrodes are very susceptible to physical damage when touching the platform surface during the alignment process, especially if that surface is subject to electrostatic charging. As any kind of metal as a platform material would be too hard, producing scratches or other kinds of damage to the Gold-covered chips, a soft, but conductive plastic material<sup>4</sup> has been chosen for the platform. As an additional measure, care has been taken, that the part of the trap chip, where the VIAs are located, never directly touches the platform surface, but only the rest of the chip.

---

<sup>1</sup>Reinhardt Microtech GmbH, Sedanstraße 14, 89077 Ulm, Germany

<sup>2</sup>Micreon GmbH, Garbsener Landstraße 10, 30419 Hannover, Germany

<sup>3</sup>OG 116, Epoxy Technology, Inc., 14 Fortune Drive, Billerica, MA 01821

<sup>4</sup>S plus+ Bright ESD, Murtfeldt Kunststoffe GmbH & Co. KG, Heßlingsweg 14-16 44309 Dortmund, Germany

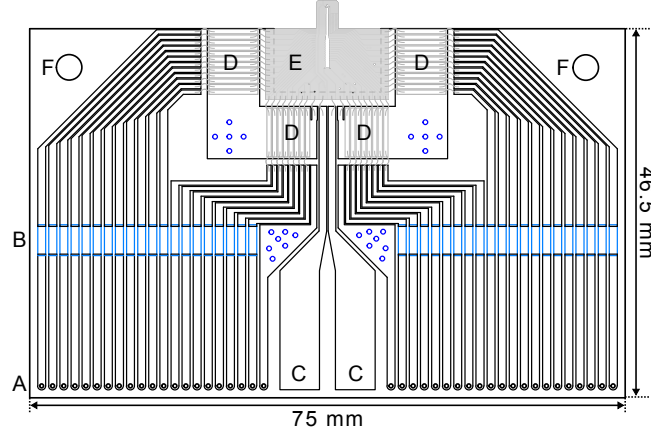


**Figure 4.5.:** Drawing of the low-pass filterboard. Through the holes (A), cables are soldered to the conducting paths of the board providing DC electrode- and ground connections. The blue parts of the conduction paths (B) are the printed  $30\ \Omega$  resistances. The wires carrying the trap's RF voltage are soldered to the large pads (C). The capacitance arrays (D) are also soldered to the filterboard, before the trap assembly (E) is attached using glue. All electrical connections from the board to the capacitance arrays, and to the trap are realized by wire bonds. The holes (F) are used for mounting the board to a holder construction at the vacuum flange. The blue holes depict VIAs connecting ground planes on the backside of the filterboard.

#### 4.1.4. Filterboard for Electrical Connections

In order to reduce technical noise, an RC low-pass filter is inserted in the connection of each DC segment. For this purpose, a in-vacuum filterboard is used, which is depicted in Fig. 4.5. The trap assembly is directly mounted on this filterboard, using again the UV-hardened glue. The electrical connections of the trap assembly to the board are provided by wirebonding.

The conducting paths and the resistances are realized by sintered thick-film printing on an Alumina substrate<sup>5</sup>. Row capacitors<sup>6</sup> are used as the capacitances for the low-pass filters. Lead-free solder paste is used connect the filterboard's conducting paths to UHV-compatible cables, which in turn provide the electrical connection to the outside of the vacuum vessel by means of electrical feedthroughs. The low-pass filters' cut-off frequency reads  $\omega_c = 2\pi \times 1.33\ \text{MHz}$  with resistances and capacitances of  $R = 30\ \Omega$  and  $C = 4\ \text{nF}$ .

<sup>5</sup>Institut für Aufbau- und Verbindungstechnik, Technische Universität Dresden, Helmholtzstraße 10, 01069 Dresden, Germany

<sup>6</sup>Compex Corp. 439 Commerce Lane, West Berlin, New Jersey, 08091, USA

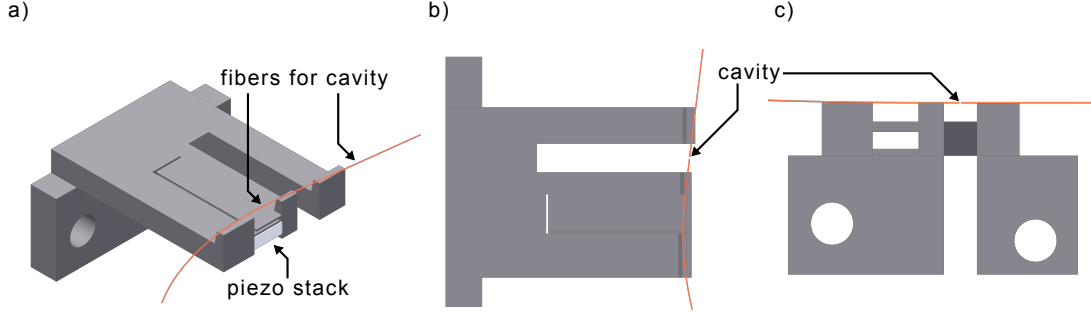


**Figure 4.6.:** Isometric (a), top (b) and front (c) view of the fiber cavity assembly. Titanium was used as material for the holder, the fibers are depicted in red, the piezo stack for scanning the cavity length is depicted in white.

##### 4.1.5. Fiber Cavity Assembly

The core feature of the discussed trap design is its possibility to be equipped with a fiber cavity. In order to reduce the overall complexity of the setup, the trap assembly and the fiber cavity assembly have been designed as distinct entities, which can be constructed, tested and operated independently. Once both parts are working as required, they can be joined and operated together. This thesis mainly discusses the the trap assembly, but to provide context for the reader, a short overview of the cavity assembly is given here as well.

The end facets of two optical fibers are used to form an optical cavity [Ste06, Hun10]. Light is coupled to this cavity via a single mode fiber, whereas a multi mode fiber is used on the outcoupling side. Such a cavity, intended for the use in the trap assembly, is described in detail in [Pfi16]. It has a length  $L = 250 \mu\text{m}$ , which allows for hiding the fibers behind the electrode structure of the trap. The mirror geometry is plano-concave, where the single mode fiber features a plane surface, and the radius of curvature for the multimode fiber is  $350 \mu\text{m}$ . This geometry gives a beam diameter of  $\approx 7 \mu\text{m}$  at the position of the ion in the cavity. The shaping of the fiber facets is done using a focused ion beam device. The description of the basic concept of that technique can be found in [Sal13]. A dielectric mirror coating is applied to both fiber facets, yielding a cavity with a Finesse  $\mathcal{F} \approx 16000$ .

The two fibers which comprise the cavity are mounted on a solid fork-like titanium structure. One of the two fork arms can be moved by a piezo stack in order to scan the cavity length (see Fig. 4.6). This structure can be mounted in such a way to the trap assembly, that the two fibers are exactly located in between the top layer and the bottom layer of the trap (see Fig. 4.2 c).



All details about the fiber cavity assembly given above need to be considered work-in-progress, especially as the development of fiber cavities has attracted a lot of interest recently and is evolving rapidly [Bra13, Tak14, Gal16, Uph16, Ott16].

## 4.2. Characterization Measurements

In order to verify that the setup incorporating the fibertrap assembly described above is working as intended, characterization experiments have been performed. In the following, the rest of the experimental setup apart from the fibertrap assembly required for operation is briefly described. Then simulations of the fibertrap's axial trap frequencies are compared to measurements. Finally, coherent operations on the optical qubit including sideband cooling are discussed.

### 4.2.1. Experimental Setup

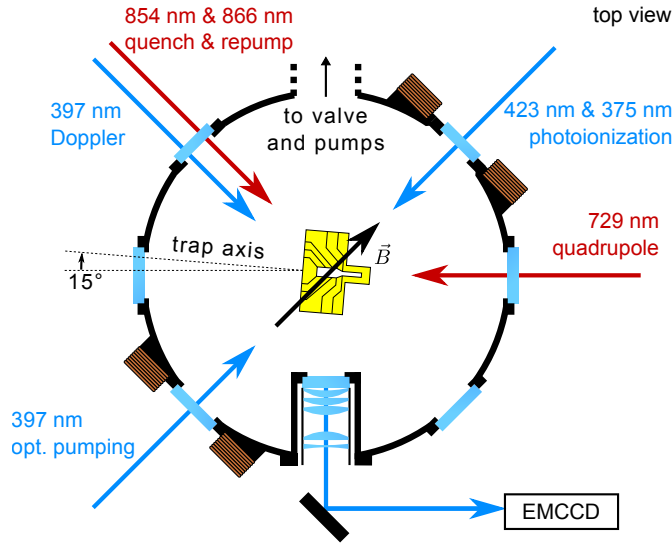


**Figure 4.7.:** Fibertrap vacuum vessel together with directions of incident laser beams. A high-NA objective lens in a inverted viewport is used for imaging the ions on a EMCCD camera. Note the tilt of the trap axis with respect to the direction given by the viewports.

The trap assembly together with the filterboard and the cabling has been put in a vacuum vessel (for details, see [Zie12]), the end pressure being  $2 \times 10^{-10}$  mbar. The trap assembly has been tilted relative to the viewports of the vessel to establish the possibility of having a small angle between the trap axis and the quadrupole laser. The vacuum setup together with the incident laser beams is depicted in Fig. 4.7.

The basic laser setup consists of a Doppler cooling laser with a wavelength close to 397 nm, a repump laser close to 866 nm, and a quench laser close to 854 nm. Two lasers are used for two-step photoionization of neutral Calcium, one close to 423 nm, and one at roughly 375 nm. The setup is very similar to the respective systems described

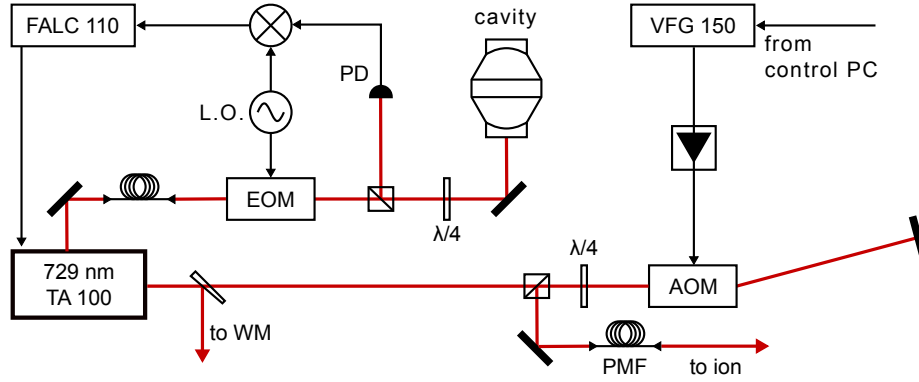


**Figure 4.8.:** Optical setup for the diode laser near 729 nm used for driving the quadrupole transition. The reflection signal of a high-Finesse cavity is used to create a PDH error signal. A fast regulator module then locks the laser to the cavity by acting on both the diode current and grating piezo.

in chapter 3. The quadrupole transition is driven by an amplified diode laser system providing up to 500 mW of laser light close to 729 nm<sup>7</sup>. It is locked to a high Finesse cavity<sup>8</sup> to ensure the narrow linewidth needed for driving the quadrupole transition. This system is depicted in Fig. 4.8 in more detail.

#### 4.2.2. Static and Dynamic Trap Potential Control

##### Single Ion Trapping

The first step of trap operation and characterization is statically trapping single ions. To this end, an oven [Rot03], located inside the vacuum vessel and filled with Calcium granules<sup>9</sup> is heated up by 2 to 4 A of electrical current to provide a constant current of neutral calcium vapor in the vicinity of the trapping structure. An isotope selective two-step ionization process using two lasers close to 423 nm and 375 nm is used to produce singly-charged  $^{40}\text{Ca}^+$  ions. An RF drive signal with a frequency of 18.6 MHz and a Voltage between 150 to 500 V<sub>pp</sub> is applied to the respective trap electrodes. This signal is produced by DDS source<sup>10</sup>, amplified<sup>11</sup> and impedance matched to the trapping structure by a custom-made helical resonator.

<sup>7</sup>TA 100, Toptica Photonics AG, Lochhamer Schlag 19, 82166 Gräfelfing, Germany

<sup>8</sup>Advanced Thin Films, 5733 Central Avenue, Boulder, CO 80301, USA

<sup>9</sup>Calcium granules, redistilled, -16 mesh, 99.5% (metals basis), Alfa Aesar GmbH & Co KG, Zeppelinstr. 7b, 76185 Karlsruhe, Germany

<sup>10</sup>SMC100A, Rohde & Schwarz GmbH & Co. KG, Mühldorfstr. 15, 81671 München, Germany

<sup>11</sup>ZHL-5W-1, Mini-Circuits, Europe Dale House, Wharf Road Frimley Green, Camberley, Surrey GU16 6LF, United Kingdom

For the described characterization experiments, only one of the trap's segments is used at the same time, the others are set to ground potential. The trapping segment's DC voltage is set between 3V and 9V, depending on the desired axial trap frequency. It is supplied by a custom made FPGA based multichannel voltage supply [Zie12]. Mappings of the electrical in-vacuum connections to the feedthroughs provided by the vacuum vessel can be found in appendix C.

For Doppler Cooling, the ion is subjected to a laser field close to 397 nm,  $\approx 10$  Mhz detuned from resonance, and a laser field close to 866 nm for repumping. Fluorescence detection is performed using an high-NA objective lens<sup>12</sup> and an EMCCD camera<sup>13</sup>.

### Potential Simulations and Measurements

While the geometrical structure of the fibertrap's electrodes is identical to the design from [Sch08], this holds not true for the immediate surroundings of the electrode structure. Especially the conducting paths close to the small region which are running in parallel to the trap axis significantly differ from the original design.

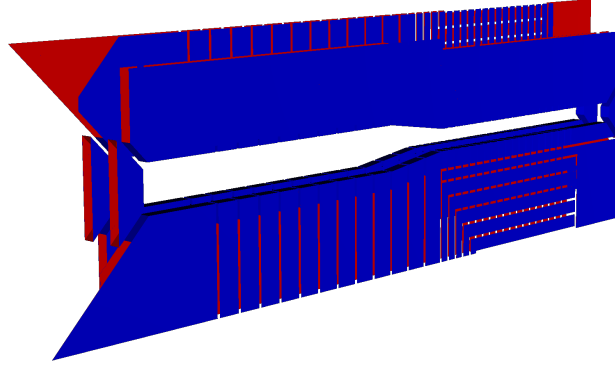


**Figure 4.9.:** Visualization of the extended 3D-model of the fibertrap used for simulating the axial trapping potentials. Not only the trap electrodes have been taken into account, but also their immediate surrounding, especially the part, where the VIAs are located

To study the influence of that structures on the trap frequency on different positions along the trap axis, an electric field simulation using a readily available software package [Sin10] has been performed. It is based on the boundary element method [Poz02], therefore only the electrode surface needs to be discretized. This results in a significant

---

<sup>12</sup>S6ASS2214/45, Sill Optics GmbH & Co. KG, Johann Höllfritsch-Str. 13, 90530 Wendelstein, Germany

<sup>13</sup>ixon+, DU-860D-CS0-UVB, Andor Technology Ltd., 7 Millenium Way, Springvale Business Park, Belfast BT12 7AL, United Kingdom

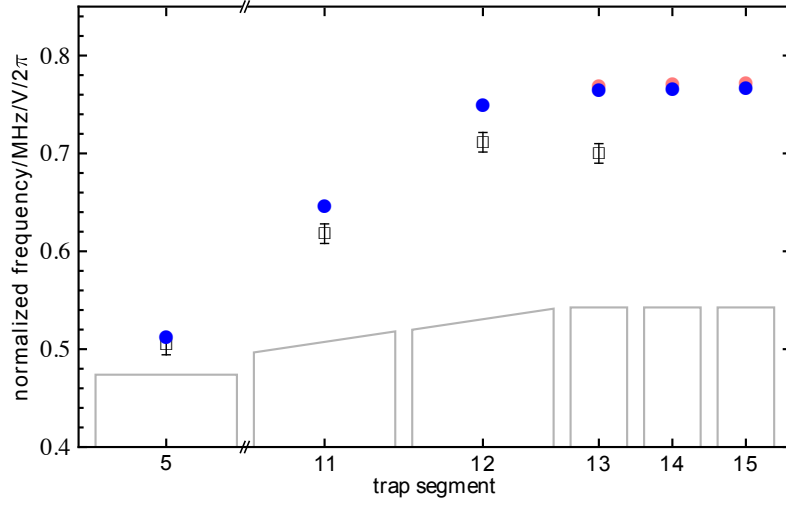


**Figure 4.10.:** Axial frequencies if 1V is applied to one DC segment, and 0V to all others for segments in the loading region, the taper, and the processing region of the fibertrap. Open squares are measured data, filled dots are the results of a BEM simulation [Sin10] of the electrode structure. For the red dots, the coupling of the electrodes in the processing region and the connection stripes shown in Fig. 4.3 have been neglected, while both has been taken into account for the blue points.

calculation speedup compared to finite element methods, where the whole field volume of interest needs to be discretized. Due to this speedup, a field calculation of adequate accuracy of not only the the trap’s electrode structure itself, but also the conducting paths in their close vicinity can be performed on a standard desktop PC in less than one hour of time. The model used for those field calculations is shown in Fig. 4.9, where the structure of the conducting paths in the vicinity of the electrodes has been taken into account.

Fig. 4.10 shows the results of spectroscopic trap frequency measurements with a single ion together with calculated values. Two different configurations have been used in the calculations. One, where the coupled electrodes are set to the same potential, together with the respective conducting paths. This is the realistic setting as implemented by the design of the trap. For comparison, a second, idealized configuration has also been simulated, where all electrodes are treated independently, and the conducting paths used for electrode coupling are always fixed to 0 V. The comparison of those two simulations shows differences on the sub-percent level in the trap’s small region, and are quickly decreasing in the tapered and the large region of the trap. Measured values in the trap’s large region coincide with the simulation results, however, for ion positions in the taper and the small region, considerable discrepancies to both simulation settings appear as the ion enters the taper, reaching almost  $\sim 10\%$  in the small region. This indicates deviations of the simulation model from the actual trap. The following list

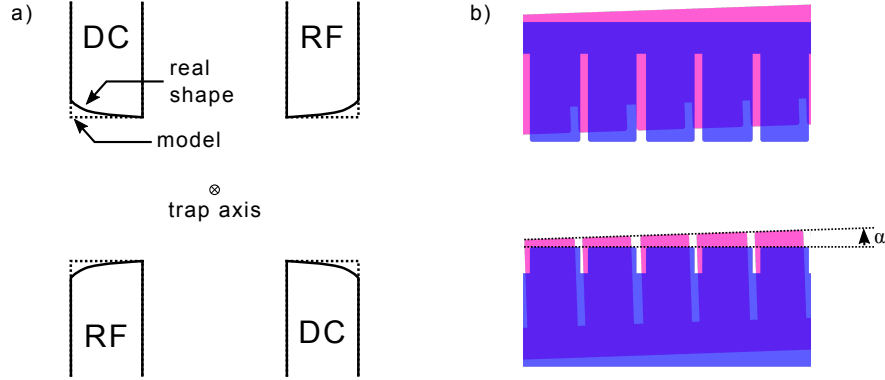


**Figure 4.11.:** Deviations of the real trap geometry from the idealized model used for simulations. a) The shape of the electrodes is not perfectly rectangular, but rolls off at the edges due to the fs-laser cutting process. b) The toplayer and the bottomlayer of the trap are presumably misaligned, e.g. top layer and bottom layer might have an unwanted relative angle  $\alpha$ .

contains features of the real trap structure, which have not been adequately reproduced in the simulation model to keep modeling and simulation effort under control:

- The holes, which actually constitute the VIAs (see Fig. 4.3) are not modeled.
- The shape of the electrode structure as produced by the fs-laser cuts is simplified. In the model, the fs-laser produces cuts exactly parallel to its direction of propagation. This is not entirely correct as the true resulting shapes are more complex, see Fig. 4.11 a).
- Top- and bottom layer of the trap structure are manually aligned with respect to each other using optical microscopes. This makes a certain misalignment inevitable, see Fig. 4.11 b). Because the misalignment cannot be straightforwardly quantified, it is not taken into account in the simulation model.

As the discrepancies are quite large, they are not likely caused by only minor simplifications of the simulation model far away from the ion position. It is more likely, that the second and the third issue are the main reasons for the deviations. The second issue is expected to lower the trap frequencies the more the smaller the electrode-ion distance becomes, the third issue is expected to lower the trap frequencies the more, the smaller geometrical dimensions the electrode has. The data in Fig. 4.10 shows both kinds of behavior, and is thus compatible with those assumptions. It is also interesting to note, that the ion's axial positions of the two simulations differ only very little, i.e. by  $\sim 1 \mu\text{m}$ .

From the two simulations in conjunction with the experimental data it can be concluded, that the considerable design change of the fibertrap compared to the original design has only minor influences on the potentials provided by the trap. Errors due to manual alignment of the trap assembly and inaccuracies in the modeling of trap electrode structures very close to the ion seem to have a much larger impact than the rather unorthodox conducting path routing of the fibertrap.

That being said, a future limitation imposed by the fact that the electrodes in the small region are not independently addressable concerns the ability to split ion crystals, and afterwards shuttle the resulting subcrystals independently along the axis. One requirement for ion crystal splitting as discussed in [Rus14, Kau14] is a set of five independent electrodes, which the fibertrap can provide. Independent transport of multiple ion crystals in the small region is not possible though, at least in a straight forward way. For now, this feature is only of minor significance, but future trap designs might address that issue.

### Axial Ion Transport

Whereas the measurements discussed above were performed by only applying static voltages to the electrodes of one specific trap segment, the actual purpose of the trap design is ion transport along the axial direction by dynamically changing the voltages applied to the DC electrodes<sup>14</sup>. Ion transport in segmented traps has been studied extensively, as discussed in chapter 2.4. In the fibertrap, adiabatic axial ion transport has been implemented as a proof of principle by applying linear voltage ramps on the segment electrodes. To this end, a single ion was successfully transported from segment 5 to segment 16 of the trap, covering a total distance of  $\approx 2.5$  mm in  $\approx 1$  s. Further transport was impeded by damaged DC electrode connections. By choosing a moderate RF voltage of  $180 V_{pp}$ , it was possible to transport from the large region through the taper into the small region of the trap while leaving that voltage constant without leaving the trap's stability region.

---

<sup>14</sup>The term “DC electrode” might become misleading in the context of ion transport, depending on the frequency components present in the signal applied to this electrode.

### 4.2.3. Coherent Dynamics and Sideband Cooling

Sufficient control over an ion's external and internal state is a necessary precondition for performing any experiments in the quantum regime. The main purpose of the trap structure discussed in this thesis is to be part of an interface for coherent interactions between a single ion and a single photon. Many different schemes and variations of atom-photon interfaces are described in recent literature [Rei15], the case of single  $^{40}\text{Ca}^+$  ion is discussed in [Pfi16], where in the context of a quantum repeater realization three of those schemes are elaborated on in detail. One experimental requirement, which all of those schemes have in common, is the control of the  $4^2S_{1/2} - 3^2D_{5/2}$  quadrupole transition, mediated by a stable laser source close to 729 nm (see Fig. 4.8). Precise control of the external degree of freedom on the single or few motional quanta level has not the same relevance for a light-ion interface, but having this kind of control extends the scope of the platform considerably, as the coupling of the system's internal and external states (see Eq. 2.28) is the basis for the most prominent two-qubit entangling gates [Lei03b, SK03, Kir09]. Have this degree of multi-qubit control available is what distinguishes the discussed platform from others, e.g. based on cold neutral atoms. Especially for implementing a quantum repeater platform, this kind of control becomes crucial.

In the following, those dynamics on the quadrupole transition of a single ion in the fibertrap are studied, and the applicability of the system for the intended purposes is evaluated. The employed experimental techniques follow generally those found in recent ion trapping literature [Sch13]. The specifics for the apparatus developed in the context of this thesis are discussed in the following.

#### State Initialization and Sideband Cooling

After Doppler cooling, optical pumping using  $\sigma^+$ -polarized light near 397 nm, directed along the magnetic field is employed to initialize the ion's internal state to the  $m = +1/2$  Zeeman sublevel of the  $4^2S_{1/2}$  manifold (see Fig. 4.7). Afterwards, pulsed sideband cooling is performed [Esc03] by first driving the red sideband of the quadrupole transition using the stabilized laser near 729 nm, and second quenching the  $3^2D_{5/2}$  manifold with a laser field close to 854 nm (see Fig. 4.12). The short-lived  $4^2P_{3/2}$  state then quickly decays back to the initial state. During such a closed transition, the motional state of the ion is reduced by 1 excitation quantum. This cycle is repeated 30 to 60 times to attain the motional state with the lowest possible mean excitation number  $\bar{n}$ . To correct for unwanted processes, which make the ion end up in the wrong Zeeman substate ( $m=-1/2$ ), every 10 cooling cycles, a short pulse of  $\sigma^+$ -light is used to ensure,



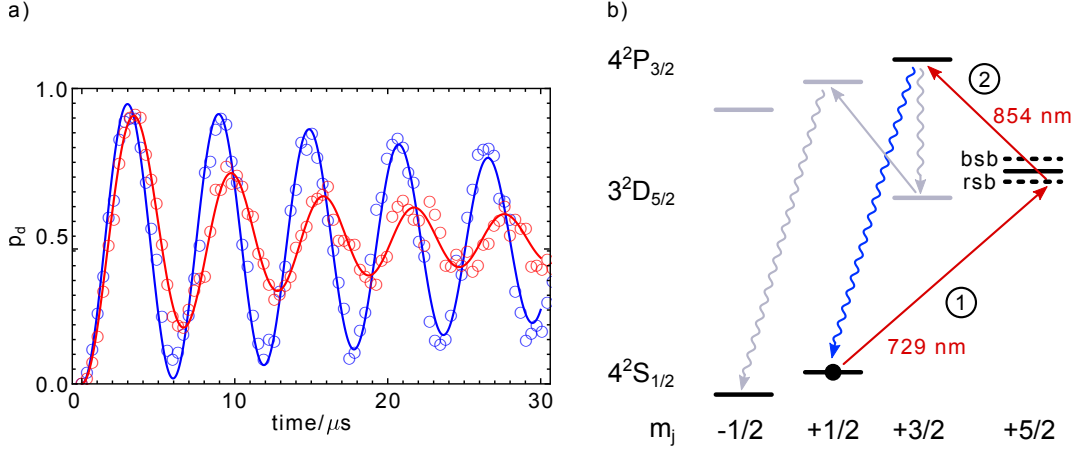


**Figure 4.12.:** a) Coherent dynamics on the carrier after Doppler cooling (red) and sideband cooling (blue). Open points depict measured data, continuous lines are fits of Eq. 4.2, yielding  $\bar{n} = 30.9$  for the Doppler cooled- and  $\bar{n} = 6.9$  for the sideband cooled case. Data is taken in segment 13 of the fibertrap  $\omega_{ax} = 2\pi \times 2.16$  MHz b) Relevant levels and transitions used for the pulsed sideband cooling scheme. After initialization, a  $\pi$ -pulse is driven on the red sideband of the quadrupole transition, and then the population is quenched from the  $3^2D_{5/2}$ -state. The population then quickly decays back to the initial state. Parasitic transitions, which cause a deterioration of the spin polarization are shown in grey. They are counteracted by inserting pulses for optical pumping every 10 cooling cycles.

that the ion is back in the  $m = +1/2$ -state. Note, that not every single pulse removes exactly one excitation quantum, as the probability to successfully drive the red sideband transition is reduced by lowering  $\bar{n}$ . When the cooling rate equals the heating rate of the system, the minimum temperature is reached, and additional cooling cycles do not reduce the temperature further.

### Coherent Interaction

As shown in chapter 2.2.3, driving coherent dynamics on the quadrupole transition allows for drawing conclusion on the motional state of the ion. To this end, a pulse of the laser field close to 729 nm, resonant to either the carrier or the sideband transition is applied. The length of that pulse is scanned over repeated, otherwise identical experiments.

### State Projection and Readout

After the coherent interaction, the ion's state is projected to either the  $4^2S_{1/2}$  state, or the  $3^2D_{5/2}$  state by switching on the laser fields close to 397 nm and 866 nm and

detecting the ion's fluorescence with the EMCCD Camera for 1.5 ms. Only the  $4^2S_{1/2}$  state is fluorescing, the  $3^2D_{5/2}$  state remains dark. After repeating 200 identical experiments, the probability of the ion being dark,  $p_d$  is obtained, being equivalent to the ion occupying the  $3^2D_{5/2}$  state. Repeating this sets of experiments for different pulse times of the quadrupole laser field yields data as shown in Fig. 4.12.

Those dynamics can be understood employing Eq. 2.38, with one additional parameter  $C$  added, which accounts for imperfect optical pumping, reducing the maximally attainable excitation. The function used for fitting the measured data  $f(t)$  thus reads

$$\begin{aligned} f_m(t) &= C \sum_n p_n^{\bar{n}} \sin^2 \left( \frac{1}{2} \Omega_{n+m,n} t \right) \\ &= C \sum_n \frac{\bar{n}^n}{(\bar{n} + 1)^{n+1}} \sin^2 \left( \frac{1}{2} \Omega_0 e^{-\eta^2/2} \eta^{|m|} \mathcal{L}_q^{|m|}(\eta^2) \left( \frac{q!}{(q+m)!} \right)^{1/2} t \right), \end{aligned} \quad (4.1)$$

$q$  denotes the lesser of  $n$  and  $n + m$ . The explicit form directly reveals the fitting parameters: The Rabi frequency of the ground state  $\Omega_0$ , the mean excitation number  $\bar{n}$  and the pumping efficiency  $C$ . The Lamb-Dicke parameter  $\eta$  is predetermined from the experimental setup geometry.  $m$  denotes the sideband, to which the function applies.  $f_0(t)$  refers to the carrier transition,  $f_{-1}(t) = f_{rsb}(t)$  to the first red sideband- and  $f_{+1}(t) = f_{bsb}(t)$  to the first blue sideband transition.

Fig. 4.12 a) compares coherent dynamics on the quadrupole transition of a single ion for the Doppler cooled- and the sideband cooled case. The data is shown together with the fitted functions  $f_{car}(t)$ . The motional excitation of  $\bar{n} = 6.9$  after sideband cooling is considerably lower than for the Doppler cooled case  $\bar{n} = 30.9$ , but substantially higher than for traps of comparable size and fabrication where motional excitations  $\bar{n}$  of way below one phonon are achieved [Bro15, Kie14]. Data for studying the trap's heating rate in more detail is shown in Fig. 4.13. Here, carrier and red sideband transitions are driven in an interleaved fashion for otherwise identical experimental parameters. This allows for mutually fitting  $f_{car}(t)$  and  $f_{rsb}(t)$  using the same parameter set. To obtain the rate of excitation change over time,  $\dot{\bar{n}}$ ,  $\bar{n}$  is measured for different waiting times are inserted between cooling and the coherent dynamics pulse. For the data from Fig. 4.13, the heating rate reads  $\dot{\bar{n}} = 16.5/\text{ms}$

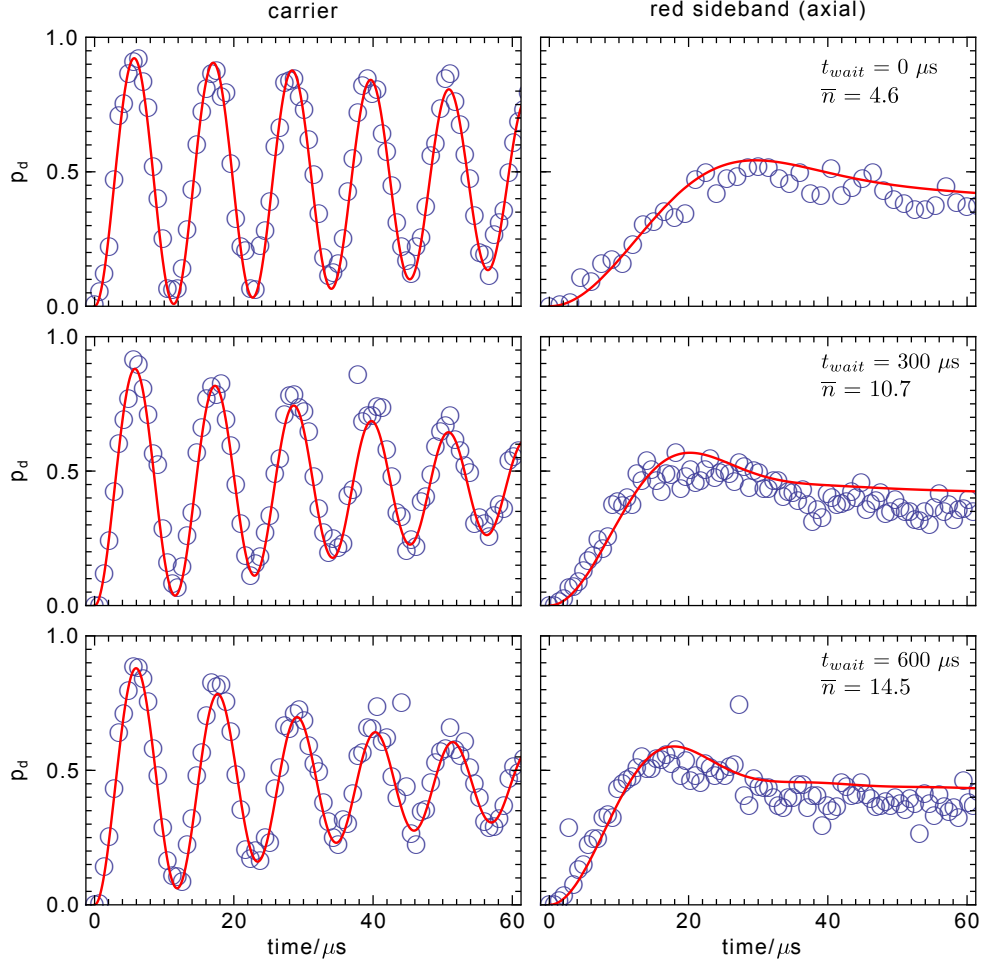


**Figure 4.13.:** Pulse width scans on the quadrupole transition for the carrier and the red sideband after different waiting times. Open circles are measured data, continuous lines are combined fits of Eq. 4.2 (see main text for details). The heating rate in this case reads  $\dot{n} = 16.5/\text{ms}$ . Data is taken at segment 5 of the fibertrap ( $\omega_{ax} = 2\pi \times 1.32 \text{ MHz}$ ).

### 4.3. Discussion

As pointed out especially in chapter 4.1 the requirements for an ion trap intended for ion-photon interfacing are not only quite specific, but also the implementation of those requirements leads to technical challenges, which might not be immediately apparent. The most prominent of those challenges is arguably the necessity for VIAs in the design and following from that, the coupling of electrodes in the small region of the trap. In the end, the trap was based on the design from [Sch09] but heavily modified to account for the mentioned requirements.

In order to make sure, that this modified design still can be operated as intended, trapping potentials in axial directions have been simulated using the software package from [Sin10]. For this, not only the electrode structure has been modeled, but also the immediate surrounding conducting paths. Their influence on the trapping potentials has been found to be insignificant. Comparisons with experimental data show, that deviations presumably due to imperfect electrode alignment are much larger.

For the manufacturing of the trap structure, a rather conservative approach has been taken. The trap was fabricated from Alumina substrates using fs-laser cutting, electrodes and conducting paths consist of evaporated gold. The different trap layers have been glued together, and the trap was attached to board providing low pass filters and wiring to the outside. During the assembly, special care needed to be taken to not damage the VIAs.

After the assembly, the trap was set up in a UHV vessel and was operated using a diode laser setup, DC voltages were supplied by an FPGA based multichannel voltage supply. Single ions have been trapped in all three regions of the trap, and could be successfully transported axially. Also, single ions have been sideband cooled, and a heating rate of  $\dot{n} = 16.5/\text{ms}$  in the large region has been measured at an axial trap frequency  $\omega_{ax} = 2\pi \times 1.32 \text{ MHz}$ .

In summary, the trap assembly, designed and implemented as described, has been found to work as intended. It provides the required features needed for an ion-photon-interface trap, namely stable trapping and axial transporting of single ions in all trap regions and good coherent control of the ion's internal state is possible employing a suitable laser for driving the quadrupole transition.

On the downside, the VIAs in the trap structure have appeared to be very fragile. The provided connection can easily be destroyed by even minor physical stress during the assembly process, or by currents, which are induced by the capacitive coupling of the RF- to the DC electrodes, if the voltage of the RF drive is chosen too high. Moreover,

the heating rate is relatively high, when compared to other traps with comparable ion-electrode distances [Bro15], and cooling the ion close to the motional ground state is not possible. This is of only minor relevance for the intended ion-photon coupling, but it impedes the realization of high-fidelity two-ion entangling gates, which would largely increase the options for future applications. There is one improvement however, which can possibly be applied to tackle both of these major challenges, namely increasing the gold layer's thickness by an additional electroplating step during the fabrication. Thicker Gold layers in microstructured traps are one known possibility to reduce heating rates, although the underlying processes are not yet completely understood. As the VIAs are known to reliably work before eventually being damaged by external means, the additional Gold applied during the electroplating process will reduce their resistance, presumably enough to withstand the currents induced by capacitive RF coupling for typical RF drive voltages.



## 5. Conclusion and Outlook

Cavity QED experiments with ions have been always somewhat more cumbersome than with neutral atoms, but the unrivaled control of the external and internal quantum states of ions make the quest of strong light-ion coupling an extremely promising one. Recent developments in technology, namely the appearance of segmented microtraps and fiber cavities have considerable potential for progress towards that goal. The trap structure discussed in chapter 4 has been designed from the start for being combined with a fiber cavity. It has been successfully operated and characterized, and its operation together with a fiber cavity should be rather straight forward in the near future. There are however details in the design which have been proven to be suboptimal during the trap's characterization measurements: The VIAs are very susceptible to mechanical or electrical damage, and the heating rate of the trap is higher than expected. While the latter is not an immediate problem in the context of CQED experiments, the former definitely is. It is promising though, that both issues have been reported recently to be solved by the same kind of cure, namely making the Gold layer on the trap substrates thicker by electroplating. This poses an additional step in the already quite complex trap manufacturing process, but it is well justified by potentially resolving the two most prominent issues of the design. Apart from those limitations, the trap allows for directly making use of the toolbox for quantum computation of segmented ion traps developed in recent years, like fast transport and splitting/merging of ion crystals, and performing high-fidelity quantum gates, and by those means has the potential to push CQED experiments far beyond today's limits.

Improvements for the more distant future include a simplification of the trap manufacturing process. More specifically, the necessity to assemble the trap's three-layer structure by hand is something worth overcoming. This calls for using planar trap structures, which can be manufactured in a monolithic fashion, but the implementation of a fiber cavity in such a structure is not straight forward, and calls for further work and new concepts.

The measurements presented in chapter 3 resolved a remarkable discrepancy between the theoretical calculations [Saf11] and the most recent experimental results predating this work [Jin93] of the  $4^2S_{1/2}$  states' radiative lifetime  $\tau$ . The discrepancy in the

## 5. Conclusion and Outlook

---

specific case of  $^{40}\text{Ca}^+$  was all the more puzzling, as similar calculations for alkaline-like species from Li to Fr,  $\text{Mg}^+$ ,  $\text{Ba}^+$  and  $\text{Sr}^+$  are in good agreement with experimental results (see [Saf11] and references therein).

Moreover, the presented new method allows for not only measuring the lifetime  $\tau$ , but also the radiative decay rates  $\gamma_{PS}$ ,  $\gamma_{PD}$  and  $\tilde{\gamma}_{PS}$ , which in turn can be used to directly determine the reduced dipole matrix elements  $\mathcal{D}_{PS}$ ,  $\mathcal{D}_{PD}$  and  $\tilde{\mathcal{D}}_{PS}$ . This multitude of interdependent, but different quantities allows for a wider comparison to theoretical and experimental literature, compared to only determining one singular quantity like  $\tau$ . Also, the way how the measurements are constructed by choosing different detuning parameters, and the way how the results are evaluated ensures a certain self-consistency of the data, which would not be achieved by just repeating identical measurements of the same quantity. Moreover, the described method is not limited to the  $^{40}\text{Ca}^+$  ion, but can be employed by other atom or ion species, which allow for preparation and readout of Zeeman or hyperfine sublevels.

The reduced dipole matrix elements  $\gamma_{PS}$  and  $\tilde{\gamma}_{PS}$  enter in the calculations of the black body radiation (BBR) shift of the  $4^2S_{1/2} \leftrightarrow 3^2D_{5/2}$  and the  $4^2S_{1/2} \leftrightarrow 3^2D_{3/2}$  quadrupole transition, both of which are widely used in a variety of laser spectroscopy experiments, e.g. [Chw09, Kre05, Geb15]. The BBR shift is among the major contributions to the uncertainties of clock transition frequencies, for species such as  $^{43}\text{Ca}^+$  [Aro07],  $\text{Sr}^+$  [Dub13],  $\text{Sr}$  [Saf13, Blo14], and  $\text{Yb}$  [Lud15]. These are used for state-of-the-art optical clock experiments, and some of them are discussed as new SI frequency standards. The presented results add to existing work [Bel14, Dub14, Mid12] validating computational methods used to predict the BBR shift in optical clocks.

As table 3.1 shows, the measurement uncertainty of the method can be further reduced by technical means. The largest contributor is the possible presence of  $\epsilon_0$ -polarized light. In a future refined version of the setup,  $\epsilon_0$  could be determined by not only measuring the differential AC-Stark shift  $\Delta_S$  but also the absolute AC-Stark shifts of both levels, which would eliminate  $\epsilon_0$ -polarized light as an error source. The uncertainty of the resonance frequency and the statistical uncertainty can be minimized by taking more data. In order to do so, without overly increasing the measurement time, it is possible to reduce the duration of both sequences considerably. AOM warmup times can be minimized, e. g. by applying water-cooling, and the reason for the long detection time is mainly a PMT performing not optimally, which also leaves room for improvement. Also, using more power in the off-resonant laser makes it possible to shorten the time window for the spin flips. Tackling these issues puts the measurement of dipole matrix elements with uncertainties in the  $10^{-4}$  regime well within reach.



## A. Uncertainties of the Matrix Element Measurements

In this appendix, statistical and systematic uncertainties and corrections of  $R_+$ ,  $R_-$ ,  $\Delta_S$  and  $\Delta$  and their effect on decay rate  $\gamma_{PS}$  and the leak factor  $b$  are discussed and quantified. In the end, the calculations giving the resulting total uncertainties of  $\gamma_{PS}$ ,  $\gamma_{PD}$ ,  $b$  and  $\tau$  are performed. The treatment follows largely the one given in the supplemental material of [Het15].

### A.1. Data Overview

For four different detunings ( $\Delta_i, i = \{1, \dots, 4\}$ ), two chosen on the blue side and two on the red side of the resonance,  $N_i = \{18, 17, 14, 16\}$  data sets have been acquired, which are used for determining pairs of spin-flip rates ( $R_{+,i,j}$  and  $R_{-,i,j}, i = \{1, \dots, 4\}, j = \{1, \dots, N_i\}$ ) and leak factors  $b_{i,j}$  by fitting the data sets to Eq. 3.27. Before and after recording each spin-flip rate/leak factor data set, one spin-echo type data set is acquired, which allows for determining an AC-Stark shift. The mean of those two embracing AC-Stark shifts is considered the AC-Stark shift  $\Delta_{S,i,j}$ , belonging to the spin-flip measurement  $(i, j)$ . The four detunings  $\Delta_i$  are determined by measuring the absolute frequencies of the off-resonant laser  $\nu_i$ , and the resonance frequency  $\nu_{res}$ , the detuning being  $\Delta_i = \nu_i - \nu_{res}$ .

### A.2. Uncertainties and Corrections of the Measured Variables

In the following, statistical uncertainties, systematic uncertainties and systematic shifts are strictly distinguished. A statistical uncertainty of a given quantity is denoted by  $\epsilon(\cdot)$ , while a systematic uncertainty is denoted by  $\sigma(\cdot)$ . A systematic shift is denoted by  $\delta(\cdot)$ , and it is always accompanied by a systematic uncertainty. All shifts and

uncertainties are reported as *relative* quantities. Some uncertainties are found to be small as compared to the dominating ones, in this case an estimation of the magnitude is given, however these uncertainties are not quantitatively taken into account in the total uncertainty. If this is the case, it is explicitly stated in the corresponding section. As our total uncertainty is on the  $10^{-3}$  level, corrections and uncertainties below the  $10^{-4}$  level are not taken into account in the final uncertainty budget. In the cases where mean values  $\bar{\epsilon}, \bar{\sigma}$  are reported, these quantities result from averaging over all the individual uncertainties of each data set. These average values are only given as an quantitative overview for the reader, those mean values have not been used for the computation of the resulting total uncertainties, see sec. A.3 for details.

### A.2.1. Statistical Uncertainty of $\delta R$ and $b$

The individual standard uncertainties  $\epsilon(R_{\pm,i,j})$  and  $\epsilon(b_{i,j})$  of the values for  $R_{\pm,i,j}$  and  $b_{i,j}$  are extracted by marginalization of the data generated by the used Markov Chain Monte Carlo fitting algorithm.

$\epsilon(R_{\pm,i,j})$  and  $\epsilon(b_{i,j})$  are used to calculate the total uncertainty of  $\gamma_{PS}$ ,  $\mathcal{E}(\gamma_{PS})$ , and  $\epsilon(b_{i,j})$  affect the total uncertainties of  $\gamma_{PD}$  and  $\tau$ ,  $\mathcal{E}(\gamma_{PD})$  and  $\mathcal{E}(\tau)$  see section A.3. The means of the standard uncertainties of  $\delta R$  and  $b$ , taken over all data sets  $(i, j)$ , are given here to provide a quantitative overview. They read

$$\begin{aligned}\bar{\epsilon}(\delta R) &= 12.1 \times 10^{-3} \\ \bar{\epsilon}(b) &= 24.8 \times 10^{-3},\end{aligned}\tag{A.1}$$

where  $\delta R = R_+ - R_-$  is the differential spin-flip rate.

### A.2.2. Detuning $\Delta$

The detunings read  $\Delta_i = \nu_i - \nu_{res}$ , with  $\nu_{res}$  being the so far unknown resonance frequency of the transition. The precision of the detunings  $\Delta_i$  are given by the measurement precision of the absolute laser frequencies  $\nu_i$  of the four detuning values. These are measured by a commercial wavemeter. The resulting uncertainties have been quantified by determining the standard deviation of a time series of wavelength measurements of  $\nu_i$ . The wavemeter was calibrated and drift-monitored using a laser, which has a linewidth orders of magnitude smaller than that measured standard deviation. The uncertainties amount to:

$$\begin{aligned}
\epsilon_{wm}(\Delta_1) &= 0.4 \times 10^{-3} \\
\epsilon_{wm}(\Delta_2) &= 0.5 \times 10^{-3} \\
\epsilon_{wm}(\Delta_3) &= 0.6 \times 10^{-3} \\
\epsilon_{wm}(\Delta_4) &= 0.4 \times 10^{-3}
\end{aligned} \tag{A.2}$$

To determine the resonance frequency  $\nu_{res}$ , the fact, that the ratio of AC-Stark shift and differential spin-flip rate is proportional to the detuning can be made use of:

$$(-)\frac{1}{3}\frac{\Delta_{S,i,j}}{\delta R_{i,j}} \propto \Delta_i. \tag{A.3}$$

The minus sign holds for negative detunings. A linear regression of this quantity is performed with respect to the wavelength meter frequency  $\nu_i$  from which the zero-crossing  $\nu_{res}$ , i.e. the resonance frequency, is obtained. The accuracies of the detunings  $\Delta_i$  are limited by the accuracy of the linear regression used to determine the numerical value of  $\nu_{res}$ . As  $\nu_{res}$  is used to compute *all* detunings, it is a systematic uncertainty. The values are:

$$\begin{aligned}
\sigma_{fit}(\Delta_1) &= 1.5 \times 10^{-3} \\
\sigma_{fit}(\Delta_2) &= 1.8 \times 10^{-3} \\
\sigma_{fit}(\Delta_3) &= 1.8 \times 10^{-3} \\
\sigma_{fit}(\Delta_4) &= 1.6 \times 10^{-3}
\end{aligned} \tag{A.4}$$

### A.2.3. Residual Near-resonant Light at 397 nm

Two laser sources provide spurious residual light weakly driving the cycling transition.

- **Doppler Cooling Laser:** The laser used for Doppler cooling and fluorescence readout is switched by an acousto-optical modulator in double-pass configuration, see chapter 3.2. An estimate of the residual photon scattering rate due to imperfect switch-off is obtained by initializing the qubit in  $|\uparrow\rangle$  or  $|\downarrow\rangle$ , either before or after a 10 ms wait time before readout. This yields spurious spin-flip rates of  $R_-^{(res)} = 1.1(6)$  Hz and  $R_+^{(res)} = 0.7(4)$  Hz. These rates are taken into account for two of the acquired data sets, by modifying the model Eqs. 3.27, incorporating

the fact that these persist throughout the entire 1 ms interval. From fitting with the modified model, the obtained corrections are

$$\begin{aligned}\delta_{397}(\delta R) &= -4.1 \times 10^{-4} \\ \delta_{397}(b) &= -8.3 \times 10^{-4}\end{aligned}\tag{A.5}$$

and the systematic uncertainties read

$$\begin{aligned}\sigma_{397}(\delta R) &= 4.6 \times 10^{-4} \\ \sigma_{397}(b) &= 6.4 \times 10^{-4}.\end{aligned}\tag{A.6}$$

- Off-resonant Laser: The off-resonant light near 397 nm is obtained from an amplified, frequency doubled diode laser system, see chapter 3.2. The amplified fundamental beam seeding the doubler has a broad background of amplified spontaneous emission (ASE), extending over about 30 nm, equivalent to  $\delta_{amp} \approx 2\pi \times 57$  THz. The suppression with respect to the coherent light is specified to be  $\chi = -40$  dB. It is theoretically conceivable that this background leads to additional UV light near the atomic resonance, which would effectively shorten the measured lifetime. A pessimistic estimate of this effect is given here, assuming only  $\chi = -30$  dB ASE suppression, perfect phase-matching for sum-frequency generation (SFG) of ASE and laser mode photons, perfect AOM diffraction even for incoherent light and that a spurious component exactly hits the atomic resonance. With a SHG cavity linewidth of  $\delta_c = 2\pi \times 500$  kHz, the power ratio of the spurious to the main SHG component reads

$$\frac{P_{spur}}{P_{SHG}} \approx \chi \frac{\delta_c}{\delta_{amp}} \approx 9 \times 10^{-15}.\tag{A.7}$$

This strong suppression even under pessimistic assumptions leads us to the conclusion that this effect does not have to be taken into account. Still, an experimental verification has been performed, where the depolarization after initialization in  $|\downarrow\rangle$  was probed, at a fixed off-resonant pulse-time of 50  $\mu$ s, corresponding to about 20% depolarization. The laser frequency was scanned over a range of 1.3 GHz, which is more than one free spectral range of the SHG cavity. The scan speed is about 2 MHz/s, such that one data point integrates over about 4 MHz, which is slow enough to resolve the atomic line. No resonant features were observed in the resulting depolarization signal.

All in all, the effect is predicted to be orders of magnitudes too small to be relevant and could not be observed experimentally, so the respective uncertainties and shifts are neglected in the following.

#### A.2.4. Residual $\pi$ -polarized Off-resonant Light

The k-vector of the off-resonant light is aligned parallel to the magnetic field, so ideally only  $\sigma$ -transitions can be driven. Alignment errors of the beam might be the cause for residual  $\pi$ -polarized light, which is not accounted for in Eq. 3.17. Taking into account the additional scattering events and the pumping to the  $D_{3/2}$ -state caused by additional  $\pi$  polarized light, the rate equations Eqs. 3.17 are extended, including an additional parameter  $R_D$ :

$$\begin{aligned}\dot{p}_\uparrow &= -R_-(1+b)p_\uparrow - R_D p_\uparrow + R_+ p_\downarrow \\ \dot{p}_\downarrow &= -R_+(1+b)p_\downarrow - R_D p_\downarrow + R_- p_\uparrow.\end{aligned}\tag{A.8}$$

with

$$R_D = \frac{b}{2} \frac{\epsilon_0^2}{\epsilon_+^2} R_+.\tag{A.9}$$

The solutions of the rate equations are of the same form as for Eq. 3.17, however with altered coefficients

$$\bar{R} = (1+b)(R_- + R_+) + R_D\tag{A.10}$$

$$\tilde{R}^2 = \bar{R}^2 - 4(2+b)(R_D + bR_-)R_+.\tag{A.11}$$

If the data is now fitted using this modified model, values of about  $R_D = 3(3)$  Hz are obtained, and altered values for  $\delta R_{i,j}, b_{i,j}$  for all data sets  $(i, j)$ , which are used to calculate the total uncertainties of  $\gamma_{PD}$  and  $\tau$ ,  $\mathcal{E}(\gamma_{PD})$  and  $\mathcal{E}(\tau)$  see section A.3. From the difference with the unmodified model, the shifts and uncertainties for each detuning,  $\bar{\delta}_\pi(\delta R_i), \bar{\delta}_\pi(b_i), \bar{\sigma}_\pi(\delta R_i)$  and  $\bar{\sigma}_\pi(b_i)$  are extracted. Here, the mean value of the shifts  $\bar{\delta}_\pi(\delta R)$  and  $\bar{\delta}_\pi(b)$  and the accompanying uncertainties  $\bar{\sigma}_\pi(\delta R)$  and  $\bar{\sigma}_\pi(b)$  are given to provide a quantitative overview:

$$\begin{aligned}\bar{\delta}_\pi(\delta R) &= 3.3 \times 10^{-3} \\ \bar{\delta}_\pi(b) &= -2.4 \times 10^{-3},\end{aligned}\tag{A.12}$$

and the spread of the deviations within each data set determines the systematic uncertainties

$$\begin{aligned}\bar{\sigma}_\pi(\delta R) &= 2.9 \times 10^{-3} \\ \bar{\sigma}_\pi(b) &= 2.6 \times 10^{-3}\end{aligned}\tag{A.13}$$

### A.2.5. Differential AC-Stark Shift $\Delta_S$

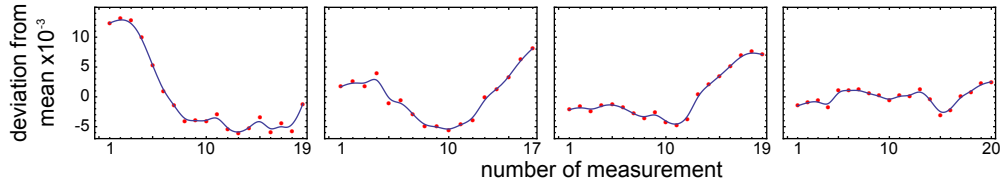


**Figure A.1.:** The red points depict the relative deviations of the AC-Stark shift values  $\Delta_{S,i,j}$  from their mean for all four measurement sessions. The blue curves are the B-spline functions defined by the points. The RMS deviation of the points from the spline is used as the statistical uncertainty.

The statistical uncertainty of fitting the Model Eq. 3.28 to the data taken in the spin-echo experiments is on the  $10^{-7}$  level, which is insignificant compared to other uncertainties. Systematic effects, i.e. temporal drifts, are clearly dominant.

$\Delta_{S,i,j}$  for each data set  $i, j$  is determined by the mean of two measurements, taken before and after the spin-flip rate measurement yielding  $\delta R_{i,j}$ . The drift of the AC-Stark shift over the measurement time for each detuning  $\Delta_i$  is slow and therefore mostly resolved, thus the assumption of a linear drift between two consecutive stark shift measurements is justified. To account for residual drifts on a timescale which is not resolved, the measured  $\Delta_S$  values are used as control points to define a B-spline function as shown in Fig. A.1. The RMS of the difference of the measurement result and the corresponding B-spline value is treated as the overall inaccuracy  $\epsilon(\Delta_{S,i,j})$  of all  $\Delta_S$  values pertaining to detuning  $\Delta_i$ . The mean value of those relative uncertainties reads

$$\bar{\epsilon}(\Delta_S) = 3.0 \times 10^{-4}\tag{A.14}$$

### A.2.6. Zeeman Shift

The Zeeman shifts of the atomic levels ( $\Delta_Z = 2\pi \times 13.34$  MHz splitting between  $|\uparrow\rangle$  and  $|\downarrow\rangle$ ) have not been taken into account. However, as the atomic resonance frequency is determined via the AC-Stark shift caused by the predominantly  $\sigma_+$  polarized beam,

the detuning  $\Delta$  specifically refers to the  $|S_{1/2}, m_J = -1/2\rangle \leftrightarrow |P_{1/2}, m_J = +1/2\rangle$  transition *including* its Zeeman shift. Corrections are only necessary for the transitions driven by the weak  $\sigma_-$  and  $\pi$  polarization components. The corresponding systematic uncertainties are estimated to be

$$\begin{aligned}\sigma_Z(\delta R) &\approx \frac{\epsilon_{0,-}^2}{\epsilon_+^2} \frac{\Delta_Z}{\Delta} \approx \frac{R_-}{R_+} \frac{\Delta_Z}{\Delta} \lesssim 3 \times 10^{-5} \\ \sigma_Z(\Delta_S) &\lesssim 2 \times 10^{-5}\end{aligned}\tag{A.15}$$

### A.2.7. Influence of Micromotion

Both the spin-flip rates  $R_+$ ,  $R_-$  and the AC-Stark shift  $\Delta_S$  are altered in the presence of micromotion along the propagation direction of the off-resonant beam. The micromotion causes effective frequency modulation (FM), characterized by the trap drive frequency  $\Omega_{rf} = 2\pi \times 25$  MHz and the modulation index  $\beta$ . The refined expressions read

$$R_{\pm}^{(mm)} \approx \gamma_{PS} \frac{\epsilon_{\pm}^2 + \epsilon_0^2}{9} \sum_{n=-\infty}^{+\infty} J_n^2(\beta) \frac{\Omega^2}{4(\Delta + n\Omega_{rf})^2}\tag{A.16}$$

$$\Delta_S^{(mm)} \approx \frac{\epsilon_+^2 - \epsilon_-^2}{3} \sum_{n=-\infty}^{+\infty} J_n^2(\beta) \frac{\Omega^2}{4(\Delta + n\Omega_{rf})}.\tag{A.17}$$

By measuring the the shape of the resonance fluorescence line by recording fluorescence photons at low power and across resonance, an upper bound for the modulation index of  $\beta = 3.5$  is obtained. Note that the micromotion-induced frequency modulation leads to symmetric FM sidebands, therefore the effects cancel out to first order. Due to the  $\Delta^{-1}(\Delta^{-2})$  scaling behavior of the AC-Stark shift (spin-flip rates), *both* quantities are slightly increased by FM components on the side towards the resonance, such that the total effect partially cancels out. Thus, an estimate for the systematic uncertainty of the resulting  $\gamma_{PS}$  rather than for  $\Delta_S$  and  $\delta R$  is given. Using realistic values of  $\Omega^2$ ,  $\epsilon_+^2$ ,  $\epsilon_-^2$  and  $\Delta$ , it reads

$$\sigma_{mm}(\gamma_{PS}) = \frac{1}{\delta R} \left( \delta R^{(mm)} - \delta R \right) - \frac{1}{\Delta_S} \left( \Delta_S^{(mm)} - \Delta_S \right) \approx 1.0 \times 10^{-4}\tag{A.18}$$

### A.2.8. Influence of Near-Resonance-Effects

The expressions for  $\delta R$  Eq. 3.12 and  $\Delta_S$  Eq. 3.20 are only valid if  $|\Delta| \gg \gamma_{PS}, \Omega$ . Our experimental conditions are  $\gamma_{PS}/|\Delta| \lesssim 5 \times 10^{-2}$ ,  $\Omega/|\Delta| \lesssim 4 \times 10^{-2}$ , and the influences of those approximations are quantified in the following.

The *measured*, i.e. actual spin-flip rate  $\delta R^{(meas)}$  is *smaller* than the far-off-resonance approximation Eq. 3.12. Using Eq. 2.22 instead of Eq. 2.23, where power broadening and the finite natural linewidth are included, the spin-flip rate is given by

$$\begin{aligned}\delta R^{(meas)} &= \gamma_{PS} \frac{\epsilon_+^2 - \epsilon_-^2}{9} \frac{\Omega^2}{4\Delta^2 + 2\Omega^2 + \gamma_{PS}^2} \\ &\approx \gamma_{PS} \frac{\epsilon_+^2 - \epsilon_-^2}{9} \Omega^2 \left( \frac{1}{4\Delta^2} - \frac{2\Omega^2 + \gamma_{PS}^2}{16\Delta^4} \right) \\ &= \delta R + \delta R',\end{aligned}\tag{A.19}$$

and thus

$$\delta R' = -\delta R \frac{2\Omega^2 + \gamma_{PS}^2}{4\Delta^2}\tag{A.20}$$

The correction is obtained by invoking the expression Eq. 3.12 for the decay rate  $\gamma_{PS}$ :

$$\begin{aligned}\gamma_{PS} &= \frac{3\Delta}{\Delta_S} (\delta R^{(meas)} - \delta R') \\ &= \frac{3\Delta}{\Delta_S} \delta R^{(meas)} (1 + \delta_{broad}(\delta R))\end{aligned}\tag{A.21}$$

such that

$$\delta_{broad}(\delta R) = -\frac{\delta R'}{\delta R^{(meas)}} \approx 2\Delta_S/\Delta\tag{A.22}$$

The numeric values read as follows:

$$\begin{aligned}\delta_{broad}(\delta R_1) &= 2.0 \times 10^{-4} \\ \delta_{broad}(\delta R_2) &= 2.6 \times 10^{-4} \\ \delta_{broad}(\delta R_3) &= 2.9 \times 10^{-4} \\ \delta_{broad}(\delta R_4) &= 2.1 \times 10^{-4}.\end{aligned}\tag{A.23}$$

For  $\Delta_S$ , no expression corresponding to Eq. A.19 is available, therefore values from a numerical simulation using a three-level generalized optical Bloch equation are extracted. For  $\delta_{broad}(\Delta_S) = (\Delta_S^{(meas)} - \Delta_S)/\Delta_S^{(meas)}$ , the values read



$$\begin{aligned}
\delta_{broad}(\Delta_{S,1}) &= 1.0 \times 10^{-4} \\
\delta_{broad}(\Delta_{S,2}) &= 1.4 \times 10^{-4} \\
\delta_{broad}(\Delta_{S,3}) &= 1.4 \times 10^{-4} \\
\delta_{broad}(\Delta_{S,4}) &= 1.0 \times 10^{-4}.
\end{aligned} \tag{A.24}$$

### A.2.9. Finite $D_{3/2}$ -lifetime and residual 866 nm repump light

In the model Eqs. 3.17, the lifetime of the metastable  $D_{3/2}$ -state is considered to be infinite, due to the dynamics of that model evolving on a much shorter timescale, than the long, but finite lifetime of that state of 1176(11) ms [Kre05]. Residual light near 866 nm also depletes population accumulated in the  $D_{3/2}$  state at a rate  $R_{dep}$ , effectively reducing its lifetime. The residual power in the imperfectly switched off beam has been measured using a fibre-coupled avalanche photodiode, to about 6 pW. In the switched-on state, the optical power is 86  $\mu$ W. For observing the amount of resonance fluorescence versus optical power at 866 nm, a saturation parameter of 23(5) is inferred. This leads to a saturation parameter in the switched-off state of  $S_{off}^{(866)} = 1.6(8) \times 10^{-6}$ . The depletion rate of the  $D_{3/2}$  state is then

$$R_{D3/2}^{(dep)} = \frac{\gamma_{PS}}{2} \frac{S_{off}^{(866)}}{1 + 4\bar{\delta}^2/\gamma_{PD}^2}. \tag{A.25}$$

Here,  $\bar{\delta}$  is the average detuning of the sub-transitions between the  $P_{1/2}$  and  $D_{3/2}$  manifolds, considering the Zeeman splitting (see Sec. A.2.6) and the repump laser to be tuned onto the blue side of the entire manifold. A laser induced depletion rate of 1.2(1.0) Hz was obtained. Thus, the  $D_{3/2}$  state is depleted at a total rate of about  $R_{D3/2}^{(dep)} = 2.2(1.0)$  Hz.

For estimating the impact of the depletion on the result for  $\delta R$ , the rate equations Eqs. 3.17 are modified to be

$$\begin{aligned}
\dot{p}_{\uparrow} &= -R_{-}(1+b) p_{\uparrow} + R_{+} p_{\downarrow} + \frac{1}{2} R_{D3/2}^{(dep)} (1 - p_{\uparrow} - p_{\downarrow}) \\
\dot{p}_{\downarrow} &= -R_{+}(1+b) p_{\downarrow} + R_{-} p_{\uparrow} + \frac{1}{2} R_{D3/2}^{(dep)} (1 - p_{\uparrow} - p_{\downarrow}).
\end{aligned} \tag{A.26}$$

Using these for example data in our fit procedure, the systematic shifts read

$$\begin{aligned}
\delta_{\gamma D3/2}(\delta R) &= 3.2 \times 10^{-4} \\
\delta_{\gamma D3/2}(b) &= 1.6 \times 10^{-3}
\end{aligned} \tag{A.27}$$

and systematic uncertainties

$$\begin{aligned}\sigma_{\gamma D3/2}(\delta R) &= 1.6 \times 10^{-4} \\ \sigma_{\gamma D3/2}(b) &= 7 \times 10^{-4}\end{aligned}\tag{A.28}$$

### A.2.10. Influence of the $P_{3/2}$ state

The  $P_{3/2}$  is separated from the  $P_{1/2}$  manifold by the fine-structure-splitting of  $\Delta_{FS} \approx 2\pi \times 6.69$  THz. The coupling strength  $\Omega^2$  is increased with respect to the  $P_{1/2}$  state by a factor of 2, given by the ration of the squared reduced dipole matrix elements, which is indicated explicitly. The presence of these levels affects both the AC-Stark shift and the spin-flip rates. For the latter, the decay rate is approximated to be the same as for the  $^2P_{1/2}$  state, and only the predominant  $\sigma_+$  polarization component is taken into account, and the decay into the  $D_{3/2}$  and  $D_{5/2}$  states is neglected. The additional spin-flip rate then reads:

$$R_+^{(P3/2)} \approx \gamma_{PS} \frac{2}{3} \frac{\epsilon_+^2}{6} \frac{2\Omega^2}{4(\Delta_{FS} - \Delta)^2} \approx \gamma_{PS} \frac{1}{9} \frac{2\Omega^2}{4\Delta_{FS}^2}\tag{A.29}$$

Note that the for the  $P_{3/2}$  state, due to the different Clebsch-Gordan coefficients, the branching ratio of decays with spin-flip to decay without spin-flip is reversed with respect to the  $P_{1/2}$  state, however the spin-flip rate has the same prefactor as in Eq. 3.12. The excitation channel  $S_{1/2}, m_J = +1/2 \rightarrow P_{3/2}, m_J = +3/2$  contributes only to elastic scattering. Interference effects between different pathways do not play a role as the emitted photons are distinguishable either by wavelength or by polarization/emission direction.

For the AC-Stark shift, the correction reads:

$$\Delta_S^{(P3/2)} \approx \left( \frac{\epsilon_+^2}{2} - \frac{\epsilon_+^2}{6} \right) \frac{2\Omega^2}{4(\Delta_{FS} - \Delta)} \approx \frac{\epsilon_+^2}{3} \frac{2\Omega^2}{4\Delta_{FS}}\tag{A.30}$$

For the  $P_{3/2}$  state, the transition  $S_{1/2}, m_J = +1/2 \rightarrow P_{3/2}, m_J = +3/2$  contributes to the differential AC-Stark shift and has a larger Clebsch-Gordan coefficient than the transition  $S_{1/2}, m_J = -1/2 \rightarrow P_{3/2}, m_J = +1/2$ . The reversed sign has to be accounted for as only measure absolute values of  $\Delta_S$  have been measured. For  $\Delta > 0$ , the magnitude of  $\Delta_S$  is increased, for  $\Delta < 0$  it is decreased.

The respective shifts read

$$\delta_{P3/2}(\Delta_{S,i}) = \frac{\Delta_i}{3\Delta_{FS}} \approx 1.0 \times 10^{-3} \frac{\Delta_i}{2\pi \times 10 \text{ GHz}}\tag{A.31}$$

$$\delta_{P3/2}(\delta R_i) = \frac{\Delta_i^2}{3\Delta_{FS}^2} \approx 1.5 \times 10^{-6} \left( \frac{\Delta_i}{2\pi \times 10 \text{ GHz}} \right)^2\tag{A.32}$$

Note that the  $\delta_{P3/2}(\Delta_{S,i,j})$  depend on the sign of  $\Delta_i$ . Due to its small magnitude,  $\delta_{P3/2}(\delta R_{i,j})$  is neglected from hereon. Systematic uncertainties are not included here as well due to the small magnitudes of these corrections

#### A.2.11. Fit bias

Parameter estimation from measurement data might be affected by a systematic bias, depending on the used estimator. Artificial measurement data has been created from the model Eq. 3.17 with fixed values of  $R_{\pm}, b$  with binomial uncertainty. It shows, that for an increasing number of measurements, i.e. vanishing noise, the fit results for  $R_{\pm}, b$  converge to the preset values. No bias is therefore taken into account in our uncertainty budget.

#### A.2.12. SPAM uncertainties

For the determination of the differential spin-flip rate  $\delta R$ , SPAM uncertainties are taken into account in the model from Eq. 3.27 for the parameter estimation. The uncertainty of the additional parameters and their cross-correlation with  $R_{\pm}, b$  is already taken into account, as the statistical uncertainties  $\epsilon(\delta R)$  and  $\epsilon(b)$  are obtained by marginalizing over the sample data from the Monte Carlo parameter estimation algorithm.

### A.3. Total uncertainties and corrections of $\gamma_{PS}, \gamma_{PD}$ and $\tau$

The uncorrected values for  $\gamma_{PS}$  for each detuning  $\Delta_i$  are obtained from averaging:

$$\begin{aligned}\gamma'_{PS,i} &= \frac{1}{N_i} \sum_{j=1}^{N_i} 3\Delta_i \frac{\delta R_{i,j}}{\Delta_{S,i,j}} \\ b'_i &= \frac{1}{N_i} \sum_{j=1}^{N_i} b_{i,j}\end{aligned}\tag{A.33}$$

The corrected values are obtained by adding all relative corrections:

$$\begin{aligned}\gamma_{PS,i}/\gamma'_{PS,i} &= 1 + \delta_{397}(\delta R) + \delta_{broad}(\delta R_i) + \delta_{\gamma_{D3/2}}(\delta R) + \delta_{\pi}(\delta R_i) \\ &\quad - \delta_{broad}(\Delta_{S,i}) - \delta_{P3/2}(\Delta_{S,i}) \\ b_i/b'_i &= 1 + \delta_{397}(b) + \delta_{\gamma_{D3/2}}(b) + \delta_{\pi}(b_i)\end{aligned}\tag{A.34}$$

The statistical uncertainties are obtained from uncertainty propagation:

$$\begin{aligned}\epsilon(\gamma_{PS,i,j})^2 &= \epsilon(\Delta_i)^2 + \epsilon(\Delta_{S,i,j})^2 + \epsilon(\delta R_{i,j})^2 \\ \epsilon(b_i)^2 &= \frac{1}{N_i^2} \sum_{j=1}^{N_i} \epsilon(b_{i,j})^2\end{aligned}\tag{A.35}$$

When taking the systematic uncertainties into account, problem occurs, that most of their correlations are not quantitatively available. However, it can be reasoned that they are due to well-distinguished physical effects and thus influence the resulting quantities in ways which are hardly related to each other. According to JCGM guidelines [Joi08], possible correlations are neglected and added in quadrature:

$$\begin{aligned}\sigma(\gamma_{PS,i})^2 &= \sigma_{mm}(\gamma_{PS})^2 + \sigma_{fit}(\Delta_i)^2 + \sigma_{397}(\delta R)^2 + \sigma_{\gamma_{D3/2}}(\delta R)^2 + \sigma_{\pi}(\delta R_i)^2 \\ \sigma(b_i)^2 &= \sigma_{397}(b)^2 + \sigma_{\gamma_{D3/2}}(b)^2 + \sigma_{\pi}(b_i)^2\end{aligned}\tag{A.36}$$

The final values are obtained by a weighted average over the four results:

$$\begin{aligned}\gamma_{PS} &= \frac{1}{\sum_i N_i} \sum_i N_i \gamma_{PS,i} \\ b &= \frac{1}{\sum_i N_i} \sum_i N_i b'_i\end{aligned}\tag{A.37}$$

The total statistical uncertainties are given by

$$\begin{aligned}\epsilon(\gamma_{PS})^2 &= \frac{1}{(\sum_i N_i)^2} \sum_{i,j} \epsilon(\gamma_{PS,i,j})^2 \\ \epsilon(b)^2 &= \frac{1}{(\sum_i N_i)^2} \sum_i N_i^2 \epsilon(b_i)^2.\end{aligned}\tag{A.38}$$

For the total systematic uncertainties, complete correlation between experiments at different detunings are assumed and averaged linearly:

$$\begin{aligned}\sigma(\gamma_{PS}) &= \frac{1}{\sum_i N_i} \sum_i N_i \sigma(\gamma_{PS,i}) \\ \sigma(b) &= \frac{1}{\sum_i N_i} \sum_i N_i \sigma(b_i),\end{aligned}\tag{A.39}$$

The total measurement uncertainties result from adding statistical and systematic uncertainties in quadrature:

$$\begin{aligned}\mathcal{E}(\gamma_{PS})^2 &= \epsilon(\gamma_{PS})^2 + \sigma(\gamma_{PS})^2 \\ \mathcal{E}(b)^2 &= \epsilon(b)^2 + \sigma(b)^2\end{aligned}\tag{A.40}$$

For the radiative decay rate to the  $D_{3/2}$  state,  $\gamma_{PD} = (b/3)\gamma_{PS}$  follows

$$\mathcal{E}(\gamma_{PD})^2 = \epsilon(b)^2 + \epsilon(\gamma_{PS})^2 + \sigma(b)^2 + \sigma(\gamma_{PS})^2\tag{A.41}$$

and correspondingly the total lifetime reads  $\tau = 1/(\gamma_{PS} + \gamma_{PD})$ :

$$\mathcal{E}(\tau)^2 = \epsilon(\gamma_{PS})^2 + \sigma(\gamma_{PS})^2 + \frac{b^2}{(3+b)^2} (\epsilon(b)^2 + \sigma(b)^2).\tag{A.42}$$



## B. Drawings of the Light-Ion Interface Trap

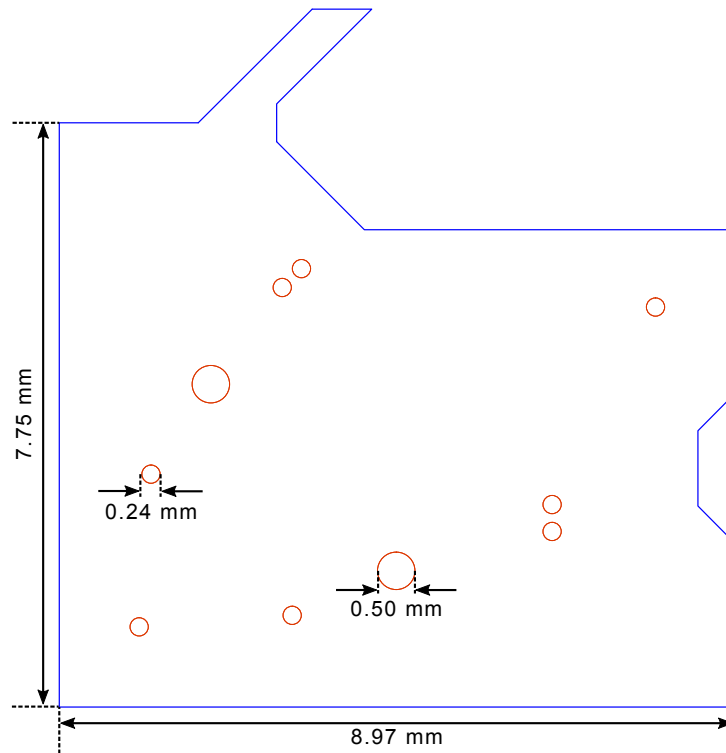
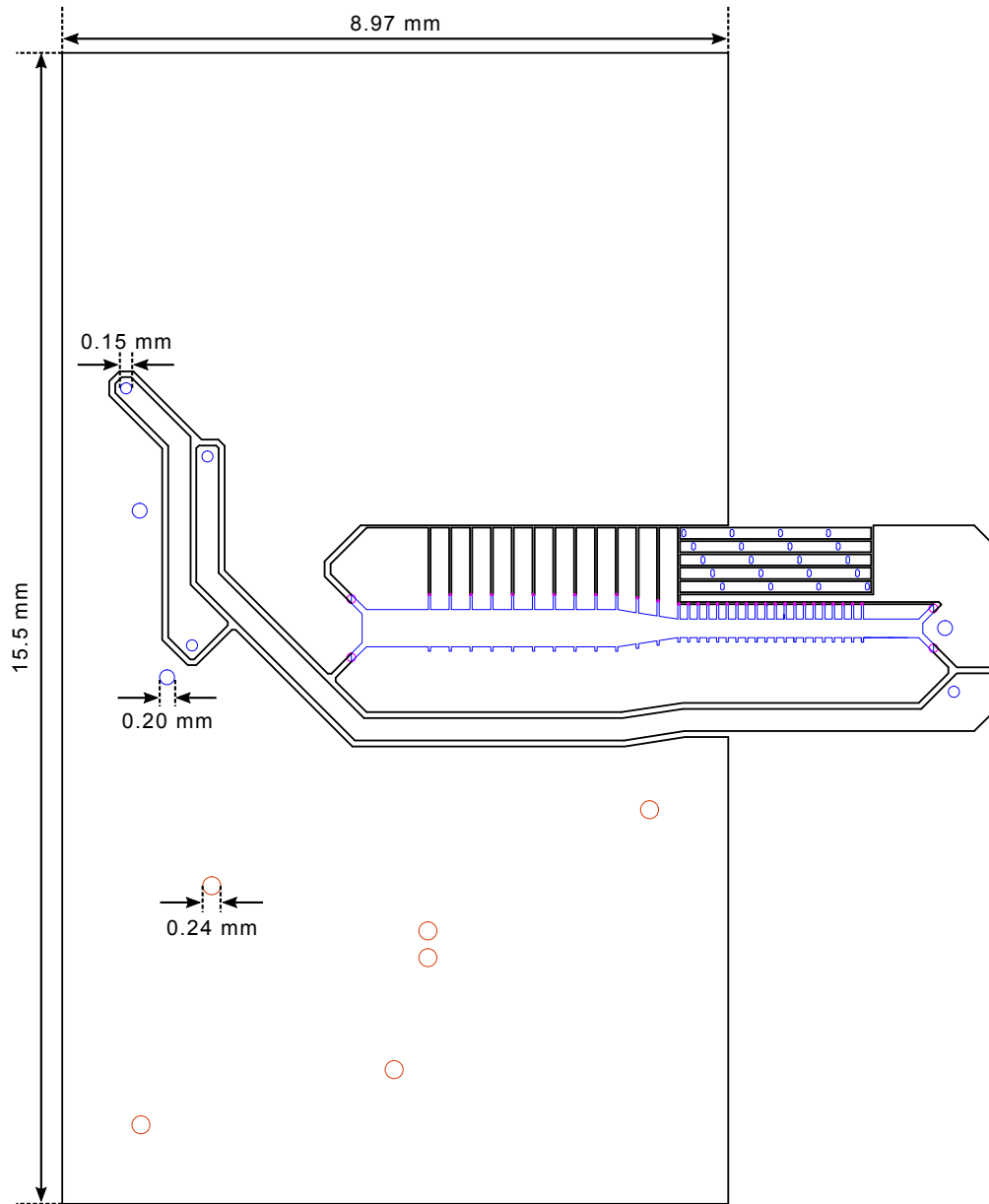


Figure B.1.: Spacer



**Figure B.2.:** Bottomlayer, backside





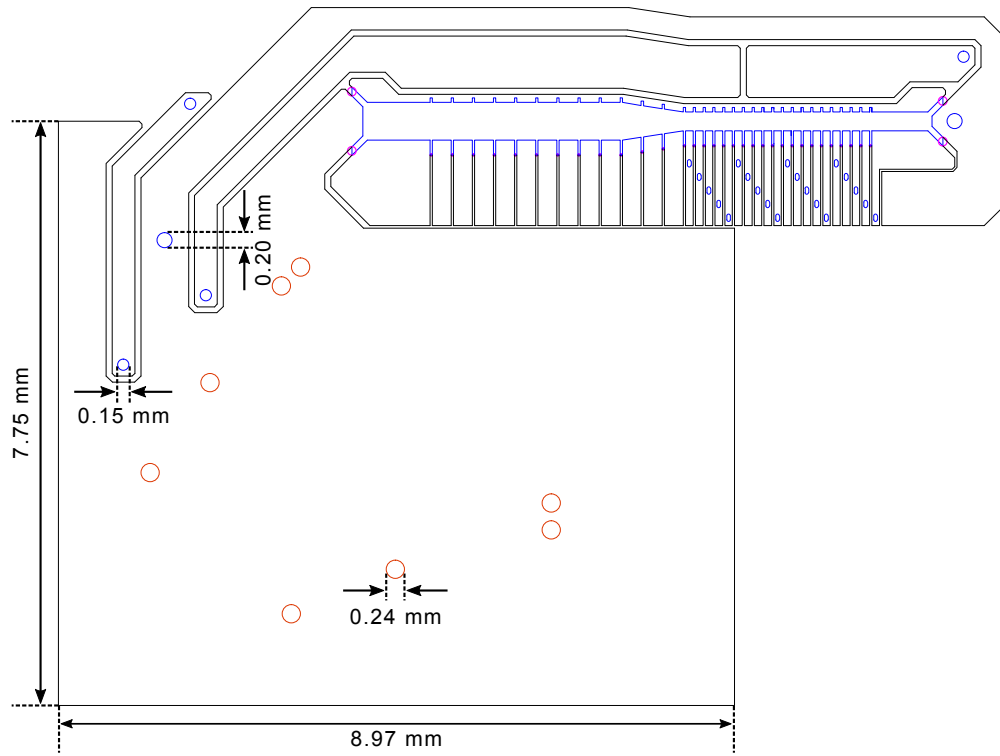


**Figure B.4.:** Toplayer, backside

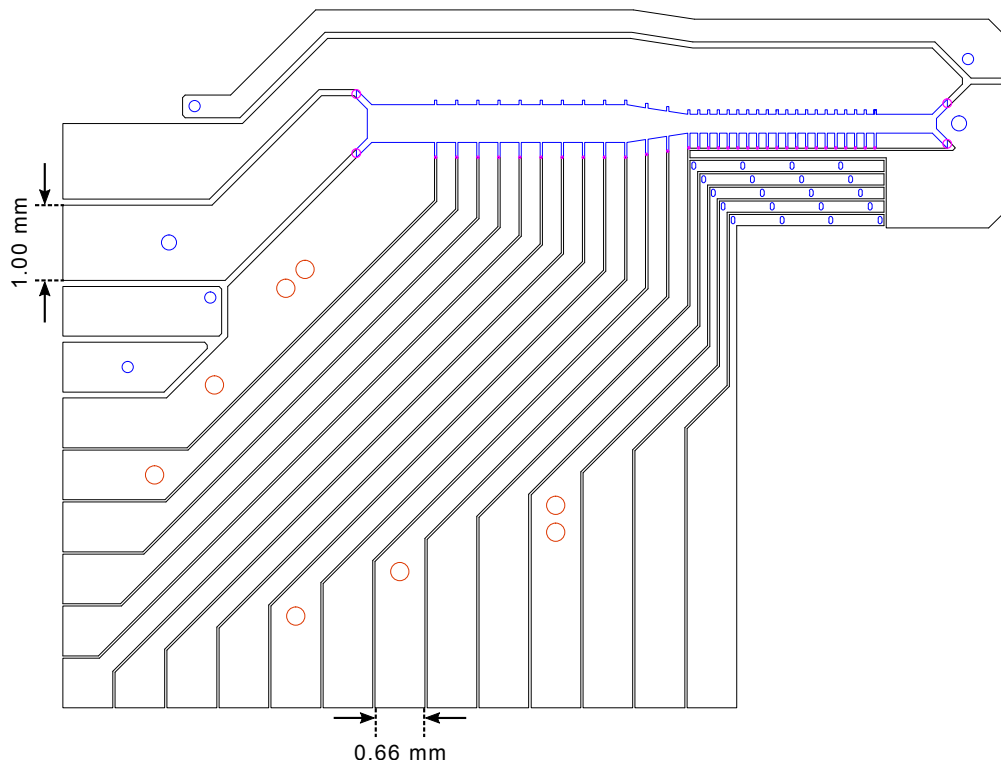


Figure B.5.: Toplayer, frontside

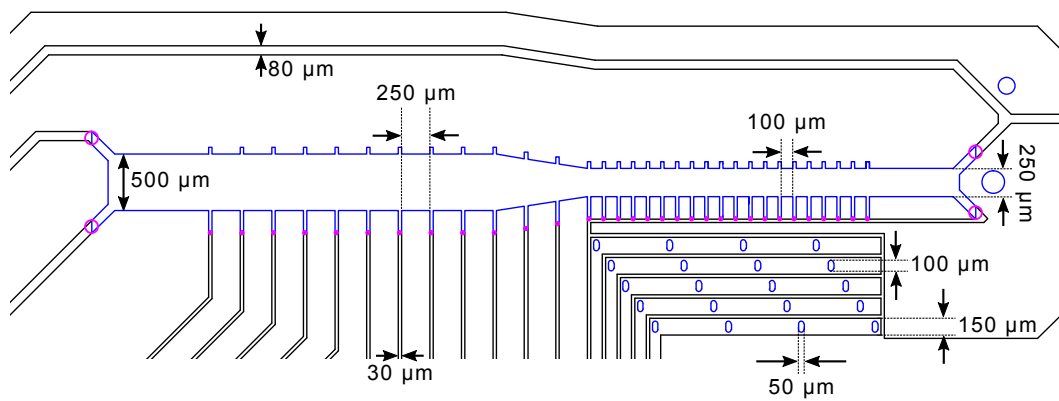
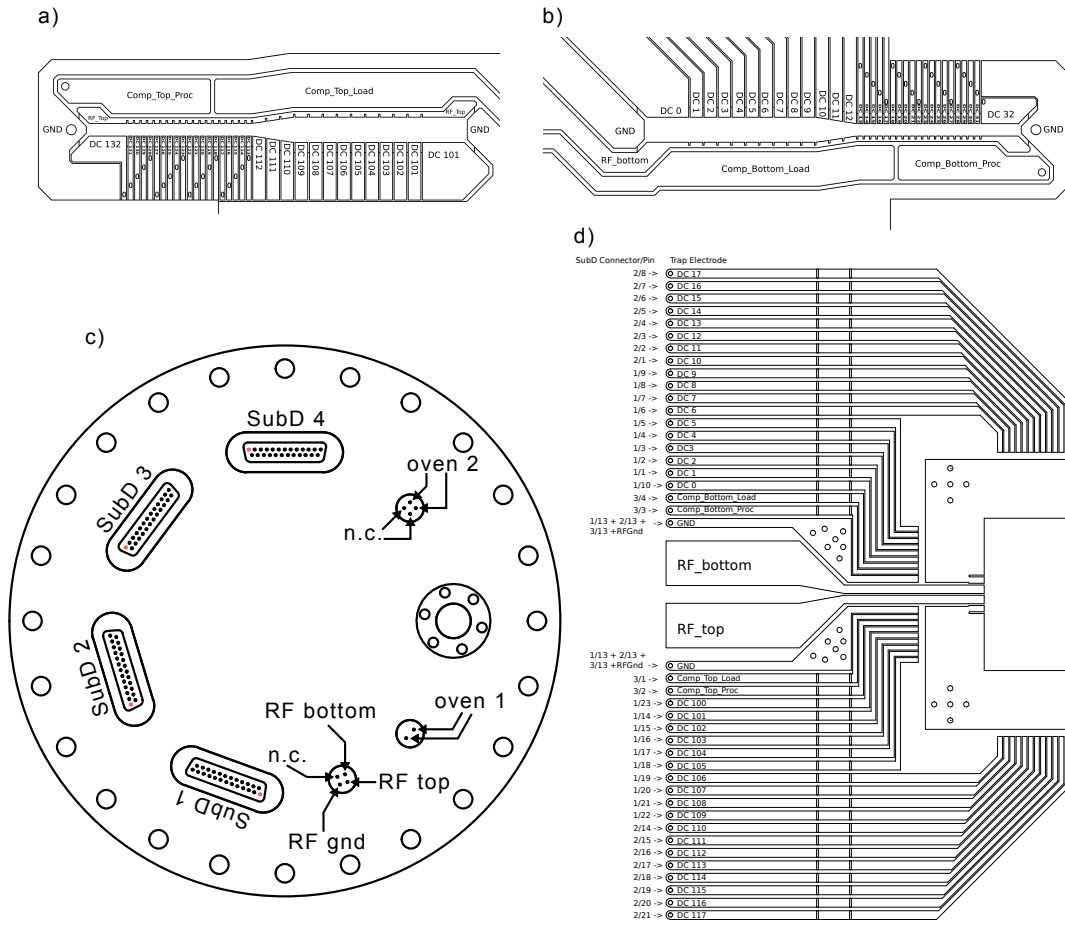


Figure B.6.: Toplayer, frontside, detail of electrode region



## C. Mappings of electrical connections



**Figure C.1.:** Electrode labels of a) top layer and b) bottom layer of the fibertrap. c) Top view of the fibertrap setup vacuum vessel's top flange. Electrical connections are provided by the depicted feedthroughs. d) Depiction of filterboard connections to UHV-feedthroughs.



## D. List of Publications

### Publications discussed in this thesis

- *A quantum repeater node with trapped ions: a realistic case example*  
A. D. Pfister, M. Salz, **M. Hettrich**, U. G. Poschinger, F. Schmidt-Kaler  
Applied Physics B **122**, 89 (2016)
- *Measurement of Dipole Matrix Elements with a Single Trapped Ion*  
**M. Hettrich**, T. Ruster, H. Kaufmann, C. F. Roos, C. T. Schmiegelow,  
F. Schmidt-Kaler, U. G. Poschinger  
Physical Review Letters **115**, 143003 (2015)

### Further publications

- *Phase-Stable Free-Space Optical Lattices for Trapped Ions*  
C. T. Schmiegelow, H. Kaufmann, T. Ruster, J. Schulz, V. Kaushal,  
**M. Hettrich**, F. Schmidt-Kaler, and U. G. Poschinger  
Physical Review Letters **116**, 033002 (2016)
- *Experimental realization of fast ion separation in segmented Paul traps*  
T. Ruster, C. Warschburger, H. Kaufmann, C. T. Schmiegelow, A. Walther,  
**M. Hettrich**, A. Pfister, V. Kaushal, F. Schmidt-Kaler, and U. G. Poschinger  
Physical Review A **90**, 033410 (2014)
- *Controlling Fast Transport of Cold Trapped Ions*  
A. Walther, F. Ziesel, T. Ruster, S. T. Dawkins, K. Ott, **M. Hettrich**, K. Singer,  
F. Schmidt-Kaler, and U. Poschinger  
Physical Review Letters **109**, 080501 (2012)

#### D. List of Publications

---

- *Interaction of a laser with a qubit in thermal motion and its application to robust and efficient readout*  
U. Poschinger, A. Walther, **M. Hettrich**, F. Ziesel, F. Schmidt-Kaler  
Applied Physics B **107**, 1159 (2012)
- *Single ion as a shot-noise-limited magnetic-field-gradient probe*  
A. Walther, U. Poschinger, F. Ziesel, **M. Hettrich**, A. Wiens, J. Welzel,  
and F. Schmidt-Kaler  
Physical Review A **83**, 062329 (2011)



# Bibliography

- [All75] L. Allen and J. H. Eberly, *Optical Resonance and Two-Level Atoms*, John Wiley & Sons, 1975.
- [Alo16] J. Alonso, F. M. Leupold, Z. U. Soler, M. Fadel, M. Marinelli, B. C. Keitch, V. Negnevitsky, and J. P. Home, *Generation of large coherent states by bang-bang control of a trapped-ion oscillator*, Nat Comms **7**, 11243 (2016).
- [Ami10] J. M. Amini, H. Uys, J. H. Wesenberg, S. Seidelin, J. Britton, J. J. Bollinger, D. Leibfried, C. Ospelkaus, A. P. VanDevender, and D. J. Wineland, *Toward scalable ion traps for quantum information processing*, New J. Phys. **12**, 033031 (2010).
- [And70] T. Andersen, J. Desesquelles, K. A. Jessen, and G. Sørensen, *Measurements of atomic lifetimes for neutral and ionized magnesium and calcium*, J. Quant. Spectrosc. Radiat. Transfer **10**, 1143 (1970).
- [Ans85] W. Ansbacher, A. S. Inamdar, and E. H. Pinnington, *Pulsed laser measurements of the lifetimes of the 4p levels of Ca II*, Phys. Lett. **110A**, 383 (1985).
- [Aro07] B. Arora, M. S. Safronova, and C. W. Clark, *Blackbody-radiation shift in a  $^{43}\text{Ca}^+$  ion optical frequency standard*, Phys. Rev. A **76**, 064501 (2007).
- [Bar04] M. D. Barrett, J. Chiaverini, T. Schaetz, J. Britton, W. M. Itano, J. D. Jost, E. Knill, C. Langer, D. Leibfried, R. Ozeri, and et al., *Deterministic quantum teleportation of atomic qubits*, Nature **429**, 737 (2004).
- [Bas78] S. Bashkin and J. O. Stoner, *Atomic Energy-Level and Grotrian Diagrams, Vol II*, North Holland, 1978.
- [Bel14] K. Beloy, N. Hinkley, N. B. Phillips, J. A. Sherman, M. Schioppo, J. Lehman, A. Feldman, L. M. Hanssen, C. W. Oates, and A. D. Ludlow, *Atomic Clock with  $1 \times 10^{-18}$  Room-Temperature Blackbody Stark Uncertainty*, Phys. Rev. Lett. **113**, 260801 (2014).

- [Bla01] E. D. Black, *An introduction to Pound-Drever-Hall laser frequency stabilization*, American Journal of Physics **69**, 79 (2001).
- [Blo14] B. J. Bloom, T. L. Nicholson, J. R. Williams, S. L. Campbell, M. Bishof, X. Zhang, W. Zhang, S. L. Bromley, and J. Ye, *An optical lattice clock with accuracy and stability at the  $10^{-18}$  level*, Nature **506**, 71 (2014).
- [Bow12] R. Bowler, J. Gaebler, Y. Lin, T. R. Tan, D. Hanneke, J. D. Jost, J. P. Home, D. Leibfried, and D. J. Wineland, *Coherent Diabatic Ion Transport and Separation in a Multizone Trap Array*, Physical Review Letters **109**, 080502 (2012).
- [Bra92] B. Bransden and C. J. Joachain, *Physics of Atoms and Molecules*, Longman Scientific & Technical, 1992.
- [Bra13] B. Brandstaätter, A. McClung, K. Schüppert, B. Casabone, K. Friebe, A. Stute, P. O. Schmidt, C. Deutsch, J. Reichel, R. Blatt, and T. E. Northup, *Integrated fiber-mirror ion trap for strong ion-cavity coupling*, Review of Scientific Instruments **84**, 123104 (2013).
- [Bri05] K.-A. Brickman, P. C. Haljan, P. J. Lee, M. Acton, L. Deslauriers, and C. Monroe, *Implementation of Grover's quantum search algorithm in a scalable system*, Physical Review A **72**, 050306 (2005).
- [Bro86] L. S. Brown and G. Gabrielse, *Geonium theory: Physics of a single electron or ion in a Penning trap*, Rev. Mod. Phys. **58**, 233 (1986).
- [Bro15] M. Brownnutt, M. Kumph, P. Rabl, and R. Blatt, *Ion-trap measurements of electric-field noise near surfaces*, Rev. Mod. Phys. **87**, 1419 (2015).
- [Bud08] D. Budker, D. F. Kimball, and D. P. DeMille, *Atomic Physics - An Exploration through Problems and Solutions*, Oxford University Press, 2008.
- [Car54] H. Y. Carr and E. M. Purcell, *Effects of Diffusion on Free Precession in Nuclear Magnetic Resonance Experiments*, Physical Review **94**, 630 (1954).
- [Car12] M. Carlsson and J. Leenaarts, *Approximations for radiative cooling and heating in the solar chromosphere*, A&A **539**, A39 (2012).
- [Chw09] M. Chwalla, J. Benhelm, K. Kim, G. Kirchmair, T. Monz, M. Riebe, P. Schindler, A. S. Villar, W. Hänsel, C. F. Roos, R. Blatt, M. Abgrall, G. Santarelli, G. D. Rovera, and P. Laurent, *Absolute Frequency Measurement of the  $^{40}\text{Ca}^+$   $4s^2S_{1/2} - 3d^2D_{5/2}$  Clock Transition*, Phys. Rev. Lett. **102**, 023002 (2009).

- 
- [Col07] Y. Colombe, T. Steinmetz, G. Dubois, F. Linke, D. Hunger, and J. Reichel, *Strong atom-field coupling for Bose-Einstein condensates in an optical cavity on a chip*, *Nature* **450**, 272 (2007).
- [CT04] C. Cohen-Tannoudji, J. Dupont-Roc, and G. Grynberg, *Atom-Photon Interactions*, Wiley-VCH, 2004.
- [Deu85] D. Deutsch, *Quantum Theory, the Church-Turing Principle and the Universal Quantum Computer*, *Proceedings of the Royal Society A: Mathematical, Physical and Engineering Sciences* **400**, 97 (1985).
- [Die89] F. Diedrich, J. C. Bergquist, W. M. Itano, and D. J. Wineland, *Laser Cooling to the Zero-Point Energy of Motion*, *Physical Review Letters* **62**, 403 (1989).
- [Dir27] P. A. M. Dirac, *The Quantum Theory of the Emission and Absorption of Radiation*, *Proceedings of the Royal Society A: Mathematical, Physical and Engineering Sciences* **114**, 243 (1927).
- [DiV96] D. DiVincenzo, *Topics in Quantum Computers*, arXiv:cond-mat/9612126 (1996).
- [Dre83] R. W. P. Drever, J. L. Hall, F. V. Kowalski, J. Hough, G. M. Ford, A. J. Munley, and H. Ward, *Laser phase and frequency stabilization using an optical resonator*, *Appl. Phys. B* **31**, 97 (1983).
- [Dub13] P. Dubé, A. A. Madej, Z. Zhou, and J. E. Bernard, *Evaluation of systematic shifts of the  $^{88}\text{Sr}^+$  single-ion optical frequency standard at the  $10^{-17}$  level*, *Phys. Rev. A* **87**, 023806 (2013).
- [Dub14] P. Dubé, A. A. Madej, M. Tibbo, and J. E. Bernard, *High-Accuracy Measurement of the Differential Scalar Polarizability of a  $^{88}\text{Sr}^+$  Clock Using the Time-Dilation Effect*, *Phys. Rev. Lett.* **112**, 173002 (2014).
- [Dut07] M. V. G. Dutt, L. Childress, L. Jiang, E. Togan, J. Maze, F. Jelezko, A. S. Zibrov, P. R. Hemmer, and M. D. Lukin, *Quantum Register Based on Individual Electronic and Nuclear Spin Qubits in Diamond*, *Science* **316**, 1312 (2007).
- [Esc03] J. Eschner, G. Morigi, F. Schmidt-Kaler, and R. Blatt, *Laser cooling of trapped ions*, *J. Opt. Soc. Am. B* **20**, 1003 (2003).
- [Fey82] R. P. Feynman, *Simulating physics with computers*, *Int J Theor Phys* **21**, 467 (1982).

- [Fox06] M. Fox, *Quantum Optics: An Introduction*, Oxford Master Series in Physics, OUP Oxford, 2006.
- [Gal16] J. Gallego, S. Ghosh, S. K. Alavi, W. Alt, M. Martinez-Dorantes, D. Meschede, and L. Ratschbacher, *High-finesse fiber Fabry-Perot cavities: stabilization and mode matching analysis*, Appl. Phys. B **122**, 47 (2016).
- [Geb15] F. Gebert, Y. Wan, F. Wolf, C. N. Angstmann, J. C. Berengut, and P. O. Schmidt, *Precision Isotope Shift Measurements in Calcium Ions Using Quantum Logic Detection Schemes*, Physical Review Letters **115**, 053003 (2015).
- [Ger10] R. Gerritsma, G. Kirchmair, F. Zähringer, E. Solano, R. Blatt, and C. F. Roos, *Quantum simulation of the Dirac equation*, Nature **463**, 68 (2010).
- [Gos88a] R. N. Gosselin, E. H. Pinnington, and W. Ansbacher, *Measurement of the lifetimes of the  $4p$  levels in  $\text{Ca II}$  using laser excitation of a fast beam*, Phys. Rev. A **38**, 4887 (1988).
- [Gos88b] R. N. Gosselin, E. H. Pinnington, and W. Ansbacher, *Precision lifetime measurement of levels of  $\text{Ti}^+$ ,  $\text{Ca}^+$  and  $\text{Na}^+$  using laser excitation of a fast ion beam*, Nuc. Inst. Meth. B **31**, 305 (1988).
- [Gre97] L. Greengard and V. Rokhlin, *A new version of the Fast Multipole Method for the Laplace equation in three dimensions*, Acta Numerica **6**, 229 (1997).
- [Gue91] C. Guet and W. R. Johnson, *Relativistic many-body calculations of transition rates for  $\text{Ca}^+$ ,  $\text{Sr}^+$ , and  $\text{Ba}^+$* , Phys. Rev. A **44**, 1531 (1991).
- [Gul01] S. Gulde, D. Rotter, P. Barton, F. Schmidt-Kaler, R. Blatt, and W. Hoyer-vorst, *Simple and efficient photo-ionization loading of ions for precision ion-trapping experiments*, Appl Phys B **73**, 861 (2001).
- [Gul03] S. Gulde, M. Riebe, G. P. T. Lancaster, C. Becher, J. Eschner, H. Häffner, F. Schmidt-Kaler, I. L. Chuang, and R. Blatt, *Implementation of the Deutsch-Jozsa algorithm on an ion-trap quantum computer*, Nature **421**, 48 (2003).
- [Gut01] G. R. Guthöhrlein, M. Keller, K. Hayasaka, W. Lange, and H. Walther, *A single ion as a nanoscopic probe of an optical field*, Nature **414**, 49 (2001).
- [Häf03] H. Häffner, S. Gulde, M. Riebe, G. Lancaster, C. Becher, J. Eschner, F. Schmidt-Kaler, and R. Blatt, *Precision Measurement and Compensation of Optical Stark Shifts for an Ion-Trap Quantum Processor*, Phys. Rev. Lett. **90**, 143602 (2003).

- 
- [Häf08] H. Häffner, C. Roos, and R. Blatt, *Quantum computing with trapped ions*, Physics Reports **469**, 155 (2008).
- [Hah50] E. L. Hahn, *Spin Echoes*, Physical Review **80**, 580 (1950).
- [Hän75] T. Hänsch and A. Schawlow, *Cooling of gases by laser radiation*, Optics Communications **13**, 68 (1975).
- [Hän99] T. W. Hänsch and H. Walther, *Laser spectroscopy and quantum optics*, Review of Modern Physics (1999).
- [Har04] J. Hartmann, *Investigations on the spectrum and orbit of  $\delta$  orionis*, Astrophysical Journal **19**, 268 (1904).
- [Har06] S. Haroche and J.-M. Raimond, *Exploring the Quantum*, Oxford University Press, 2006.
- [Har10] M. Harlander, M. Brownnutt, W. Hänsel, and R. Blatt, *Trapped-ion probing of light-induced charging effects on dielectrics*, New J. Phys. **12**, 093035 (2010).
- [Har11] M. Harlander, R. Lechner, M. Brownnutt, R. Blatt, and W. Hänsel, *Trapped-ion antennae for the transmission of quantum information*, Nature **471**, 200 (2011).
- [Har12] M. J. Harlander, *Architecture for a scalable ion-trap quantum computer*, Ph.D. thesis, Leopold-Franzens-Universität Innsbruck (2012).
- [Her09] P. F. Herskind, A. Dantan, J. P. Marler, M. Albert, and M. Drewsen, *Realization of collective strong coupling with ion Coulomb crystals in an optical cavity*, Nature Physics **5**, 494 (2009).
- [Het15] M. Hettrich, T. Ruster, H. Kaufmann, C. F. Roos, C. T. Schmiegelow, F. Schmidt-Kaler, and U. G. Poschinger, *Measurement of Dipole Matrix Elements with a Single Trapped Ion*, Physical Review Letters **115**, 143003 (2015).
- [Hun10] D. Hunger, T. Steinmetz, Y. Colombe, C. Deutsch, T. W. Hänsch, and J. Reichel, *A fiber Fabry-Perot cavity with high finesse*, New J. Phys. **12**, 065038 (2010).
- [Jac16] G. Jacob, K. Groot-Berning, S. Wolf, S. Ulm, L. Couturier, S. T. Dawkins, U. G. Poschinger, F. Schmidt-Kaler, and K. Singer, *Microscopy with a Deterministic Single Ion Source*, arXiv:1512.00347 (2016).
- [Jay63] E. Jaynes and F. Cummings, *Comparison of quantum and semiclassical radiation theories with application to the beam maser*, Proc. IEEE **51**, 89 (1963).

- [Jel04] F. Jelezko, T. Gaebel, I. Popa, A. Gruber, and J. Wrachtrup, *Observation of Coherent Oscillations in a Single Electron Spin*, Physical Review Letters **92**, 076401 (2004).
- [Jin93] J. Jin and D. A. Church, *Precision lifetimes for the  $\text{Ca}^+ 4p^2 P$  levels: Experiment challenges theory at the 1level*, Phys. Rev. Lett. **70**, 3213 (1993).
- [Joh09] M. Johanning, A. Braun, N. Timoney, V. Elman, W. Neuhauser, and C. Wunderlich, *Individual Addressing of Trapped Ions and Coupling of Motional and Spin States Using rf Radiation*, Physical Review Letters **102**, 073004 (2009).
- [Joi08] Joint Committee for Guides in Metrology, *Guide to the Expression of Uncertainty in Measurement*, Bureau International des Poids et Mesures, 2008.
- [Kau12] D. Kaufmann, T. Collath, M. T. Baig, P. Kaufmann, E. Asenwar, M. Johanning, and C. Wunderlich, *Thick-film technology for ultra high vacuum interfaces of micro-structured traps*, Appl. Phys. B **107**, 935 (2012).
- [Kau14] H. Kaufmann, T. Ruster, C. T. Schmiegelow, F. Schmidt-Kaler, and U. G. Poschinger, *Dynamics and control of fast ion crystal splitting in segmented Paul traps*, New J. Phys. **16**, 073012 (2014).
- [Kie02] D. Kielpinski, C. Monroe, and D. J. Wineland, *Architecture for a large-scale ion-trap quantum computer*, Nature **417**, 709 (2002).
- [Kie14] D. Kienzler, H.-Y. Lo, B. Keitch, L. de Clercq, F. Leupold, F. Lindenfesler, M. Marinelli, V. Negnevitsky, and J. P. Home, *Quantum harmonic oscillator state synthesis by reservoir engineering*, Science **347**, 53 (2014).
- [Kie15] D. Kienzler, *Quantum Harmonic Oscillator State Synthesis by Reservoir Engineering*, Ph.D. thesis, ETH Zürich (2015).
- [Kim98] H. J. Kimble, *Strong interactions of single atoms and photons in cavity QED*, Physica Scripta **T76**, 127 (1998).
- [Kim04] H. J. Kimble and S. J. van Enk, *Quantum physics: Push-button teleportation*, Nature **429**, 712 (2004).
- [Kim10] K. Kim, M.-S. Chang, S. Korenblit, R. Islam, E. E. Edwards, J. K. Freericks, G.-D. Lin, L.-M. Duan, and C. Monroe, *Quantum simulation of frustrated Ising spins with trapped ions*, Nature **465**, 590 (2010).
- [Kir09] G. Kirchmair, J. Benhelm, F. Zähringer, R. Gerritsma, C. F. Roos, and R. Blatt, *Deterministic entanglement of ions in thermal states of motion*, New J. Phys. **11**, 023002 (2009).

- 
- [Kos72] A. Kossakowski, *On quantum statistical mechanics of non-Hamiltonian systems*, Reports on Mathematical Physics **3**, 247 (1972).
  - [Kre05] A. Kreuter, C. Becher, G. P. T. Lancaster, A. B. Mundt, C. Russo, H. Häffner, C. Roos, W. Hänsel, F. Schmidt-Kaler, R. Blatt, and M. S. Safronova, *Experimental and theoretical study of the  $3d^2D$ -level lifetimes of  $^{40}\text{Ca}^+$* , Phys. Rev. A **71**, 032504 (2005).
  - [Kuh99] A. Kuhn, M. Hennrich, T. Bondo, and G. Rempe, *Controlled generation of single photons from a strongly coupled atom-cavity system*, Appl Phys B **69**, 373 (1999).
  - [Lei97] D. Leibfried, D. M. Meekhof, C. Monroe, B. E. King, W. M. Itano, and D. J. Wineland, *Experimental preparation and measurement of quantum states of motion of a trapped atom*, Journal of Modern Optics **44**, 2485 (1997).
  - [Lei03a] D. Leibfried, R. Blatt, C. Monroe, and D. Wineland, *Quantum dynamics of single trapped ions*, Rev. Mod. Phys. **75**, 281 (2003).
  - [Lei03b] D. Leibfried, B. DeMarco, V. Meyer, D. Lucas, M. Barrett, J. Britton, W. M. Itano, B. Jelenkovic, C. Langer, T. Rosenband, and D. J. Wineland, *Experimental demonstration of a robust, high-fidelity geometric two ion-qubit phase gate*, Nature **422**, 412 (2003).
  - [Lei05] D. Leibfried, E. Knill, S. Seidelin, J. Britton, R. B. Blakestad, J. Chiaverini, D. B. Hume, W. M. Itano, J. D. Jost, C. Langer, and et al., *Creation of a six-atom 'Schrödinger cat' state*, Nature **438**, 639 (2005).
  - [Lia95] S.-S. Liaw, *Ab initio calculation of the lifetimes of  $4p$  and  $3d$  levels of  $\text{Ca}^+$* , Phys. Rev. A **51**, R1723 (1995).
  - [Lin76] G. Lindblad, *On the generators of quantum dynamical semigroups*, Commun.Math. Phys. **48**, 119 (1976).
  - [Lou97] R. Loudon, *The Quantum Theory Of Light*, Oxford Science Publications, 1997.
  - [Lud15] A. D. Ludlow, M. M. Boyd, J. Ye, E. Peik, and P. O. Schmidt, *Optical atomic clocks*, Rev. Mod. Phys. **87**, 637 (2015).
  - [Mac12] T. Macha, *Frequenzstabilisierung eines Titan-Saphir-Lasers und Verbesserung von Qubits mit  $\text{Ca}^+$ -Ionen*, Master's thesis, Universität Mainz (2012).
  - [Man80] Y. Manin, *Vychislimoe i nevychislimoe*, Sov. Radio 13–15 (1980).

- [Mid12] T. Middelmann, S. Falke, C. Lisdat, and U. Sterr, *High Accuracy Correction of Blackbody Radiation Shift in an Optical Lattice Clock*, Phys. Rev. Lett. **109**, 263004 (2012).
- [MK13] T. Mayer-Kuckuk, *Atomphysik: Eine Einführung*, Vieweg+Teubner Verlag, 2013.
- [Mon95] C. Monroe, D. M. Meekhof, B. E. King, S. R. Jefferts, W. M. Itano, D. J. Wineland, and P. Gould, *Resolved-Sideband Raman Cooling of a Bound Atom to the 3D Zero-Point Energy*, Physical Review Letters **75**, 4011 (1995).
- [Mon96] C. Monroe, D. M. Meekhof, B. E. King, and D. J. Wineland, *A “Schrodinger Cat” Superposition State of an Atom*, Science **272**, 1131 (1996).
- [Mon11] T. Monz, P. Schindler, J. T. Barreiro, M. Chwalla, D. Nigg, W. A. Coish, M. Harlander, W. Hänsel, M. Hennrich, and R. Blatt, *14-Qubit Entanglement: Creation and Coherence*, Physical Review Letters **106**, 130506 (2011).
- [Mon16] T. Monz, D. Nigg, E. A. Martinez, M. F. Brandl, P. Schindler, R. Rines, S. X. Wang, I. L. Chuang, and R. Blatt, *Realization of a scalable Shor algorithm*, Science **351**, 1068 (2016).
- [Mun02] A. B. Mundt, A. Kreuter, C. Becher, D. Leibfried, J. Eschner, F. Schmidt-Kaler, and R. Blatt, *Coupling a Single Atomic Quantum Bit to a High Finesse Optical Cavity*, Physical Review Letters **89**, 103001 (2002).
- [Nag86] W. Nagourney, J. Sandberg, and H. Dehmelt, *Shelved optical electron amplifier: Observation of quantum jumps*, Physical Review Letters **56**, 2797 (1986).
- [Nie00] M. A. Nielsen and I. L. Chuang, *Quantum Computation and Quantum Information*, Cambridge University Press, 2000.
- [Niz05] A. P. Nizovtsev, *A Quantum Computer Based on NV Centers in Diamond: Optically Detected Nutations of Single Electron and Nuclear Spins*, Opt. Spectrosc. **99**, 233 (2005).
- [Obe99] H. Oberst, *Resonance fluorescence of single Barium ions*, Master’s thesis, Leopold-Franzens-Universität Innsbruck (1999).
- [Olm09] S. Olmschenk, D. N. Matsukevich, P. Maunz, D. Hayes, L.-M. Duan, and C. Monroe, *Quantum Teleportation Between Distant Matter Qubits*, Science **323**, 486 (2009).



- 
- [Ott16] K. Ott, S. Garcia, R. Kohlhaas, K. Schüppert, P. Rosenbusch, R. Long, and J. Reichel, *Millimeter-long Fiber Fabry-Perot cavities*, arXiv:1603.04791[physics.optics] (2016).
  - [Pau58] W. Paul, O. Osberghaus, and E. Fischer, *Ein Ionenkäfig*, Forschungsberichte des Wirtschafts- und Verkehrsministeriums Nordrhein-Westfalen (1958).
  - [Pau90] W. Paul, *Electromagnetic traps for charged and neutral particles*, Rev. Mod. Phys. **62**, 531 (1990).
  - [Pfi16] A. D. Pfister, M. Salz, M. Hettrich, U. G. Poschinger, and F. Schmidt-Kaler, *A quantum repeater node with trapped ions: a realistic case example*, Appl. Phys. B **122**, 89 (2016).
  - [Pos10a] U. Poschinger, A. Walther, K. Singer, and F. Schmidt-Kaler, *Observing the Phase Space Trajectory of an Entangled Matter Wave Packet*, Physical Review Letters **105**, 263602 (2010).
  - [Pos10b] U. G. Poschinger, *Quantum Optics Experiments in a Microchip Ion Trap*, Ph.D. thesis, Universität Ulm (2010).
  - [Poz02] C. Pozrikidis, *A Practical Guide to Boundary Element Methods with the Software Library BEMLIB*, CRC Press, 2002.
  - [Pru14] T. Pruttivarasin, M. Ramm, and H. Häffner, *Direct spectroscopy of the  $2\,S\,1/2 - 2\,P\,1/2$  and  $2\,D\,3/2 - 2\,P\,1/2$  transitions and observation of micro-motion modulated spectra in trapped  $40\,\text{Ca}^+$* , Journal of Physics B: Atomic, Molecular and Optical Physics **47**, 135002 (2014).
  - [Ram13] M. Ramm, T. Pruttivarasin, M. Kokish, I. Talukdar, and H. Häffner, *Precision Measurement Method for Branching Fractions of Excited  $P_{1/2}$  States Applied to  $^{40}\text{Ca}^+$* , Phys. Rev. Lett. **111**, 023004 (2013).
  - [Rau06] E. Rauscher and G. W. Marcy, *Ca II H and K Chromospheric Emission Lines in Late-K and M Dwarfs*, PASP **118**, 617 (2006).
  - [Rei13] A. Reiserer, C. Nölleke, S. Ritter, and G. Rempe, *Ground-State Cooling of a Single Atom at the Center of an Optical Cavity*, Physical Review Letters **110**, 223003 (2013).
  - [Rei15] A. Reiserer and G. Rempe, *Cavity-based quantum networks with single atoms and optical photons*, Rev. Mod. Phys. **87**, 1379 (2015).

- [Rie04] M. Riebe, H. Häffner, C. F. Roos, W. Hänsel, J. Benhelm, G. P. T. Lancaster, T. W. Körber, C. Becher, F. Schmidt-Kaler, D. F. V. James, and R. Blatt, *Deterministic quantum teleportation with atoms*, Nature **429**, 734 (2004).
- [Rie05] M. Riebe, *Preparation of Entangled States and Quantum Teleportation with Atomic Qubits*, Ph.D. thesis, Leopold-Franzens-Universität Innsbruck (2005).
- [Roh01] H. Rohde, *Experimente zur Quanteninformation in einer lineare Ionenfalle*, Ph.D. thesis, Leopold-Franzens-Universität Innsbruck (2001).
- [Roo99] C. Roos, T. Zeiger, H. Rohde, H. C. Nägerl, J. Eschner, D. Leibfried, F. Schmidt-Kaler, and R. Blatt, *Quantum State Engineering on an Optical Transition and Decoherence in a Paul Trap*, Physical Review Letters **83**, 4713 (1999).
- [Roo00] C. F. Roos, *Controlling the quantum state of trapped ions*, Ph.D. thesis, Leopold-Franzens-Universität Innsbruck (2000).
- [Roo06] C. Roos, M. Chwalla, K. Kim, M. Riebe, and R. Blatt, 'Designer atoms' for quantum metrology, Nature **443**, 316 (2006).
- [Rot03] D. Rotter, *Photoionisation von Kalzium*, Master's thesis, Leopold-Franzens-Universität Innsbruck (2003).
- [Rus14] T. Ruster, C. Warschburger, H. Kaufmann, C. T. Schmiegelow, A. Walther, M. Hettrich, A. Pfister, V. Kaushal, F. Schmidt-Kaler, and U. G. Poschinger, *Experimental realization of fast ion separation in segmented Paul traps*, Physical Review A **90**, 033410 (2014).
- [Saf11] M. S. Safronova and U. I. Safronova, *Blackbody radiation shift, multipole polarizabilities, oscillator strengths, lifetimes, hyperfine constants, and excitation energies in  $\text{Ca}^+$* , Phys. Rev. A **83**, 012503 (2011).
- [Saf13] M. S. Safronova, S. G. Porsev, U. I. Safronova, M. G. Kozlov, and C. W. Clark, *Blackbody-radiation shift in the Sr optical atomic clock*, Phys. Rev. A **87**, 012509 (2013).
- [Sah09] B. K. Sahoo, B. P. Das, and D. Mukherjee, *Relativistic coupled-cluster studies of ionization potentials, lifetimes, and polarizabilities in singly ionized calcium*, Phys. Rev. A **79**, 052511 (2009).
- [Sak13] J. Sakurai and J. Napolitano, *Modern Quantum Mechanics*, Pearson custom library, Pearson, 2013.

- 
- [Sal13] M. Salz, *Optimierung einer segmentierten Paulfalle mit optischer Schnittstelle*, Master's thesis, Johannes Gutenberg - Universität Mainz (2013).
  - [Sal15] A. B. Salvador, *Integrated Electromagnets and Radiofrequency Spectroscopy in a Planar Paul Trap*, Ph.D. thesis, Universität Ulm (2015).
  - [Sch35] E. Schrödinger, *Die gegenwärtige Situation in der Quantenmechanik*, Naturwissenschaften **23**, 807 (1935).
  - [Sch08] S. Schulz, U. Poschinger, F. Ziesel, and F. Schmidt-Kaler, *Sideband cooling and coherent dynamics in a microchip multi-segmented ion trap*, New J. Phys. **10**, 045007 (2008).
  - [Sch09] S. Schulz, *Scalable Microchip Ion Traps for Quantum Computation*, Ph.D. thesis, Universität Ulm (2009).
  - [Sch13] P. Schindler, D. Nigg, T. Monz, J. T. Barreiro, E. Martinez, S. X. Wang, S. Quint, M. F. Brandl, V. Nebendahl, C. F. Roos, and et al., *A quantum information processor with trapped ions*, New J. Phys. **15**, 123012 (2013).
  - [Scu01] M. O. Scully and M. S. Zubairy, *Quantum Optics*, Cambridge University Press, 2001.
  - [Sin02] K. Singer, S. Jochim, M. Mudrich, A. Mosk, and M. Weidemüller, *Low-cost mechanical shutter for light beams*, Review of Scientific Instruments **73**, 4402 (2002).
  - [Sin10] K. Singer, U. Poschinger, M. Murphy, P. Ivanov, F. Ziesel, T. Calarco, and F. Schmidt-Kaler, *Colloquium: Trapped ions as quantum bits: Essential numerical tools*, Rev. Mod. Phys. **82**, 2609 (2010).
  - [SK03] F. Schmidt-Kaler, H. Häffner, M. Riebe, S. Gulde, G. P. T. Lancaster, T. Deuschle, C. Becher, C. F. Roos, J. Eschner, and R. Blatt, *Realization of the Cirac-Zoller controlled-NOT quantum gate*, Nature **422**, 408 (2003).
  - [Ste86] S. Stenholm, *The semiclassical theory of laser cooling*, Rev. Mod. Phys. **58**, 699 (1986).
  - [Ste06] T. Steinmetz, Y. Colombe, D. Hunger, T. W. Hänsch, A. Balocchi, R. J. Warburton, and J. Reichel, *Stable fiber-based Fabry-Perot cavity*, Applied Physics Letters **89**, 111110 (2006).
  - [Ste13] M. Steiner, H. M. Meyer, C. Deutsch, J. Reichel, and M. Köhl, *Single Ion Coupled to an Optical Fiber Cavity*, Physical Review Letters **110**, 043003 (2013).

- [Stu12] A. Stute, B. Casabone, P. Schindler, T. Monz, P. O. Schmidt, B. Brandstätter, T. E. Northup, and R. Blatt, *Tunable ion - photon entanglement in an optical cavity*, Nature **485**, 482 (2012).
- [Tak14] H. Takahashi, J. Morphew, F. Orucevic, A. Noguchi, E. Kassa, and M. Keller, *Novel laser machining of optical fibers for long cavities with low birefringence*, Optics Express **22**, 31317 (2014).
- [Tha99] G. Thalhammer, *Frequenzstabilisierung von Diodenlasern bei 850, 854 und 866 nm mit Linienbreiten in Kilohertz-Bereich*, Master's thesis, Universität Innsbruck (1999).
- [The89] C. E. Theodosiou, *Accurate calculation of the  $4p$  lifetimes of  $\text{Ca}^+$* , Phys. Rev. A **39**, 4880 (1989).
- [Uph16] M. Uphoff, M. Brekenfeld, G. Rempe, and S. Ritter, *An integrated quantum repeater at telecom wavelength with single atoms in optical fiber cavities*, Appl. Phys. B **122**, 46 (2016).
- [Vae92] N. Vaeck, M. Godefroid, and C. Froese Fischer, *Core-valence correlation effects on  $E\ 1$  and  $E\ 2$  decay rates in  $\text{Ca}^+$* , Phys. Rev. A **46**, 3704 (1992).
- [Vis09] T. D. Visser, *Whose Golden Rule is it anyway?*, American Journal of Physics **77**, 487 (2009).
- [Vit01] N. V. Vitanov, T. Halfmann, B. W. Shore, and K. Bergmann, *Laser-Induced Population Transfer By Adiabatic Passage Techniques*, Annu. Rev. Phys. Chem. **52**, 763 (2001).
- [Wal12] A. Walther, F. Ziesel, T. Ruster, S. T. Dawkins, K. Ott, M. Hettrich, K. Singer, F. Schmidt-Kaler, and U. Poschinger, *Controlling Fast Transport of Cold Trapped Ions*, Physical Review Letters **109** (2012).
- [Win75] D. J. Wineland and H. Dehmelt, *Proposed  $10^{14} \Delta\nu < \nu$  Laser Fluorescence Spectroscopy on  $\text{Tl}^+$  Mono-Ion Oscillator III*, Bulletin of the American Physical Society **20**, 637 (1975).
- [Win78] D. J. Wineland, R. E. Drullinger, and F. L. Walls, *Radiation-Pressure Cooling of Bound Resonant Absorbers*, Physical Review Letters **40**, 1639 (1978).
- [Win79] D. J. Wineland and W. M. Itano, *Laser cooling of atoms*, Physical Review A **20**, 1521 (1979).

- [Win03] D. J. Wineland, M. Barret, J. Britton, J. Chiaverini, B. DeMarco, W. M. Itano, B. Jelenkovic, C. Langer, D. Leibfried, V. Meyer, T. Rosenband, and T. Schätz, *Quantum information processing with trapped ions*, Phil. Trans. R. Soc. Lond. A. **361**, 1349 (2003).
- [Woo82] W. K. Wootters and W. H. Zurek, *A single quantum cannot be cloned*, Nature **299**, 802 (1982).
- [Zie12] F. Ziesel, *Quantum State Manipulation and Dynamics in Micro Ion Traps*, Ph.D. thesis, Universität Ulm (2012).



# Curriculum Vitae

**Max Hettrich**

## AUSBILDUNG

### Promotion in Physik

seit 10.2009                      Universität Ulm

### Studium der Physik

03.2008 - 04.2009              Diplomarbeit am Institut für  
Quanteninformationsverarbeitung, Universität Ulm,  
Titel: „Präparation eines  $^{40}\text{Ca}^+$  - Quantenbits und  
Entwicklung eines faseroptischen Resonators für seine  
Detektion”

09.2006 - 01.2007              Studium der Physik, Universität Leeds

10.2003 - 04.2009              Studium der Physik, Universität Ulm

## PRAKTISCHE ERFAHRUNG

seit 04.2011                      wissenschaftlicher Mitarbeiter, WA Quantum,  
Johannes Gutenberg - Universität Mainz

04.2009 - 03.2011              wissenschaftlicher Mitarbeiter, Institut für  
Quanteninformationsverarbeitung, Universität Ulm

02.2007 - 04.2007              Industriepraktikum, Carl Zeiss AG, Oberkochen,  
Unternehmensbereich Forschung und Technologie





# Danksagung

Die erfolgreiche Durchführung der in dieser Arbeit beschriebenen Experimente war nur durch die Unterstützung Vieler möglich, deshalb möchte ich diese abschließenden Worte hier dafür verwenden, denjenigen herzlich zu danken, welche, direkt oder indirekt, zum Gelingen dieser Dissertation beigetragen haben.

An erster Stelle steht selbstverständlich Ferdinand Schmidt-Kaler, der es mir ermöglicht hat, in seiner Arbeitsgruppe die beschriebenen Experimente durchzuführen. Sein physikalisches Gespür und seine Erfahrung waren für die Überwindung der schwierigeren Phasen dieser Arbeit von unschätzbarem Wert, und seine Begeisterungsfähigkeit sowie sein außergewöhnlicher persönlicher Einsatz haben mich immer motiviert, mit vollem Einsatz auf meine Ziele hinzuarbeiten, und dabei nie die Freude an der Sache zu verlieren.

Uli Poschinger konnte mich überzeugen, mich auf eine atomphysikalische Präzisionsmessung einzulassen, was sich zu einem äußerst spannenden und aufregenden Unterfangen entwickelte. Seine betreuende Begleitung war immer extrem konstruktiv und hat zum Erfolg dieses Projekts entscheidend beigetragen, und von seiner Fähigkeit, die Ursachen von experimentellen Problemen zu erkennen, und seiner kritischen Perspektive, gerade was die Quantifizierung von Messunsicherheiten betrifft habe ich eine Menge lernen können. Ein dickes Dankeschön geht auch an Henning Kaufmann, Thomas Ruster und Christian Schmiegelow, die mir bei den berüchtigten Streuratenmessungen immer mit Rat und Tat zur Seite standen. Auch Christian Roos aus Innsbruck konnte durch seine Sicht auf die Dinge von außen wertvolle Beiträge liefern.

Beim Aufbau der Falle für das CQED-Experiment konnte ich immer auf die engagierte Mithilfe von Andy Pfister und Marcel Salz zählen, auch Frank Ziesel hat wichtige Beiträge in der Frühphase dieses Experiments geleistet. Georg Jacob und Thomas Feldker waren immer kluge Ideengeber und Gesprächspartner bei zahlreichen physikalischen Diskussionen. Ein gewisses gemeinsames Interesse für guten Kaffee und gutes Bier war dabei sicher nicht hinderlich. Auch Kilian Singer gebührt Dank. Seine blitzschnelle Auffassungsgabe zusammen mit seinem breiten physikalischen und technischen Verständnis haben mir sehr oft weitergeholfen.

Siegbert Felzer sei hier stellvertretend für alle Mitarbeiter der mechanischen Werkstatt genannt, die immer ausgezeichnet gearbeitet haben. Von Heinz Lenk und Michael Boßenecker hatte ich immer hervorragende Unterstützung, wenn es um Elektronik ging.

Jenseits des Labors haben mich einige Personen aus meinem Alltag vor dem sicheren Wahnsinn bewahrt: Jasmin Düring danke ich für die vielen wunderbaren Gespräche, Diskussionen und Streitereien über Literatur, Politik, Musik und die Zubereitung klassischer Cocktails. Ein wichtiger sportlicher Ausgleich zur Arbeit in fensterlosen Laboren waren die regelmäßigen Joggingrunden mit Dominik Haderer und Johannes Eichner, außerdem bekam ich durch sie immer wieder hochinteressante Blicke hinter die Kulissen der Spieleentwicklung. Nicht zuletzt danke ich an dieser Stelle auch meinen Eltern, die von früher Kindheit an immer meine Neugier förderten und mir die Freude am kritischen Denken vermittelten.